PROCESSING AND GAS BARRIER BEHAVIOR OF MULTILAYER THIN NANOCOMPOSITE FILMS

A Dissertation

by

YOU-HAO YANG

Submitted to the Office of Graduate Studies of
Texas A&M University
in partial fulfillment of the requirements for the degree of

DOCTOR OF PHILOSOPHY

August 2012

Major Subject: Chemical Engineering

Processing and Gas Barrier Behavior of Multilayer Thin Nanocomposite Films

PROCESSING AND GAS BARRIER BEHAVIOR OF MULTILAYER THIN NANOCOMPOSITE FILMS

A Dissertation

by

YOU-HAO YANG

Submitted to the Office of Graduate Studies of
Texas A&M University
in partial fulfillment of the requirements for the degree of

DOCTOR OF PHILOSOPHY

Approved by:

Chair of Committee,	Jaime C. Grunlan
Committee Members,	Hae-Kwon Jeong
	Victor M. Ugaz
	James D. Batteas
Head of Department,	Charles Glover

August 2012

Major Subject: Chemical Engineering

ABSTRACT

Processing and Gas Barrier Behavior of Multilayer Thin Nanocomposite Films.

(August 2012)

You-Hao Yang, B.S., National Taiwan University

Chair of Advisory Committee: Dr. Jaime C. Grunlan

Thin films with the ability to impart oxygen and other types of gas barrier are crucial to commercial packaging applications. Commodity polymers, such as polyethylene (PE), polycarbonate (PC) and polyethylene terephthalate (PET), have insufficient barrier for goods requiring long shelf life. Current gas barrier technologies like plasma-enhanced vapor deposition (PECVD) often create high barrier metal oxide films, which are prone to cracking when flexed. Bulk composites composed of polymer and impermeable nanoparticles show improved barrier, but particle aggregation limits their practical utility for applications requiring high barrier and transparency. Layer-by-layer (LbL) assemblies allow polymers and nanoparticles to be mixed with high particle loadings, creating super gas barrier thin films on substrates normally exhibiting high gas permeability.

Branched polyethylenimine (PEI) and poly (acrylic acid) (PAA) were deposited using LbL to create gas barrier films with varying pH combinations. Film thickness and mass fraction of each component was controlled by their combined charge. With lower charge density (PEI at pH 10 and PAA at pH 4), PEI/PAA assemblies exhibit the best oxygen barrier relative to other pH combinations. An 8 BL PEI/PAA film, with a thickness of 451 nm, has an oxygen permeability lower than 4.8×10^{-21} $cm^3 \cdot cm/cm^2 \cdot s \cdot Pa$, which is comparable to a 100 nm SiO_x nanocoating. Crosslinking these films with glutaraldehyde (GA), 1-[3-(dimethylamino)propyl]-3-ethylcarbodiimide methiodide (EDC) or heating forms covalent bonds between PEI and/or PAA. Oxygen transmission rates (OTR) of 8 BL films crosslinked with 0.1M GA or 0.01M EDC show the best oxygen barrier at 100% RH.

Graphene oxide (GO) sheets and PEI were deposited via LbL with varying GO concentration. The resulting thin films have an average bilayer thickness from 4.3 to 5.0 nm and a GO mass fraction from 88 to 91wt%. Transmission electron microscopy and atomic force microscopy images reveal a highly-oriented nanobrick wall structure. A 10 BL PEI/GO film that is 91 nm thick, made with a 0.2 wt% GO suspension, exhibits an oxygen permeability of 2.5×10^{-20} $cm^3 \cdot cm/cm^2 \cdot s \cdot Pa$.

Finally, the influence of deposition time on thin film assembly was examined by depositing montmorillonite (MMT) or laponite (LAP) clays paired with PEI. Film growth and microstructure suggests that smaller aspect ratio LAP clay is more dip-time dependent than MMT and larger aspect ratio MMT has better oxygen barrier. A 30 BL PEI/MMT film made with 10 second dips in PEI has the same undetectable OTR as a film with 5 minute dips (with dips in MMT held at 5 minutes in both cases), indicating LbL gas barrier can be made more quickly than initially thought. These high barrier recipes, with simple and efficient processing conditions, are good candidates for a variety of packaging applications.

DEDICATION

To

My dearest parents

ACKNOWLEDGEMENTS

I would like to thank my committee chair, Dr. Jaime Grunlan, who gives me such a great opportunity to work on gas barrier projects, which furnished my research life with continuous excitement and challenges these past few years. Thanks also go to my committee members, Dr. Hae-Kwon Jeong, Dr. Victor Ugaz, and Dr. James Batteas, for their guidance throughout the course of this research. I would also like to thank Dr. Nicole Zacharia and Dr. Jodie Lutkenhaus for their valuable suggestions.

Thanks also go to my colleagues in the Polymer Nanocomposite laboratory. Former graduate students Yu-Chin Li, Yong Tae Park, Morgan Priolo and the rest of the current PNC group members (Galina, Greg, Amanda and Bart), gave me great help and support in both work and life. Most importantly, I would like to acknowledge my three talented undergraduate students (Frank Malek, Merid Haile and Laura Bolling). Without their contributions I could not finish my degree in such an efficient and successful manner.

Finally, I want to give my greatest appreciation to my family and friends who support me with endless love and encouragement. Without you, I would not be able to finish this journey in pursuit of the Ph.D. degree.

NOMENCLATURE

AFM	Atomic force microscopy
ASTM	American society for testing and materials
BL	Bilayer
DSC	Differential scanning calorimeter
EDC	1-[3-(dimethylamino)propyl]-3-ethylcarbodiimide methiodide
EVOH	Ethylene vinyl alcohol
FTIR	Fourier transform infrared spectroscopy
GA	Glutaraldehyde
GO	Graphene oxide
HA	Hyaluronan
LAP	Laponite
LbL	Layer-by-layer
LCP	Liquid crystal polymer
MMT	Montmorillonite
OLED	Organic light-emitting device
OTR	Oxygen transmission rate
PA	Polyamide
PAA	Poly(acrylic acid)
PAAm	Poly(allylamine)
PAH	Poly(allylamine hydrochloride)

PAm	Polyacrylamide
PDDA	Poly(dimethyldiallylammonium chloride)
PE	Polyethylene
PECVD	Plasma-enhanced chemical vapor deposition
PEI	Branched polyethylenimine
PEN	Polyethylene naphthenate
PET	Polyethylene terephthalate
PLL	Poly(L-lysine)
PP	Polypropylene
PS	Polystyrene
PSS	Poly(styrene sulfate)
PVA	Poly(vinyl alcohol)
PVC	Polyvinylchloride
PVD	Physical vapor deposition
PVDC	Polyvinylidene chloride
QCM	Quartz crystal microbalance
QL	Quadlayer
RMS	Root-mean-square
SEM	Scanning electron microscopy
SPM	Scanning probe microscopy
TEM	Transmission electron microscopy
T_g	Glass transition temperature

WPO	World packaging organization
WVTR	Water vapor transmission rate
XRD	X-ray diffraction

TABLE OF CONTENTS

Page

CHAPTER

LIST OF FIGURES

FIGURE Page

FIGURE Page

LIST OF TABLES

CHAPTER I

INTRODUCTION

1.1 Background

Packaging materials play a significant role in modern society. Food, beverages, cosmetics, pharmaceuticals and electronics all require good gas and moisture protection. According to a report from the World Packaging Organization (WPO), from 1999 to 2009, global packaging sales increased from 372.4 to 563.9 billion dollars.[1] Plastic packaging materials such as polyethylene (PE), polypropylene (PP), polyvinylchloride (PVC) and polyethylene terephthalate (PET) are extensively used for making containers, lids, pouches, and films due to their barrier properties, mechanical flexibility and price.[2, 3] The global capacity of PET grew from 0.5 M tons in 1985 to 7.0 M tons in 2000.[4] Although it has already been a major material for food and soft drinks, which competes successfully with traditional glass and metal for containers and bottles, the insufficient barrier properties for oxygen, carbon dioxide and moisture disqualifies PET for goods requiring long-shelf life needed.[4]

Various coating technologies have been evaluated to improve the gas barrier of commodity polymers like PET. Laminating high-barrier polymers (e.g., ethylene vinyl alcohol (EVOH) or polyvinylidene chloride (PVDC)),[4] depositing inorganic layers (e.g., SiO_x or alumina) by plasma enhanced chemical vapor deposition (PECVD),[5] and

---

This dissertation follows the style of *Macromolecules.*

incorporating nanoparticles, in the form of solvent casting[6, 7] or layer-by-layer nanocoatings,[8] have been used to improve polymer film barrier.

As a thin film fabrication technique, layer-by-layer assembly (LbL) is one of the most versatile, efficient and robust technologies studied over the past two decades.[9-11] By alternately exposing the substrate to oppositely-charged polyelectrolyte solutions, electrostatic attractions between the positively and negatively charged ingredients result in the buildup of a multilayer structure, as shown in Figure 1.1. In addition to electrostatic attraction,[12] hydrogen bonding[13] and covalent bonding[14] can also be used in a layer-by-layer fashion.

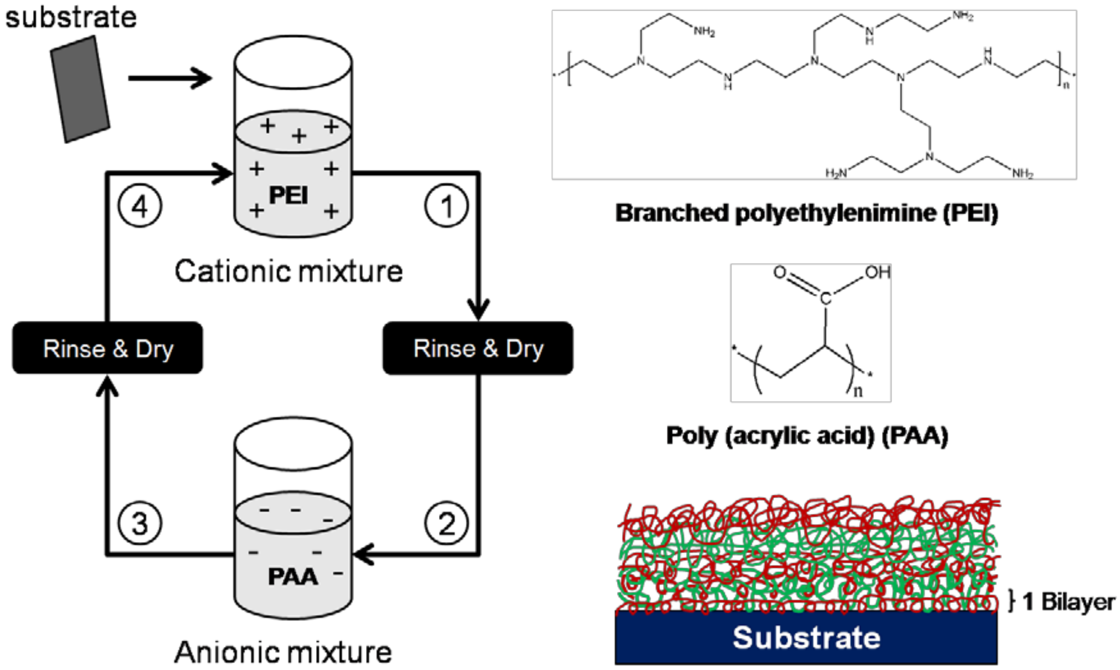

Figure 1.1. Schematic of the layer-by-layer deposition process. Steps 1-4 are repeated until the desired number of PEI/PAA bilayers are deposited.[15]

A variety of ingredients can be incorporated into LbL coatings such as polymers,[16-18] quantum dots,[19-21] nanoparticles (including spheres, rods, tubes and plates),[22-32] organic dyes,[33-35] dendrimers,[36-38] and biological molecules (including peptides, DNA, proteins and viruses).[12, 39-46] Properties of LbL films can be easily tailored by changing molecular weight,[47, 48] concentration,[49, 50] chemistry,[51] pH,[49, 52] ionic strength,[49, 53] temperature[54, 55] and deposition time[49, 56] of the deposited species and the aqueous solutions or mixtures. Moreover, nearly any substrate can be coated by LbL assembly, regardless of shape, size and surface complexity. These advantages make LbL assembly a good candidate for applications that include gas barrier coatings,[8] superhydrophobicity,[57-59] antimicrobials,[60-62] drug delivery,[63-65] electrical conductivity,[23, 66, 67] selective area patterning,[22, 68, 69] and battery electrolytes.[70, 71]

1.2 Objectives and Dissertation Outline

In the present work, two LbL systems (i.e., polymer-polymer and polymer-nanoplatelet) are studied with a focus on reducing the oxygen permeability. By increasing the distance of the diffusion path and creating more interactions throughout the thin film structure, fewer oxygen molecules are able to transmit through the coated film in a given time. The goal of this dissertation is to demonstrate the capability of improving gas barrier via LbL coatings with varying recipes and processing parameters. Crosslinking is an important parameter that influences oxygen and moisture barrier of non-linear growing assemblies. Deposition time, an important processing parameter in terms of commercial applications, is also discussed in conjunction with a polymer-nanoplatelet system.

Chapter II is a literature review of gas transport mechanisms and barrier coating technologies that includes polymer blends, metalized plastics, metal oxides, and nanocomposites. A detailed introduction of linear and non-linear growth in LbL systems is also provided to highlight the versatility of this technique.

Chapter III describes an all-polymer LbL assembly that achieves the lowest oxygen permeability ever reported. Films assembled with different pH combinations of polyethylenimine (PEI) and poly(acrylic acid) (PAA) exhibited different rates of growth, microstructure and oxygen barrier performance. The unprecedented barrier behavior comes from the unique interactions between PEI and PAA polymer chains created by LbL deposition, which is explained by a "scrambled-egg" structure and verified by differential scanning calorimetry.

Chapter IV is an extension of Chapter III in which crosslinking is used to improve the barrier of PEI/PAA assemblies. This covalent bonding improves the humid oxygen barrier and moisture barrier of PEI/PAA thin films. Glutaraldehyde (GA), 1-[3-(dimethylamino)propyl]-3-ethylcarbodiimide methiodide (EDC) and thermal crosslinking were used at different concentrations, temperatures and times. The resulting thickness and topography variation were evaluated by ellipsometry and atomic force microscopy (AFM). Fourier transform infrared spectra (FTIR) confirmed the bonding after exposure to a given crosslinking treatment.

Chapter V is a polymer-nanoplatelet gas barrier study with PEI and graphene oxide (GO). Nanobrick walls deposited via LbL resulted in linear film growth, measured by ellipsometry and quartz crystal microbalance (QCM). Oxygen barrier of PEI/GO assemblies was evaluated as a function of GO suspension concentrations. Hydrogen, carbon dioxide and moisture transmission rates were also tested to confirm the universality of this behavior.

Chapter VI compares PEI with montmorillonite (MMT) or laponite (LAP) clay by varying exposure times in the LbL dipping process. The aspect ratio difference between MMT and LAP platelets makes the assembled films grow differently in terms of short and long deposition times. X-ray diffraction (XRD) confirms that MMT platelets have similar gallery spacing independent of dip time, suggesting that LbL can be executed in a fast manner. This study indicates that LbL assemblies could be produced more quickly, which is a key challenge for their commercial use.

Chapter VII describes the conclusions and future directions of this work. Oxygen transmission rates of PET were successfully decreased by coating polymer-polymer or polymer-nanoplatelet LbL assemblies. To further improve the performance of gas or moisture barrier, different solvent can be used to replace water. Moreover, the surface of graphene oxide platelets can be modified to be positively charged, which can be used to create an all-GO based gas or moisture barrier.

CHAPTER II

LITERATURE REVIEW

2.1 Gas Diffusion Theory

Barrier coatings are vital for food, pharmaceuticals and electronics packaging because of their ability to slow down or prevent gas diffusion. In order to design a coating for low gas permeability, one needs to understand the transport phenomena behind it. Gas diffusion is a type of mass transfer that can be characterized by four steps: adsorption of gas molecules onto the film surface, dissolution from the surface into the inner structure, migration through the film thickness and finally desorption from the other side of the film.[72] In most cases, the second and third steps are determined by the permeation properties of the materials, which can be classified by their pore sizes. Porous packaging refers to materials with an average pore size larger than 2 nm, whereas dense packaging suggests a pore size smaller than 2 nm.[73] A comparison among different packaging types and their corresponding diffusion mechanisms are listed in Table 2.1. Layer-by-layer coating belongs to the category of dense packaging, and is the focus of this dissertation, so the porous materials will not be further reviewed here.

Table 2.1. Packaging types and their corresponding diffusion mechanisms.

Packaging Types	Diffusion Mechanisms
Porous material	Knudsen flow[74] Surface diffusion[75] Activated diffusion[76] Capillary condensation[77]
Dense material	Molecular model[78-81] Free volume theory[82] Dual-mode sorption[83, 84]
Nanocomposite	Tortuous path[85, 86]

2.1.1 Molecular Transport in a Polymer

Polymers are a dense packaging material due to their packed polymer chains that allow very few permeable pathways for molecules.[87] Molecular penetrants need to be dissolved into the polymer matrix and diffuse through it. This solution-diffusion process is defined by:

$$P = D \times S \tag{2.1}$$

where P is the permeability ($\mathrm{cm^3 \cdot cm/(cm^2 \cdot s \cdot Pa)}$), D is diffusivity ($\mathrm{cm^2/s}$) and S is the solubility ($\mathrm{cm^3(273.15K;\ 1.013 \times 10^5\ Pa)/cm^3 \cdot\ Pa}$) of the polymer. Diffusivity is a kinetic factor that characterizes the ability of molecules to move through the polymer phase, whereas solubility is a thermodynamic factor related to the penetrant-polymer interactions as well as the gas condensability. Gas transport is influenced by the polymer morphology. When the transport happens above the polymer’s glass transition temperature (T_g), it is in a rubbery state. When the transport happens below the T_g, it is in a glassy state. The difference between rubbery and glassy state is the former one is in thermodynamic equilibrium, whereas the latter one is not.[87]

2.1.1.1 Transport in a Rubbery Polymer

When gas molecules dissolve into a polymer, the interactions between the penetrants and the polymers will cause a change of physical state in the polymer. In the case of a rubbery polymer, the adjusting time for the influenced polymer chains is much shorter than the total diffusion time, so the overall transport phenomena can be considered Fickian flow.[2] Molecular models and free volume theory are the two methods for describing gas diffusion in rubbery polymer. In molecular models, gas diffusion can only start with activation energy higher than the energy gap between the gas molecule in its normal state activated states. Without sufficient activation energy, gas molecules cannot jump from one location to another in a rubbery polymer matrix.[88] This energy-based argument, was first proposed by Barrer, suggests that gas diffusion in rubber is a thermally activated process.[89] Activated zone theory defined the activated energy which represents the energy needed for penetrants to jump from a normal to activated state.[78] Brandt further considered the molecular structure of polymer and proposed that another activated energy term represents the intramolecular energy needed for bending the polymer chains apart for the penetrant (Fig. 2.1(a)).[79] DiBenedetto and Paul described the activated state as a penetrant molecule covered in four corners of a unit cell by four cylindrical polymers (Fig. 2.1(b)). The activation energy is equal to the energy for creating a cylindrical void into which a gas penetrant can move into.[81] Pace and Datyner combined Brandt, DiBenedetto and Paul's models and proposed that the gas diffusion in rubbery polymer has two separate mechanisms: transport longitudinally through the void among polymer chains and perpendicular jumping from one cylindrical void to another (Fig. 2.1(c)).[80]

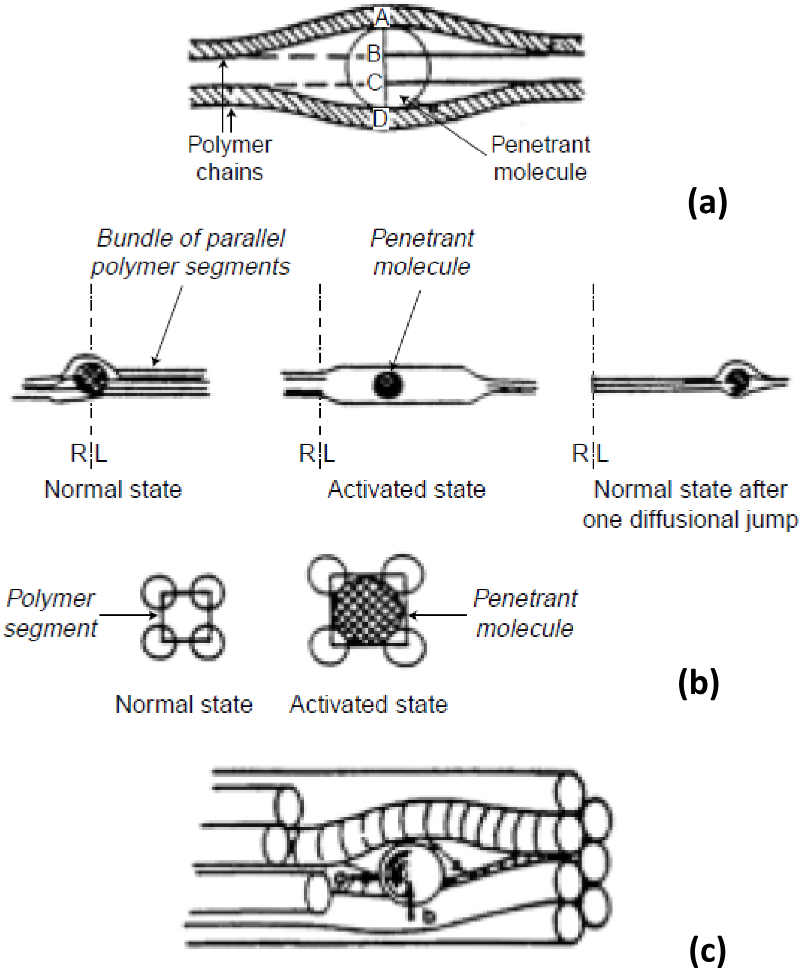

Figure 2.1. Molecular models of diffusion in rubbery polymers proposed by Brandt (a)[79] DiBenedetto and Paul (b)[81] and Pace and Datyner (c).[80]

Free volume theory, in the contrast to the molecular model, defines gas diffusion in polymer as a redistribution of free volumes by fluctuation. The definition of free volume is the actual occupied polymer volume minus the theoretical polymer volume.

One of the earliest free volume theories,[82] proposed by Fujita, suggested that gas transport in polymer has nothing to do with thermal activation, but related to free volume redistribution. Gas molecules can only move from one position to another when their local free volume exceeds a critical value in its vicinity.[88] Diffusivity can be defined by free volume theory:

$$D = A\exp\left(\frac{-B}{f}\right) \tag{2.2}$$

where *A* and *B* are constants of the considered system and *f* represents the fractional free volume:

$$f = \frac{V_{Total} - V_{Occupied}}{V_{Total}} \tag{2.3}$$

where V_{Total} is the sum of the theoretical volume of polymer, $V_{occupied}$, and the free volume in the system.

2.1.1.2 Transport in a Glassy Polymer

Gas diffusion in glassy polymer is more complicated than in the rubbery state because thermodynamic equilibrium is never reached. Since the polymer chains are less mobile when the temperature is below the T_g, it takes more relaxation time for the polymer to respond to gas molecules diffusing through. The diffusion time is often shorter than the structure-rearranging time of the polymer matrix, which causes the penetrant to sit in irregular cavities with different intrinsic diffusional mobilities.[90] As a result of these complexities, most of the existing models for diffusion in glassy polymer are phenomenological, which can only be applied to very specific polymer-penetrant systems.[91]

The most accepted model for gas diffusion in glassy polymer is dual mode sorption, which was first proposed by Barrer[83] and later extended by Koros and Paul.[84] According to the dual mode sorption model, there are two concurrent mechanisms: dissolution of gas in the polymer matrix by Henry's law and adsorption of gas molecules in holes or cavities on the surface or inside the polymer matrix by Langmuir's law. The total concentration of diffusing molecules in a glassy polymer can be described as:

$$C = C_D + C_H = k_D p + \frac{ap}{1+bp} \tag{2.4}$$

where C_D and C_H represent the concentration of normal dissolution and the concentration of trapped molecules by adsorption, respectively. k_D is a proportionality constant of Henry's law. p is pressure and a and b are constants related to the hole affinity of the penetrants. Solubility, on the other hand, can be written as:

$$S = \frac{C}{p} = k_D + \frac{a}{1+bp} \tag{2.5}$$

From Equation 2.5, higher gaseous pressure in the polymer matrix can lead to lower solubility, which in turn can influence the solubility and permeability.

2.1.2 Transport in Nanocomposites

Polymer nanocomposites contain two distinct phases: a nanofiller phase and a polymer phase. The nanofiller is a discontinuous phase, while the polymer matrix is continuous.[92] Adding inorganic nanofillers into a polymer matrix has been shown to successfully enhance mechanical,[93-95] thermal,[96-98] anti-flammable[99-101] and barrier properties[102-104] relative to polymer-only materials because dispersed nanoobjects inside of a polymer matrix can reinforce the structure and create diffusion obstacles for gas molecules. Platelet-like materials, with nanoscale dimensions (1 – 100 nm) and large aspect ratio ($\alpha > 100$), such as graphene,[105] zirconium phosphate,[106] layered double hydroxide[99] and clay[104, 107] contribute to improved gas barrier when they are fully-exfoliated in a polymer matrix. Sodium montmorillonite (MMT) is one of the most studied clays.[103, 108-110] MMT is an inorganic phyllosilicate composed of one inner alumina or magnesia octahedral layer sandwiched by two silica tetrahedral layers, as shown in Figure 2.2.[111] Exchangeable sodium, lithium or other metal ions are intercalated between these silicate sheets, allowing MMT to be dispersed in solvent by a cation exchange process.[108] After superior mechanical properties from a fully exfoliated nylon-clay composite were observed by Toyota,[112] MMT has become one of the most investigated platelets in polymer nanocomposites.[113-115]

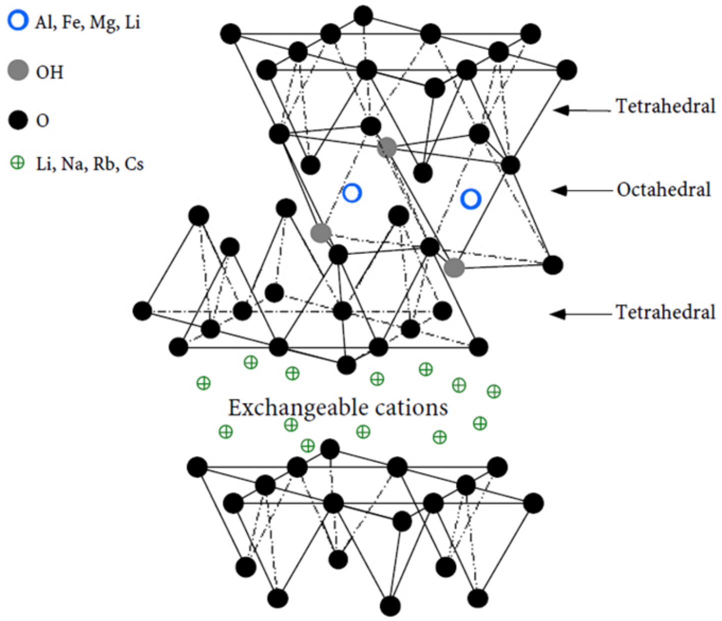

Figure 2.2. Montmorillonite clay chemistry and structure.[111]

Simple physical mixing of polymer and particles will not result in a polymer nanocomposite because the fillers in a polymer matrix often remain agglomerated and none of the dimensions is in nanometer range. Aggregation typically results in poor properties relative to a fully exfoliated nanocomposite.[114] Figure 2.3 illustrates the different morphological states of clay-polymer nanocomposites.[92] The extent of clay separation can be one of three types: (1) conventional composite - clay platelets have the same basal plane spacing d_{001} as the theoretical value, suggested the polymer did not enter the gallery of the platelets (Fig. 2.3(a)), (2) intercalated composite - d_{001} is increased by the entering polymer or other organic species, but the clay platelets remain stacked in parallel with each other (Fig. 2.3(b)), and (3) exfoliated composite - observed d_{001} is greater than 10 nm (or even undeterminable by X-ray diffraction), clay sheets are pushed apart irregularly by polymer or organic species.[92] There are different factors controlling the extent of separation of clay, such as volume percent of added clay,[114] interfacial interactions,[116] surfactant (if present in the matrix)[117] and temperature.[118]

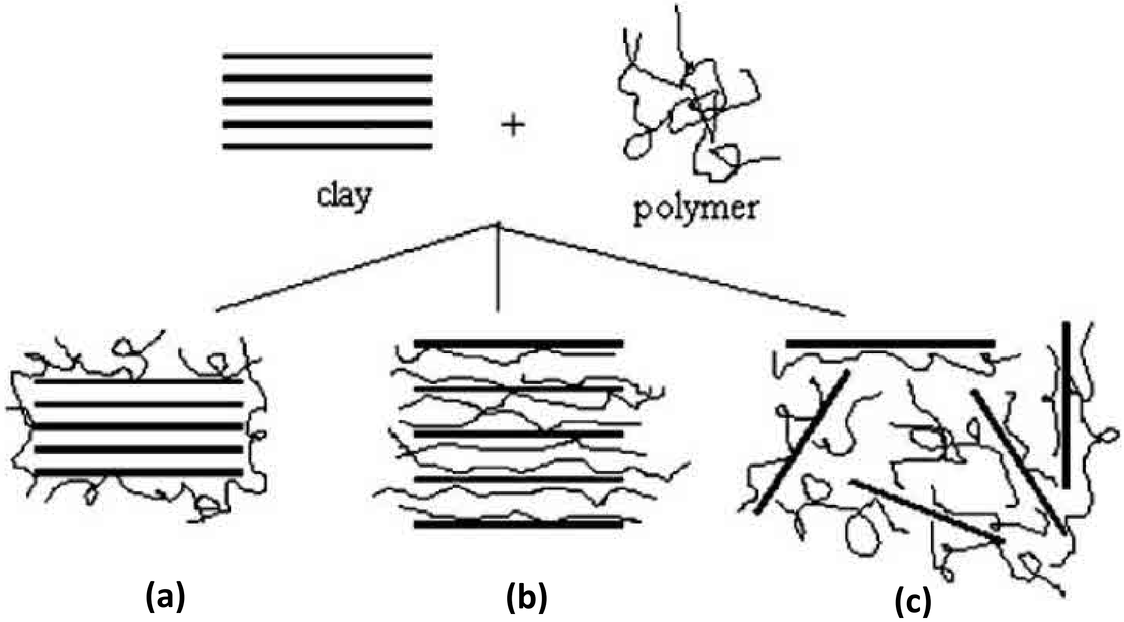

Figure 2.3. Schematics of the three different clay-filled composite morphology states: (a) conventional (b) intercalated and (c) exfoliated.[92]

The diffusion of gas molecules through a filled polymer can be viewed as a solution-diffusion process, described by Equation 2.1, with the assumption that there is no property change from the interaction between penetrant and filler.[119] In this case, the solubility of the composite is:

$$S = S_0(1-\phi) \tag{2.6}$$

where S_0 is the solubility of the neat polymer and ϕ is the volume fraction of filler in the polymer matrix. Assuming the nanofillers is impermeable, and changes the diffusion path, the diffusivity can be showed as:

$$D = D_0 F \tag{2.7}$$

where D_0 is the diffusivity of neat polymer and F is the tortuosity factor, which depends on the aspect ratio of the filler (α), and its orientation in the polymer matrix. Combining Equations 2.6 and 2.7 gives the permeability of a filled polymer composite:

$$P = DS = D_0 S_0 F(1-\phi) = P_0(1-\phi)F \tag{2.8}$$

$$F = \frac{P}{P_0(1-\phi)} \tag{2.9}$$

The reciprocal of F is the tortuosity (τ) of the composite material, which was described by Nielson as:[85]

$$\tau = 1 + \frac{L}{2W}\phi = \frac{1}{F} \tag{2.10}$$

where L and W represent the width and thickness of the platelet filler, as shown in Figure 2.4. The model assumes the length of each platelet is infinite. With the understanding that aspect ratio is L/2W, Equation 2.10 can be written as:

$$\tau = 1 + \alpha\phi \tag{2.11}$$

Platelet-like fillers are recognized as impermeable objects and the polymer phase is permeable. When gas molecules move in the direction perpendicular to the orientation of the platelets, they need to wiggle around the platelets until finding a permeable slit to pass through (Fig. 2.4). Combining Equation 2.9, 2.10 and 2.11, the permeability of filled polymer is:

$$P = \frac{P_0}{\dfrac{1+\alpha\phi}{1-\phi}} \approx \frac{P_0}{1+\alpha\phi} \qquad (2.12)$$

Nielsen's model describes a composite with low filler volume fraction, so the denominator of Equation 2.12 can be simplified as shown above.

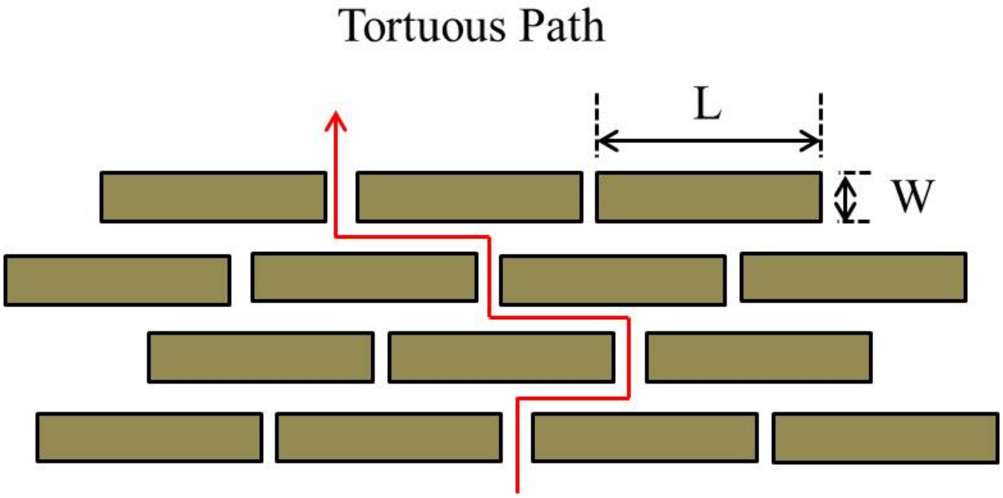

Figure 2.4. Schematic of gas transport through a polymer-platelet composite via a tortuous path.

A more advanced tortuous path theory was later proposed by Cussler,[86] stating the relationship between the permeability of a filled polymer matrix and neat polymer as:

$$P = \frac{P_0}{1 + \mu\alpha^2\phi^2 / (1-\phi)} \tag{2.13}$$

where μ is a geometric factor that is controlled by the shape of the filler. The difference between the Nielsen and Cussler models is the former failed to describe higher concentration regimes in the composite. Fredrickson defined two different regimes in a filled polymer composite.[103] When $\alpha\phi \ll 1$ and $\alpha \gg 1$, the composite is in a dilute regime, where the distance between each platelet is larger than its width. When $\alpha\phi \gg 1$ and $\alpha \gg 1$, the composite is in a semi-dilute regime, where the aspect ratio of the platelet is so large that platelets overlap with each other. Cussler's model can fit both of the regimes, while Nielsen's model only applied to the dilute regime.[120] The distribution of platelets in a polymer composite can also affect the permeability. When the platelets are in a regular array, meaning all platelets are regularly spaced, μ=1. When the platelets are in a random array, meaning the platelets are randomly distributed, μ=4/9. Schematics of regular and random arrays are shown in Figure 2.5.

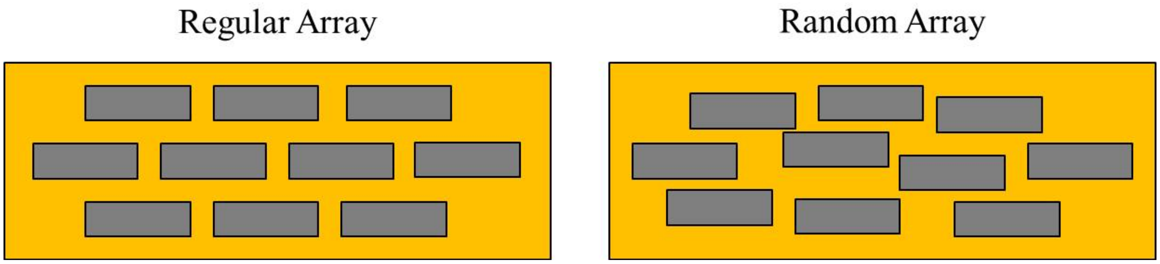

Figure 2.5. Geometries of regular and random arrays for platelet-filled polymer composites.

2. 2 Gas Barrier Films and Composites

The demand for high barrier materials that are thin, transparent, and low cost is driving the search for new technologies.[121] Food, cosmetics, pharmaceuticals, automobile parts, flexible displays, solar cells and electronics would benefit from these new packaging materials.[73, 122-124] Various gas barrier technologies, reviewed in this section, have already been developed to satisfy these applications. Polymer blending is an effective way to incorporate high barrier into bulk materials, as described in Section 2.2.1.[125] Coatings are another approach to reduce the gas permeation through various substrates, which offers multiple advantages over comparable bulk materials (e.g., light weight, transparency, low cost and freedom of design).[124, 126] These coatings include metalized plastics (Section 2.2.2),[127] metal oxide films (Section 2.2.3)[128] and polymer-clay composites (Section 2.2.4),[114] but each system has some drawbacks. In contrast, layer-by-layer assembly, provide excellent gas barrier performance, and most of the advantages from the coating techniques just described, without disadvantages like cracking and haziness.[129] LbL coating is the focus of this dissertation and will be discussed in more detail in Section 2.3.

2.2.1 Polymer Blends

Blending is a straightforward method to reduce the gas permeation by combining two different polymers, mostly by adding a limited amount of high barrier polymer into higher permeability matrix.[3] This is a less complicated process, so the production cost is lower than co-extrusion or co-injection.[121] Normally the blends properties fall between the individual polymers, but better barrier sometimes occurs from a synergistic effect.[130] A common objective of blending is to improve the insufficient properties, while keeping the desirable properties of the major polymer. Most polymers are immiscible, so the barrier of a blend will be strongly influenced by the morphology of the discontinuous phase, which is related to the interaction between two polymers and experimental conditions.[131] Figure 2.6 illustrates the relationship between the permeability and morphology of a polymer blend. Similar to clay-polymer composites, the orientation of the lamellar structure is vital for creating the extended diffusion path for gas molecules, which results in a better barrier. Under the same morphological state, gas permeability in a polymer blend increases as the volume fraction of the high-barrier polymer (filler) decreases.[132]

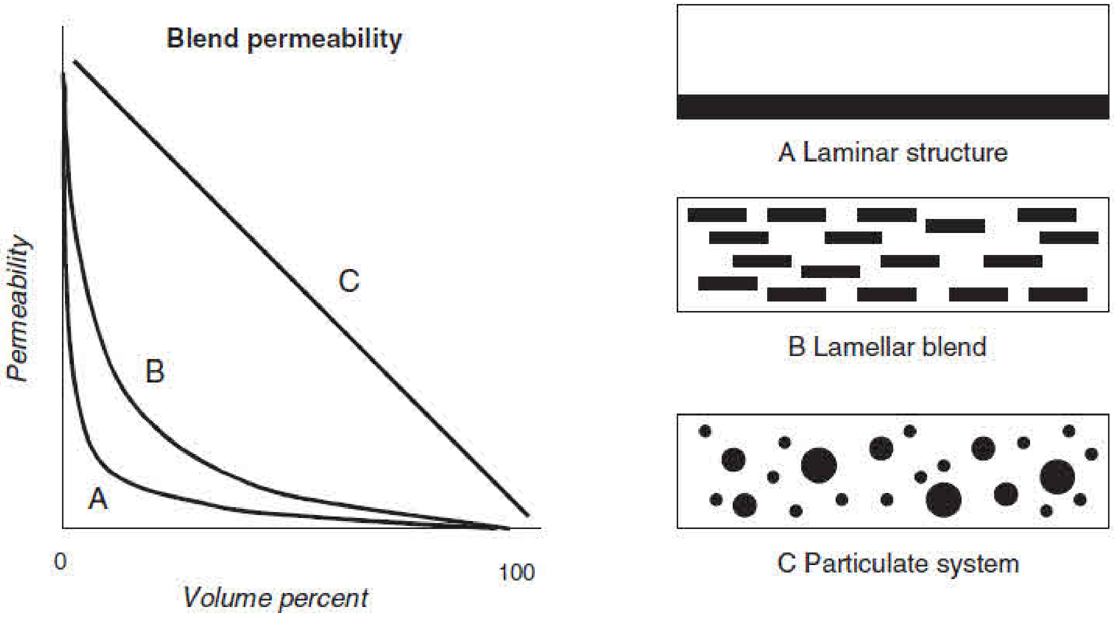

Figure 2.6. Schematic of gas permeability of a polymer blend as a function of the morphology and concentration of the high barrier phase.[121]

High barrier polymers, such as ethylene vinyl alcohol (EVOH), liquid crystal polymer (LCP) and polyethylene naphthenate (PEN), act as fillers when blended with matrix polymers like polyethylene (PE),[133] polyamide (PA),[134] polypropylene (PP)[132] and poly(ethylene terephthalate) (PET).[135] The gas barrier can be improved 2 to 10 times relative to the matrix when the appropriate morphologies are obtained, typically with a volume fraction between 5 ~ 30%.[121] This improvement is not significant relative to other techniques, but inexpensive processing has made it one of the most prevalent forms of commercial packaging material.[3]

2. 2. 2 Metalized Plastics

Depositing thin metal layers on polymeric substrates is a widely used method to create high barrier film for food packaging since the 1970s.[123, 136, 137] Metalization is performed with a vacuum web metalizer, which can evaporate pure metal molecules (e.g. Al) onto a polymeric web under high vacuum conditions.[138] The deposited thickness is in the 10-100 nm range and the oxygen permeability is reduced by three orders of magnitude relative to the uncoated substrate.[139] Some drawbacks of metalized plastic include opacity, poor flexibility, pinholes and poor adhesion to polymer film. The presence of metal also limits microwavability and recyclability. Metal oxide films are a related technology that avoids some of these limitations.

2.2.3 Metal Oxide Films

Originally commercialized in 1969,[140] metal oxide films provide an alternative to metalized plastics by providing transparent gas barrier for protecting a variety of pharmaceutical and food products.[141] Oxide thin films are also good moisture and aroma barriers that can improve food shelf life. Organic light-emitting devices (OLED) and other organic electronics also use metal oxide films for encapsulation because they are often sensitive to oxygen gas and water vapor.[139, 142] Silicon oxide (SiO_x) and aluminum oxide (Al_yO_z) are the two most common materials for gas barrier coatings. A number of processing techniques are used to coat these metal oxides onto a polymeric substrate, such as physical vapor deposition (PVD)[143], which includes evaporation[144-146] and sputtering,[147, 148] and plasma-enhanced chemical vapor deposition (PECVD).[137, 149-152] PECVD is the best method because it can precisely control the thickness, operate at low temperature environment, and produces the greatest barrier improvements compared to the other methods.[139, 140] A comparison of PECVD barrier relative to other techniques is shown in Figure 2.7.

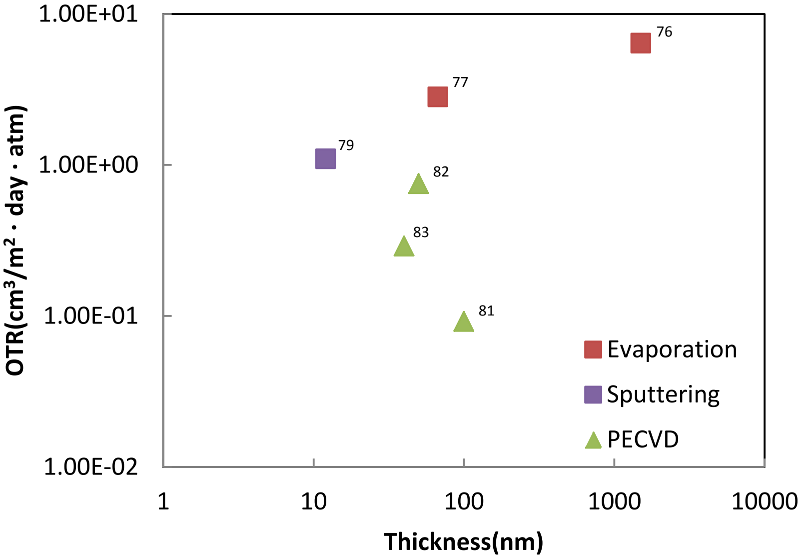

Figure 2.7. Oxygen transmission rate as a function of thickness comparisons of different SiO_x coating techniques.

Bare PET has an oxygen permeability on the order of 10^{-15} $cm^3 \cdot cm / cm^2 \cdot s \cdot Pa$ that depends on crystallinity and orientation.[140] With 100 nm of SiO_x, the oxygen permeability of PET is reduced to the order of 10^{-21} $cm^3 \cdot cm / cm^2 \cdot s \cdot Pa$.[146] This 6 orders of magnitude reduction is due to the lower diffusivity of dense SiO_x. A very tight Si-O lattice leads to oxygen diffusivity in bulk SiO_2 of 10^{-15} cm^2/s at 1500 °C, while PET has oxygen diffusivity of 10^{-9} cm^2/s at 20 °C.[139] Low diffusivity means low oxygen permeability according to Equation 2.1, but the reported oxygen permeabilities of SiO_x films are often lower than the theoretical values. Pinholes are a major issue that allows oxygen to diffuse more easily through SiO_x.[128] It's been proposed that a 70 nm SiO_x layer on PET exhibits a mean pinhole diameter of about 1 μm and a mean number of pinholes about $80/mm^2$.[153] This defective barrier coating can be improved by optimizing the PECVD processing parameters[128] or laminating a defect-free polymer layer with enough thickness.[154]

2.2.4 Polymer-Clay Composites

As mentioned in Section 2.1.2, polymers filled with impermeable clay platelets exhibit improved gas barrier. Clay platelets act as gas-impermeable sheets and can be dispersed in polymer matrices in an intercalated or exfoliated state, as shown in Figure 2.8. With 1 nm thickness and an average diameter of 200 nm,[110] clay platelets help reduce the gas permeability by increasing the length of diffusion a permeating molecule must travel.[155] This extended tortuous path, created by exfoliated clay platelets in a polymer matrix, results in a low permeability.[86] Permeabilities of various gases were cut in half when 2 wt% MMT was added to a polyamide.[156] Clay-filled polyurethane,[157] epoxy,[158] polyolefin,[159] polyamide[102] and biodegradable polymers[160] all exhibit improved barrier properties.

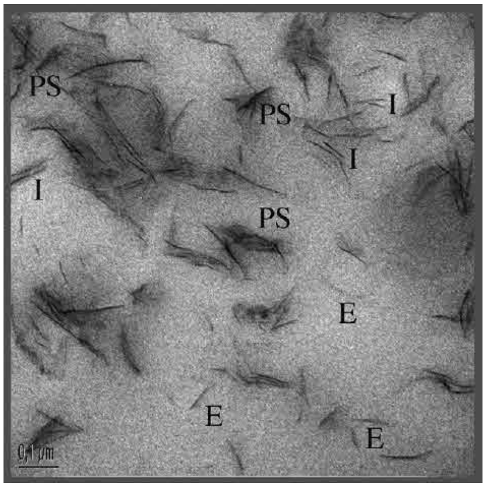

Figure 2.8. TEM of MMT platelets in polyamide composite. Phase separated (PS), intercalated (I) and exfoliated (E) platelet domains are indicated.[161]

In general, a higher volume fraction of clay results in better gas barrier,[92, 104, 155] but nanoplatelets tend to aggregate when a threshold concentration is achieved (≤ 10wt %).[104] The coexistence dilemma of high volume fraction and high gas barrier property of simple polymer-clay composites can be overcome with layer-by-layer assembly. The strong electrostatic interactions that accompany this deposition technique can dfficiently decouple single clay platelets allowing for the creation of dense composites with high concentration and exfoliation of clay platelets.[129]

2.3 Layer-by-Layer Assembly

The concept of multilayer assembly was first proposed by Iler in 1966, using cationic and anionic colloidal particles to grow multilayer films onto a glass substrate.[162] This ionic assembly methodology was later popularized by Decher and coworkers who build up multilayer films by alternatively dipping substrates into oppositely charged polyelectrolyte solutions.[163, 164] Over the past 20 years the field of layer-by-layer (LbL) assembly has grown tremendously because of the robustness, simplicity and versatility of this technique.[9, 11, 165] The LbL process is shown schematically in Figure 1.1. By exposing a charged substrate to cationic and anionic solutions, charged ingredients will be deposited onto a substrate in a layer-by-layer fashion. Although electrostatic attraction is the most common bonding type for LbL, hydrogen bonding,[13, 166] covalent bonding[167, 168] and van der Waals forces[36, 40] can also be used to grow multilayer thin films. Thermodynamically speaking, high energy is required for forcing two different polymer or particles to stay in a nano-sized, homogeneous region, but the strong inherent interactions provided by LbL from multivalent ionic complexes that stabilized such structures. The advantage of this "nano-blend" structure is the ability to generate dense nanocomposites with a much higher volume fraction of nanoparticles, which exceeds the capacity of traditional bulk composites.[169]

As mentioned in Chapter I, the properties of LbL films can be tailored by adjusting a multitude of experimental conditions such as molecular weight,[47, 48] concentration,[49, 50] chemistry,[51] pH,[49, 52] ionic strength,[49, 53, 170] temperature[54, 55] and deposition time[49, 56] of the exposed aqueous mixtures. One of the key advantages of LbL is the ability to control thickness and composition on the nanoscale. By adjusting the parameters mentioned above, film thickness and composition can be precisely tuned on a given substrate. Two primary growth modes have been uncovered for LbL assemblies: linear and non-linear. Very different growth can be obtained with the same number of layers, which takes this fabrication technology from nano to micro scale and further expands its versatility.

2.3.1 Linearly Growing Layer-by-Layer Assemblies

Assemblies of strong polyelectrolytes most often grow linearly. Cationic polymers, such as polyallylamine (hydrochloride) (PAH) and poly(dimethyldiallylammonium chloride) (PDDA), paired with a strong anionic polymer like poly(styrene sulfate) (PSS), results in strong electrostatic ion pairs with 1:1 stoichiometry charge overcompensation,[171] as shown in Figure 2.9(a). Polymers with high charge densities are stiff due to charge self-repulsion along their backbones. These relatively rigid chains deposit relatively discretely and result in linear growth as a function of bilayers deposited, as shown in Figure 2.9(b) for PDDA/PSS. Weak polyelectrolytes, such as polyallylamine (PAAm) and poly (acrylic acid) (PAA), will also exhibit linear growth when they are deposited at a pH that creates high charge density.[172]

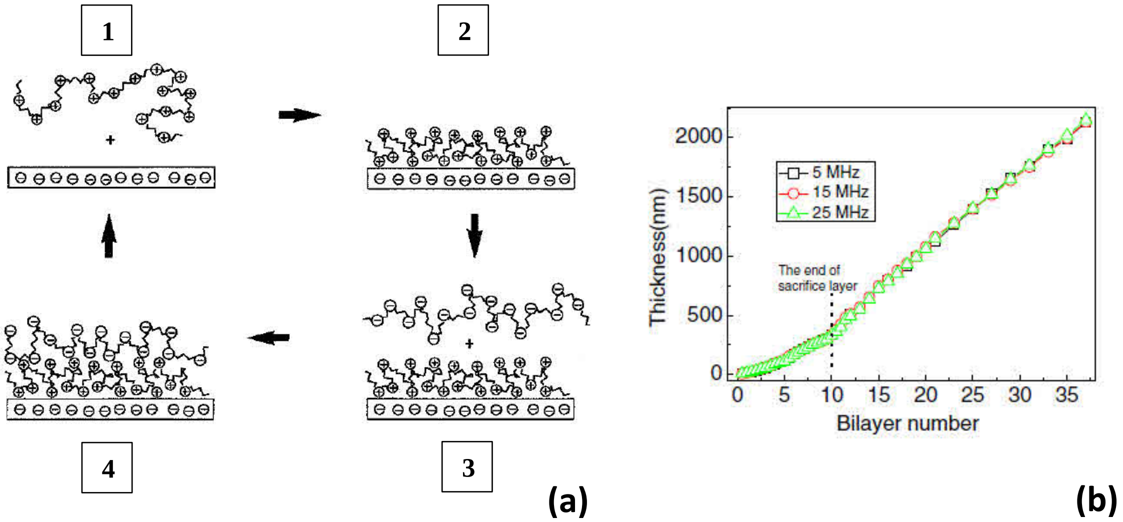

Figure 2.9. Schematic of 1:1 ratio charge overcompensation from a linearly growing layer-by-layer film (a).[9] Linear growth as a function of PDDA/PSS bilayers deposited (b).[173]

In addition to polymer-polymer LbL, charged polymers paired with non-polymer ingredients also tend to exhibit linear growth. Biomaterials such as viruses,[44, 174] DNA,[46, 175] proteins[12, 33] and nanoparticles such as colloidal silica,[176] gold,[177] silver,[178] metal oxides,[71, 179] clay,[180, 181] nanosheets[29, 31] and nanotubes,[28, 67] have all been assembled with linear growth (i.e., same amount of each ingredient in each bilayer). Figure 2.10 shows the cross-section images of poly(vinyl alcohol) (PVA)/MMT free standing film. The spacing between each two MMT layer is identical, demonstrating linear growth (Fig. 2.10(b)). This high loading polymer-MMT composite exhibits a tremendously high modulus (~125 GPa), which is comparable to a Kevlar (Fig. 2.10(a)).[182] Assemblies with only nanoparticles are also possible and only grow linearly due to their inability to interdiffuse. Charged nanoparticles have been extensively applied in layer-by-layer assembly.[176, 183-185] Laufer used a 12 nm diameter, positively charged Ludox-CL SiO_2 nanoparticle paired with two different sized negatively charged SiO_2 nanoparticles (e.g. 8 and 27 nm) to create LbL anti-flammable nanocoatings on cotton fabric.[176] Figure 2.10(c) exhibit the linear growth profile form an all nanoparticle system.

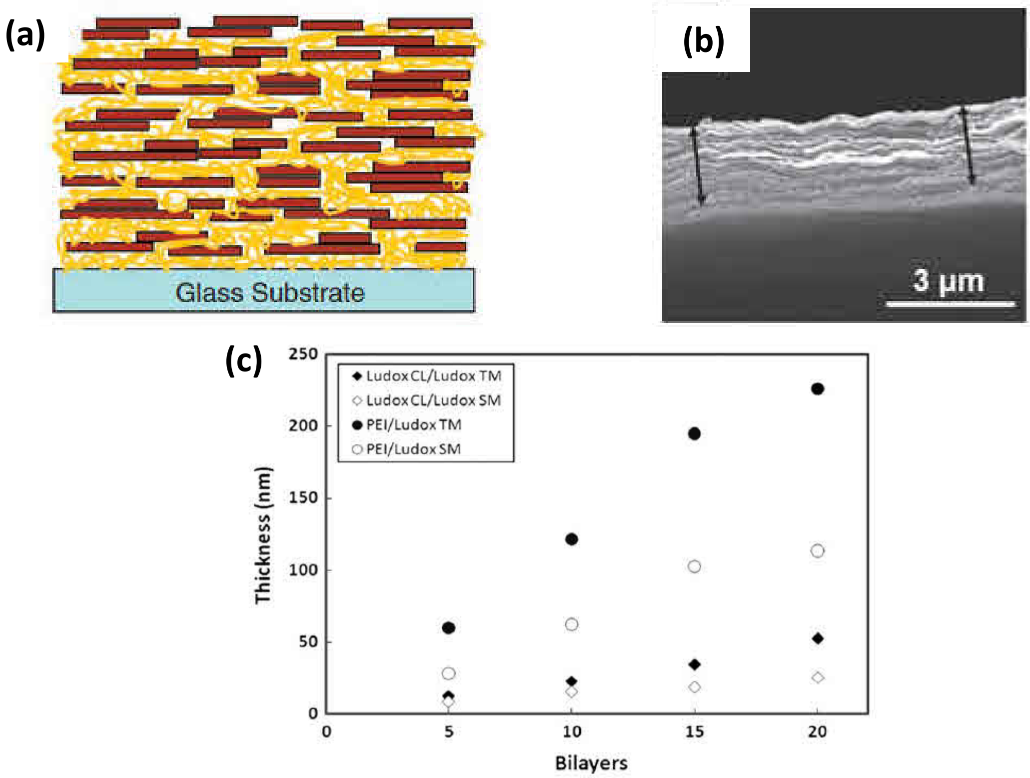

Figure 2.10. Schematic of the internal structure of PVA/MMT film (a). Cross-section SEM images of 300BL PVA/MMT films (b).[182] Thickness as a function of bilayers of silica based LbL assemblies (c).[176]

The initial clay-polymer gas barrier assemblies studied in the Polymer Nano Composites Lab exhibited linear growth as well.[8, 126, 186] Jang deposited polyacrylamide (PAm)/MMT on PET and reduced the oxygen transmission rate over three orders of magnitude (< 0.005 cc/m^2 day) with a 571 nm coating.[129] Priolo later used PEI/MMT assemblies to further reduce the film thickness necessary to achieve the same undetectable OTR.[8, 50] By increasing the MMT suspension concentration to 2 wt%, an OTR < 0.005 cc/m^2 day was achieved with a 24BL assembly (~ 120 nm thick). In this dissertation, another impermeable platelet, graphene oxide,[187] is used to impart oxygen barrier via LbL (see Chapter V). The influence of clay and polymer deposition time, on barrier behavior and growth, is also evaluated using MMT, PEI and Laponite (LAP) (see Chapter VI).[188]

2.3.2 Non-linearly Growing Layer-by-Layer Assemblies

LbL systems exhibiting non-linear growth are quite common.[12, 18, 189] Richert and coworkers came up with an "in and out" interdiffusion mechanism to qualitatively explain the non-linear growth of poly(L-lysine)/hyaluronan (PLL/HA) films.[41] After the film is dipped into the HA solution, the overall charge become negative due to the charge overcompensation. When the film contacts the positively-charged PLL solution, PLL chains overcompensate the negatively charged surface and some free PLL chains then cross the chemical potential barrier and diffuse into inner layer. The diffuse-in action continues until the equilibrium of chemical potential is reached. Rinsing with a buffer solution allows free PLL chains to diffuse out of the film, which decreases the chemical potential inside of the film. When the HA solution contacts film, the positively-charged surface again is charge overcompensated and the inner free PLL chains diffuse out to form new PLL/HA complex at the outer layer until no free PLL chains are available. Laugel and coworkers used isothermal titration microcalorimetry to test several polycation/polyanion systems and suggested an exponential growth is mainly driven by entropy.[190] Two exponentially grown LbL examples are shown in Figure 2.11.

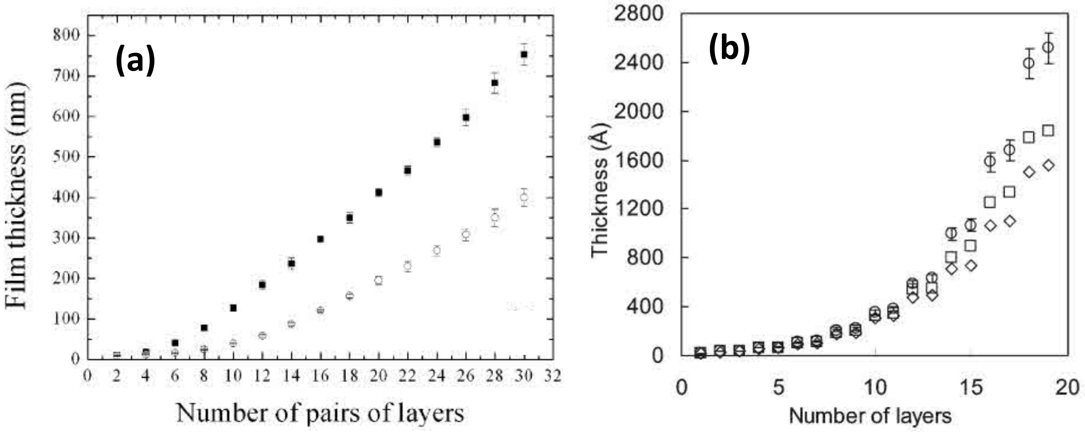

Figure 2.11. Film thickness versus number of layers for exponentially grown assemblies: PLL/HA with two different HA molecular weights of 130000 (■) and 400000 (○) (a).[191] poly(p-vinyl benzyl trimethyl ammonium)/PAA (◊), poly(p-vinyl benzyl trimethyl phosphonium) /PAA (□) and poly(p-vinyl benzyl dimethyl sulfonium)/PAA (○) (b).[192]

The exponential growth of weak polyelectrolyte pairs disrupts the heterogeneous structure, or stratified layered structure, of typical linear growth LbL films because the interdiffusion tends to homogenize the whole matrix.[193] Interaction among highly interdiffused polymers provides a more complex route for gas transport relative to traditional polymer blends. The present dissertation explores the use of exponentially growing all-polymer assemblies as gas barrier thin films (see Chapter III).[15] This work uses PEI/PAA assemblies and was inspired by the exceptional barrier of exponentially grown PEI/PAA/PEI/MMT quadlayers.[107] The influence of crosslinking is also systematically studied as a function of various experimental conditions (see Chapter IV). These polymer-only think films exhibit unprecedented gas barrier, especially considering the lack of impermeable nanoparticles.

CHAPTER III

SUPER GAS BARRIER OF ALL-POLYMER MULTILAYER THIN FILMS*

3.1 Introduction

Many LbL systems show linear growth as a function of layers deposited, but those containing weak polyelectrolytes (e.g., polyethylenimine (PEI) and polyacrylic acid (PAA)) often exhibit exponential growth.[56, 194] It is suggested that this exponential thickening effect comes from an "in and out" diffusion mechanism,[41, 191, 195] involving an endothermic polycation/polyanion complexation process.[190] Polymer chains not only adsorb onto the film's surface but also interpenetrate into inner layers for charge overcompensation, which exponentially increases the total film thickness. Weak polyelectrolyte multilayer assemblies have been widely studied because the charge density along the polymer chain can be altered with pH.[8, 52, 196] Previous research using poly(allylamine hydrochloride) (PAH) and PAA shows the ability to systematically control the thickness, density, composition and wettability by simply changing the charge density of these polyelectrolytes.[18, 52, 172] The ability to tailor charge density with pH provides a more tailorable LbL process. More recently, this concept was applied to clay-polymer assemblies that exhibit tunable gas permeability by changing the charge density of PEI.[8] The resulting nano-brick wall structure exhibits high oxygen barrier that is unrivaled by any other type of polymer or composite (or even SiO_x).

---

*Reprinted with permission from "Super Gas Barrier of All-Polymer Multilayer Thin Films" by You-Hao Yang etc., *Macromolecules* **2011**, *44*(6), 1450-1459. © 2011 American Chemistry Society.

In an effort to find an all-polymer multilayer gas barrier, PEI/PAA assemblies with different pH combinations (10/4, 8/6, 7/7 and 4/4) were studied. Thickness, density, and oxygen permeability can all be tailored by changing the pH values of aqueous PEI and PAA solutions. The thickest films are produced when both polymers have the lowest charge (10/4 for PEI/PAA), whereas a highly charged combination (7/7) is much thinner. Cross-sectional TEM shows a homogeneous structure without any discernible boundaries between layers in any of the films. The thickest PEI/PAA film (~ 1 μm thick at 10BL) exhibits an undetectable oxygen transmission rate (< 0.005 cc/m$^2 \cdot$ day), while maintaining complete transparency. The 8BL PEI/PAA (10/4) coating exhibits a permeability below 4.8×10^{-21} cm$^3 \cdot$ cm/cm$^2 \cdot$ s $\cdot$ Pa, which is believed to be the lowest permeability of an all-polymer film ever reported. Although oxygen permeability of this system is higher than polymer-clay assemblies (due to layer thickness),[8] it requires a similar number of layers to achieve a high oxygen barrier. This relatively simple recipe may be of use for a variety of packaging applications, including flexible electronics that require high flexibility and transparency (in addition to high barrier).

3.2 Experimental

3.2.1 Preparation of Deposition Mixtures

Branched polyethylenimine (PEI) (Aldrich, St. Louis, MO) (M_W ~ 25,000 g/mol) is a cationic polymer that was dissolved into 18.2 MΩ deionized water to create a 0.1 wt% solution. The pH was adjusted from its unaltered value (~10.5) to 10, 8, 7, and 4 by adding 1.0 M hydrochloric acid (HCl). Poly(acrylic acid) (PAA) (Aldrich) (M_W ~

100,000 g/mol) is an anionic polymer that was used as a 0.2 wt% solution with 18.2 MΩ deionized water. The pH of PAA was adjusted from its unaltered value (~3.1) by adding 1.0 M sodium hydroxide (NaOH).

3.2.2 Substrates

Single-side-polished (100) silicon wafers (University Wafer, South Boston, MA) were used as deposition substrates for ellipsometry, atomic force microscopy (AFM), and scanning electron microscopy (SEM). Silicon wafers were piranha treated with 3:7 30% hydrogen peroxide to 99% sulfuric acid ratio and stored in deionized water before being used. *Caution: Piranha solution reacts violently with organic material and needs to be handled properly.* Prior to use, the silicon wafers were rinsed with acetone and deionized water. Poly(ethylene terephthalate) (PET) film with a thickness of 179 μm (trade name ST505, Dupont–Teijin) was purchased from Tekra (New Berlin, WI). A 175 μm polystyrene (PS) film (Goodfellow, Oakdale, PA) was used as a substrate for transmission electron microscopy (TEM). Both PET and PS films were rinsed with deionized water and methanol before use. Cleaned PET and PS substrates were then corona-treated with a BD-20C Corona Treater (Electro-Technic Products Inc., Chicago, IL). Corona treatment improves adhesion of the first polyelectrolyte layer by oxidizing the film surface.[197] Polished Ti/Au crystals with a resonance frequency of 5 MHz were purchased from Maxtek, Inc (Cypress, CA) and used as deposition substrates for quartz crystal microbalance (QCM) characterization.

3.2.3 Layer-by-Layer Film Deposition

The overall layer-by-layer process is shown schematically in Figure 1.1. A given substrate was first dipped into the PEI solution for 5 minutes, followed by rinsing with deionized water for 30 seconds and drying with a stream of filtered air. After the first positively-charged layer was adsorbed, the substrate was dipped into PAA solution for another 5 minutes, followed by another rinsing and drying cycle. Starting from the second deposition cycle, the remaining numbers of bilayers were created using one minute dip times. This process was carried out using home-built robot systems.[181, 198] The pH of PEI or PAA is shown as a subscript next to their initials in the figures and text. For example, one bilayer of PEI(pH=10)/PAA(pH=4) is abbreviated as $(PEI_{10}/PAA_4)_1$.

3.2.4 Thin Film Characterization

Assembly thickness on silicon wafers was measured every five bilayers with a PHE-101 Discrete Wavelength Ellipsometer (Microphotonics, Allentown, PA). A 632.8 nm laser was used at an incidence angle of 65°. For the PEI_{10}/PAA_4 system, thickness was measured with a P-6 profilometer (KLA-Tencor, Milpitas, CA). The average thickness was calculated from three 0.01 m 2-D measurements. Mass increments were measured each layer with a Research Quartz Crystal Microbalance (QCM) (Inficon, East Sycrase, NY) with a frequency range of 3.8 - 6 MHz. The 5 MHz quartz crystal was inserted in a holder and dipped into the PEI and PAA solutions. After each deposition, the crystal was rinsed and dried and then left on the microbalance to stabilize for 5 minutes. Cross-sections of the PEI/PAA assemblies were imaged with a JEOL 1200 EX TEM (Mitaka, Tokyo, Japan), operated at 110 kV. Samples were prepared for imaging by embedding a piece of PS, supporting the LbL film, in epoxy prior to sectioning it with a diamond knife. Surface structure of the coated silicon wafers were imaged with a Multimode Scanning Probe Microscope (SPM or AFM) (Veeco Digital Instruments, Santa Barbara, CA) in tapping mode. OTR testing was performed by MOCON (Minneapolis, MN) in accordance with ASTM D-3985,[199] using an Oxtran 2/21 ML instrument at 23°C and 0% or 100% RH. Glass transition temperature (T_g) was measured by a Q20 differential scanning calorimeter (DSC) (TA Instruments, New Castle, DE). 5 - 10 mg samples were placed in aluminum pans and scanned from -50 to 150 °C at a heating and cooling rate of 10 °C/min.

3.3 Results and Discussion

3.3.1 Film Growth

Film growth of four different PEI/PAA pH combinations (PEI_4/PAA_4, PEI_7/PAA_7, PEI_8/PAA_6 and PEI_{10}/PAA_4) was measured by ellipsometry and profilometry, as shown in Figure 3.1. The growth rate of PEI_{10}/PAA_4 is the greatest (thickest) among all the pH combinations studied, achieving a thickness of 4.74 μm at 30 bilayers. The thickness order of the other pH combinations is 8/6 (890 nm) > 4/4 (349 nm) > 7/7 (90 nm) (Fig. 3.1(b)). These thickness differences are attributed to the inherent pH-responsive morphology of the weak polyelectrolytes and the interactive charge overcompensation from the basic PEI and acidic PAA solutions. As these polymers become highly charged (at low pH for PEI and high for PAA), they undergo intra-segmental repulsion and deposit thinner layers. With lower charge, PEI and PAA remain more loopy or coiled due to intra-molecular van der Waal attractions.[52] In terms of interactive charge overcompensation, the pK_a of PAA is very sensitive to local pH,[52, 172] so the basic PEI solution will make PAA segments more charged. The same scenario occurs with PEI, which exhibits an increased charge density when exposed to the acidic PAA solution. Once the charge density is increased, more charged groups are needed for overcompensation. As this process continues, with each deposition step, more PEI and PAA are adsorbed, resulting in the dramatic increase in film thickness as a function of layers deposited.

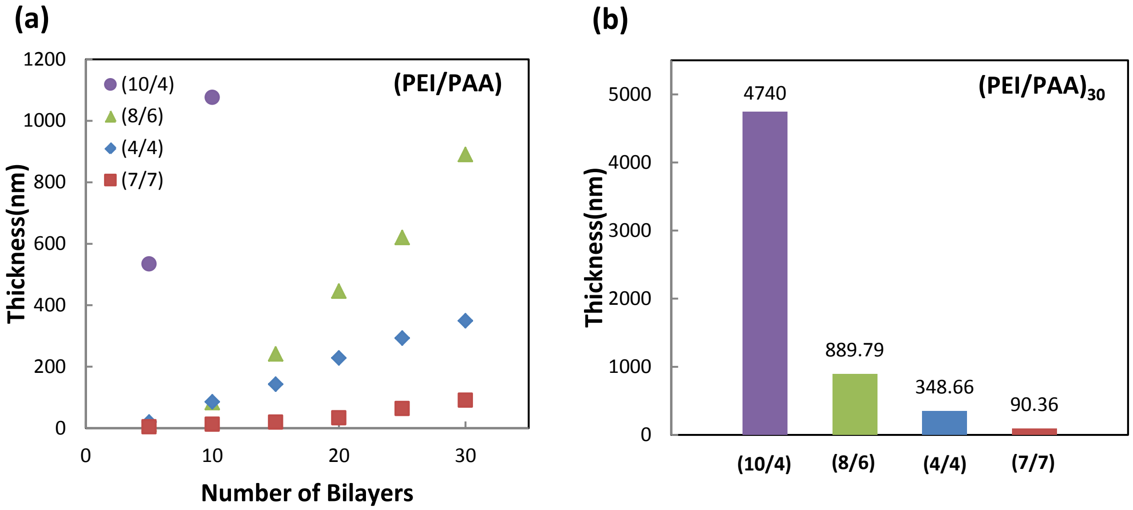

Figure 3.1. Film thickness as a function of bilayers deposited for LbL assemblies made with varying pH combinations of PEI and PAA (a). Thickness of 30BL PEI/PAA films with varying pH combinations (b). The numbers in parenthesis are the deposition pH of PEI and PAA solutions, respectively.[15]

It is interesting to observe that $(PEI_8/PAA_6)_{30}$ is 155% thicker than $(PEI_4/PAA_4)_{30}$ (Fig. 3.1(b)). Considering the inherent pH-responsive morphology of these polymers, PEI_8 has a more loopy/coiled conformation than PEI_4 and PAA_4 has a more loopy/coiled conformation than PAA_6. In (8/6), the nonioinized segments of PEI or PAA are continuously titrated by the oppositely charged polymer solution during the deposition process. This titration process results in more charged groups from PEI and PAA being required for charge overcompensation, which adds more PEI and PAA chains and results in a thicker film. For (4/4), the local titration is expected to have less impact than (8/6). In other words, the overall (4/4) film thickness is primarily controlled by the intrinsic conformations of PEI and PAA. For (7/7), both PEI and PAA are in their highly charged state, without the influence of local titration, which results in the smallest thickness (90 nm) for 30 bilayers. The fact that the thickness of $(PEI/PAA)_{30}$ can be altered by nearly two orders of magnitude, from 4.74 μm to 90 nm by simply changing the pH, highlights the significant tailorability of these LbL assembled thin films.

The mass of each deposited polymer layer was measured with a QCM, as shown in Figure 3.2. Similar to the observed thickness growth (Fig. 3.1(a)), the mass increase as a function of layers deposited is greatest for the PEI_{10}/PAA_4 system. In the case of mass, the growth is initially not linear, but gradually becomes more linear (as observed by others).[12] The PEI_8/PAA_6 and PEI_4/PAA_4 systems exhibit similar growth, while PEI_7/PAA_7 again shows the least growth relative to all other pH combinations. The average mass deposited for each PEI_{10}/PAA_4 bilayer is 15.9 $\mu g/cm^2$, which is about three times higher than PEI_8/PAA_6 (~5.1 $\mu g/cm^2$) and PEI_4/PAA_4 (~4.4 $\mu g/cm^2$). As for

PEI_7/PAA_7, there is only 1.2 μg/cm^2 deposited every bilayer. The dramatic difference between 10/4 and 8/6 come from the interactive charge overcompensation described above. A smaller pH difference for 8/6, relative to 10/4, causes the amount of charged groups ionized by the oppositely charged polymer solution to also be smaller. This reduced level of ionization requires fewer polymer chains to be needed for charge overcompensation, in the 8/6 system, resulting in reduced mass growth relative to 10/4. In addition to verifying growth, QCM provides the composition of each pH combination. PEI_{10}/PAA_4 is 58 wt% PEI (average value for measurements between 10 and 20BL), while PEI_8/PAA_6 contains only 31 wt% PEI. PEI_4/PAA_4 and PEI_7/PAA_7 have 46 wt% and 71 wt% PEI, respectively. The dramatic composition change from 8/6 to 7/7 shows that although the charge density of PEI and PAA both increase from 8/6 to 7/7, the adsorption of charged PAA is weaker than charged PEI.

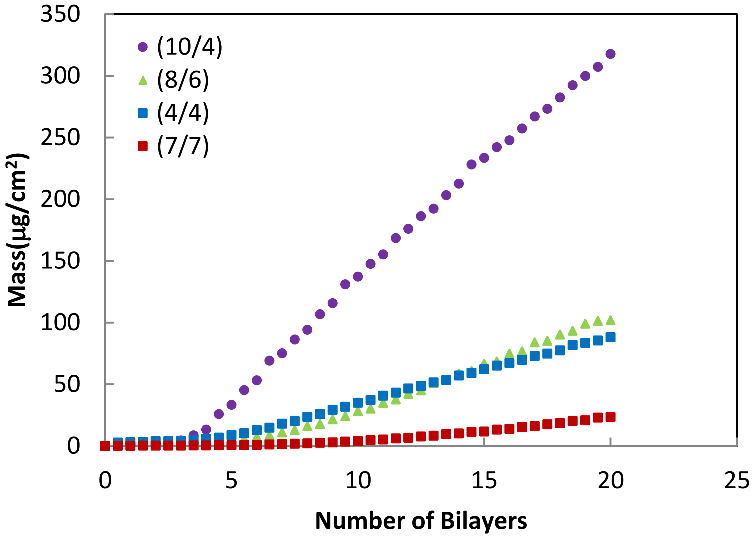

Figure 3.2. Mass as a function of layers deposited for assemblies made with varying pH combinations of PEI and PAA.[15]

3.3.2 Film Morphology

TEM cross-sectional images of $(PEI/PAA)_{20}$, made with various pH combinations, are shown in Figure 3.3. All four films were deposited on PS to facilitate sectioning. These images show the difference in thickness, with regard to pH combinations, that was discussed in the previous section. The thickness order is $PEI_{10}/PAA_4 > PEI_8/PAA_6 > PEI_4/PAA_4 > PEI_7/PAA_7$, which agrees with ellipsometer and profilometer measurements (Fig. 3.1). The homogeneity of these images suggests a high level of interdiffusion between PEI and PAA that eliminates the boundaries between each layer.

AFM surface images of $(PEI/PAA)_{10}$ and $(PEI/PAA)_{10.5}$ are shown in Figure 3.4. $(PEI_8/PAA_6)_{10}$ (Fig. 3.4(b)) and $(PEI_7/PAA_7)_{10}$ (Fig. 3.4(c)) both exhibit smooth surfaces, while $(PEI_{10}/PAA_4)_{10}$ (Fig. 3.4(a)) and $(PEI_4/PAA_4)_{10}$ (Fig. 3.4(d)) have an ordered surface texture. Both polymers in PEI_{10}/PAA_4 have low charge, which results in a more interdiffused morphology. During layer-by-layer assembly, these two globular polymers enhance the uneven topography that occurs in all films. PEI_8/PAA_6 and PEI_7/PAA_7, with more highly charged polymers, exhibit a smoother surface due to more extended (thinner) polymer chains. As for PEI_4/PAA_4, with a combination of highly charged PEI and weakly charged PAA, there is a reduced texture relative to PEI_{10}/PAA_4. With PAA in the outmost layer, this texture is enhanced. On the other hand, PEI in its highly charged state effectively suppresses the texture, as evidenced by the relatively smooth surface of $(PEI_4/PAA_4)_{10.5}$ (Fig. 3.4(f)), in which the outmost layer is PEI instead of PAA. Even for relatively rough $(PEI_{10}/PAA_4)_{10.5}$ (Fig. 3.4(e)), the outer PEI layer seems to cover up most of the surface texture.

In general, higher charged polymer combinations have smoother surfaces and less charged combinations have rougher surfaces. The order of surface roughness is PEI_{10}/PAA_4 (49.1 nm) > PEI_4/PAA_4 (5.9 nm) > PEI_8/PAA_6 (4.3 nm) > PEI_7/PAA_7 (2.1 nm), which were all measured with a 20 μm × 20 μm area. For 10.5 bilayers, the change of surface organization due to the outmost layer can be clearly seen. In PEI_{10}/PAA_4, the less charged PEI covers up the rough surface created by weakly charged PAA that decreases the surface roughness 42% (from 49.1 nm to 28.3 nm). On the other hand, when the outmost layer of PEI_4/PAA_4 is changed from a less charged PAA to highly charged PEI, there is a 25% decrease in surface roughness (from 5.9 nm to 4.4 nm). From the above results, two things can be inferred: (1) in a weakly charged state, PEI creates a smoother surface than PAA and (2) interdiffusion of PEI and PAA will not change the surface morphology dictated by the outmost layer. One can control the surface roughness of PEI/PAA assemblies simply by changing the charge density of each polymer and the outmost layer, which could be useful for self-healing and superhydrophobic films. In the present study, it is low oxygen permeability that is sought.

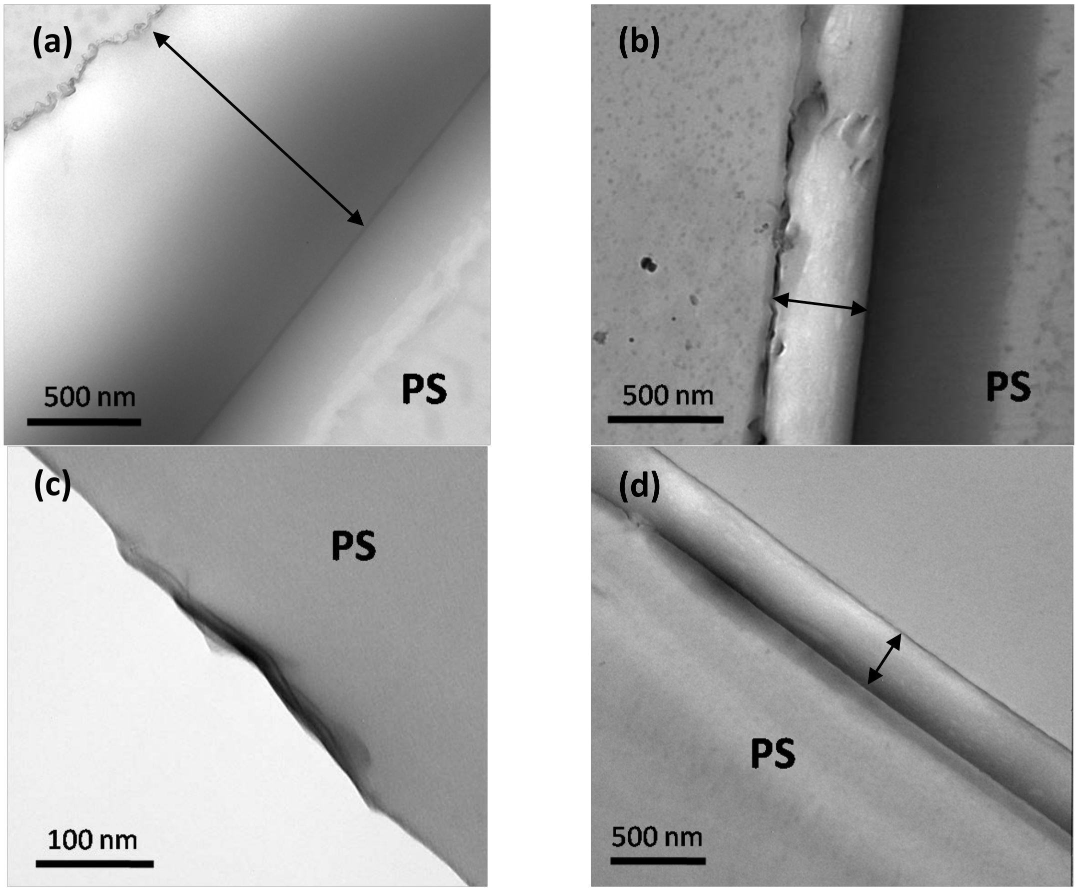

Figure 3.3. TEM cross-sectional images of $(PEI/PAA)_{20}$ on PS made with various pH combinations: PEI_{10}/PAA_4 (a) , PEI_8/PAA_6 (b), PEI_7/PAA_7 (c) and PEI_4/PAA_4 (d). The double arrow bars highlight the thickness of the films.[15]

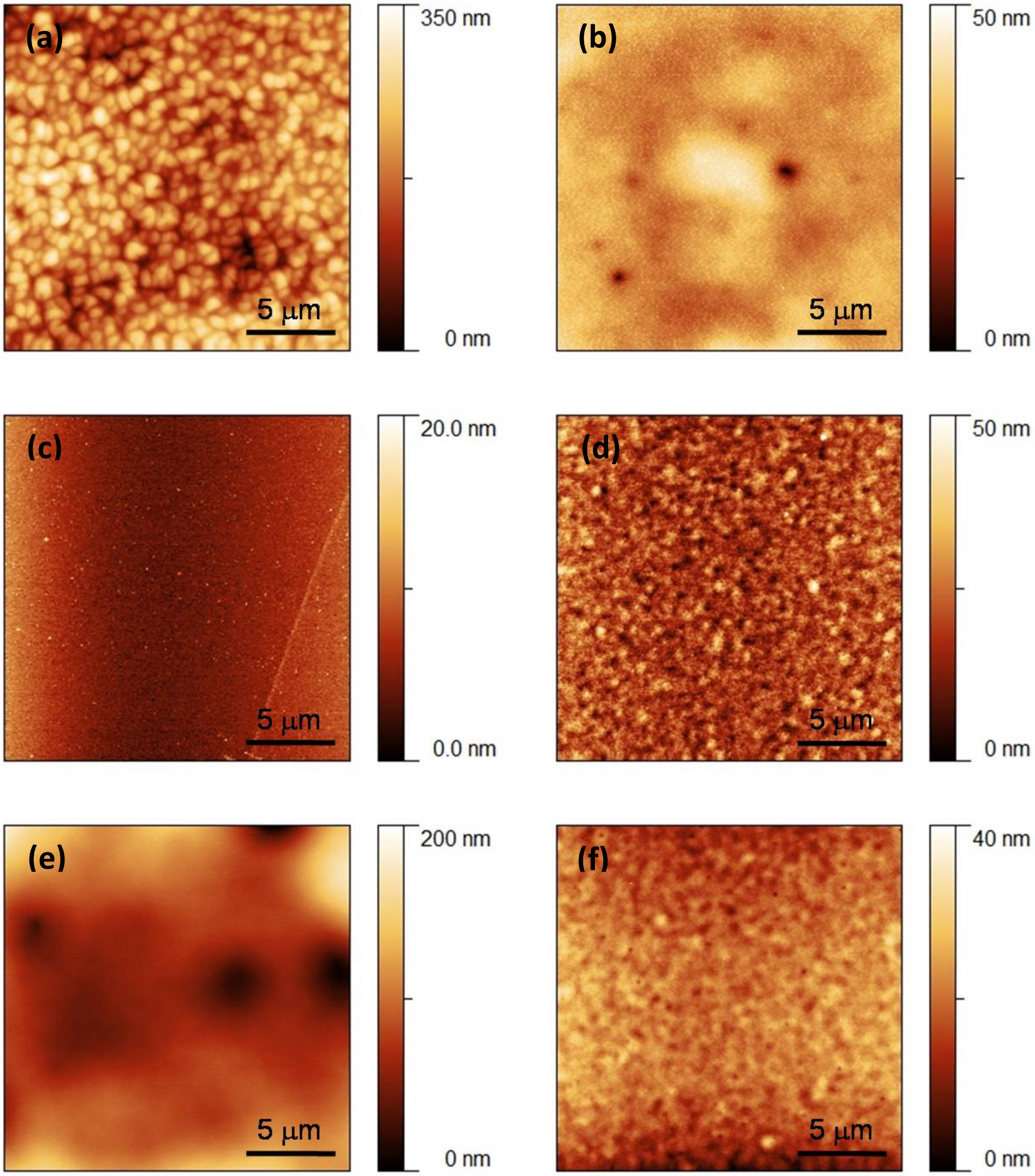

Figure 3.4. AFM height images of $(PEI/PAA)_{10}$ on Si wafers: PEI_{10}/PAA_4 (a) , PEI_8/PAA_6 (b), PEI_7/PAA_7 (c) and PEI_4/PAA_4 (d). Two PEI-terminated surfaces, $(PEI_{10}/PAA_4)_{10.5}$ (e) and $(PEI_4/PAA_4)_{10.5}$ (f), are also shown.[15]

3.3.3 Oxygen Barrier

Oxygen transmission rates for PEI_8/PAA_6, PEI_7/PAA_7 and PEI_4/PAA_4 films show little improvement relative to uncoated PET (OTR > 8.45 $cc/m^2 \cdot$ day for assemblies on 175μm thick PET film). Only the PEI_{10}/PAA_4 system exhibits low OTR with fewer than 10 bilayers, as summarized in Table 3.1 and Figure 3.5(a). Various numbers of PEI_{10}/PAA_4 bilayers were tested at 23 °C and 0 or 100% RH. In the case of 0% RH, 8BL films achieve an undetectable oxygen transmission rate (< 0.005 $cc/m^2 \cdot$ day), which is more than three orders of magnitude lower than uncoated PET film (OTR = 8.48 $cc/m^2 \cdot$ day). In the case of 100% RH, the OTR of an 8BL film increases from undetectable (< 0.005) to 0.09 $cc/m^2 \cdot$ day, while the other systems exhibit significantly higher values than at 0% RH (Fig. 3.5(b)). At 10 bilayers, the OTR remains undetectable at 100% RH (Table 3.1). In general, thicker films exhibit lower oxygen transmission rates. A thicker film has a longer diffusion pathway, which takes longer for oxygen molecules to travel through and causes them to have more interactions (e.g., H-bonding with the polymers). By increasing the number of bilayers from 6 to 8, the OTR is improved by more than three orders of magnitude. The significant OTR difference between 6 and 8 bilayers is largely due to the exponential growth of PEI/PAA (i.e., greater thickness). It is assumed that the films swell at 100% RH,[200, 201] which increases free volume and subsequently increases OTR.

Table 3.1. Oxygen permeability of PEI_{10}/PAA_4 assemblies on PET film at 23°C.

Recipe	OTR ($cc/m^2 \cdot day \cdot atm$)		Film Thickness (nm)	Permeability($\times 10^{-16} \cdot cm^3 \cdot cm/cm^2 \cdot s \cdot Pa$)	
	0% RH	100% RH		Film[a]	Total
Bare PET	8.48	8.48	N/A	N/A	17.3
$(PEI/PAA)_{10}$	<0.005[b]	<0.005	1080	<0.00006[b]	<0.0096
$(PEI/PAA)_8$	<0.005	0.61	451	<0.000048	<0.0096
$(PEI/PAA)_6$	3.75	3.83	369	0.057	7.70

[a] Film permeability was decoupled from the total permeability using a previously described method.[146]

[b] The low end detection limit for an Ox Tran 2/21 L module is 0.005 $cc/m^2 \cdot day$.

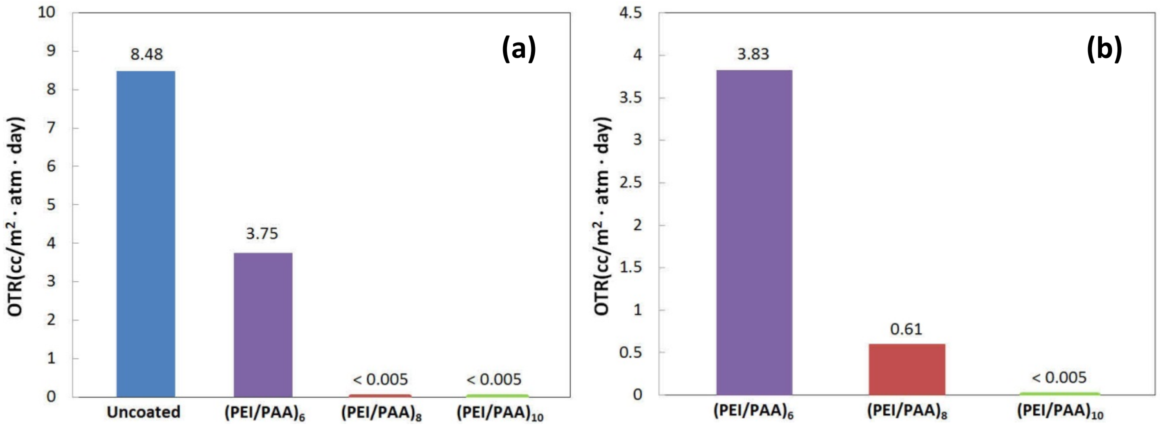

Figure 3.5. Oxygen transmission rate of PEI_{10}/PAA_4 films on PET at 0% (a) and 100% RH (b).

3.3.4 Glass Transition Temperature

Polyelectrolyte complexes can exhibit two extreme morphologies: a “ladder-like” structure or a “scrambled egg” structure.[202] The former is composed of two polyelectrolytes orderly packed by mutual charge compensation with cooperative effects, which is most favorable in a 1:1 stoichiometry of linear components. The scrambled egg structure is composed of randomly aggregated and oppositely charged polyions with partial charge compensation. The remaining ionic sites are charge-compensated by other counterions. Based upon the composition, thickness and microstructure data presented here, the PEI_{10}/PAA_4 film is believed to be closer to the scrambled egg structure, something akin to a highly interpenetrating network.[203] PEI with positively charged (or basic) amine groups always needs to stay with negatively-charged (or acidic) groups from PAA for charge compensation. This necessary association creates numerous cation/anion (or acid/base) interfaces that contribute to a densely packed thin film.

Figure 3.6(a) shows the T_g (measured by DSC) of neat PEI, PAA and a $(PEI_{10}/PAA_4)_{200}$ free-standing film. The weight fraction of $(PEI_{10}/PAA_4)_{200}$ was estimated from extrapolated QCM results. PEI has a T_g of -25.6 °C and PAA has a T_g of 89.4 °C. T_g of the LbL film is higher than the linear additive combination of neat polymer T_g’s, indicating that the polymer chains are more restrained inside of this network. The parallel additive model, known as the Fox equation ($1/T_{g,film} = w_{PEI}/T_{g,PEI} + w_{PAA}/T_{g,PAA}$, where w’s are weight fractions of a given polymer),[204] is a reasaonable approximation for random copolymers and homogeneous polymer blends. The series model, known as the Wood equation ($T_{g,film} = w_{PEI} \cdot T_{g,PEI} + w_{PAA} \cdot T_{g,PAA}$),[205] is typically an overapproximation for copolymers and polymer blends. A positive deviation in T_g relative to these linear combination predictions, can be attributed to intermolecular hydrogen bonding between these blended polymers.[206] In the case of an assembled film, the dense scrambled egg structure has numerous interfaces between PEI and PAA. Moreover, hydrogen bonding between uncharged amine groups of PEI and hydroxyl groups of PAA further decreases the mobility of each polymer, forming a more compact structure with a smaller free volume than normal polymeric membranes.[207]

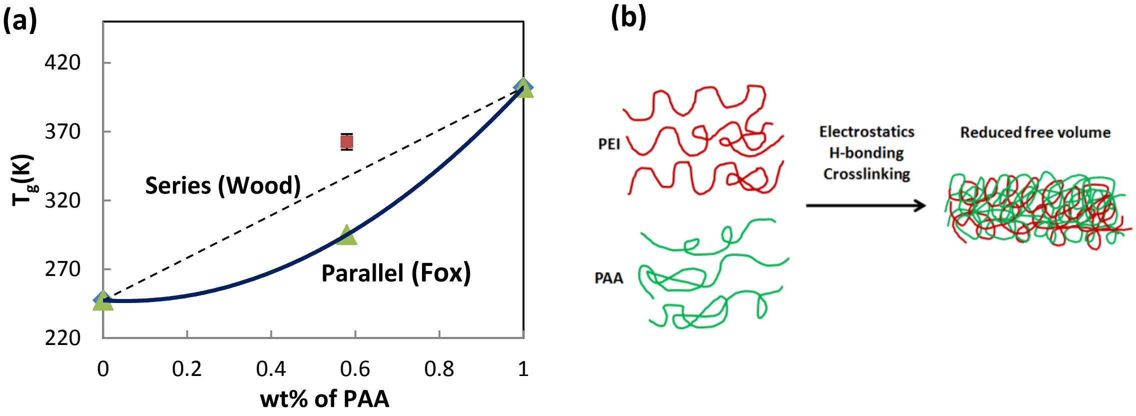

Figure 3.6 Glass transition temperature of PEI_{10}/PAA_4 compared to series (dotted line) and parallel (solid line) combinations of the two neat polymers (a). The light triangle on the parallel line is the film T_g calculated using the Fox equation. Schematic of reduced free volume in highly interdiffused PEI/PAA assemblies (b).[15]

A schematic illustration of the scrambled polymer blend is shown in Figure 3.6(b). In the PEI/PAA thin film, polymer chains are confined to a smaller volume than ordinary polymer blends due to the strong electrostatic attractions, intermolecular H-bonding and/or crosslinking. The resulting densely packed structure is the believed source of low permeability in these films. Ellipsometry reveals that the highest barrier (PEI_{10}/PAA_4) films have a higher refractive index (RI = 1.65 for an 8 BL assembly) than any of the other pH combinations (RI ~ 1.45 at 8 BL), which is suggestive of this more dense structure. The relationship between permeability and free volume can be described by Equation 2.2. Greater film density suggests the fractional free volume (Equation 2.3) of this film would be relatively small, which in turn reduces permeability (density of $(PEI_{10}/PAA_4)_{20}$ ~ 1.13 g/cm^3, where densities of PEI and PAA are 1.03 and 1.14 g/cm^3, respectively).

Other than free volume effects, hydrogen bonding between uncharged amine groups of PEI and hydroxyl groups of PAA surely contributes some barrier to oxygen.[125, 208] The permeability values in Table 3.1 were obtained by multiplying film thickness by OTR. The $(PEI_{10}/PAA_4)_8$ assemblies have an unprecedented oxygen permeability ($< 4.8\times10^{-21}$ cm^3 · cm/cm^2 · s · Pa at 23°C and 0% RH). Compared to a commercial SiO_x-coated PET, whose permeability is around 3×10^{-18} cm^3 · cm/cm^2 · s · Pa),[152] the permeability of the crosslinked $(PEI_{10}/PAA_4)_8$ film is three orders of magnitudes lower. This is believed to be the lowest gas permeability ever reported for an all-polymer film of any type.

3.4 Conclusions

Layer-by-layer assembly of PEI and PAA was performed with various pH combinations that demonstrated the thickness and compositional tailoribility of this system. Superlinear growth is observed regardless of pH. AFM images show that the surface of these films can be controlled by the outmost layer and its degree of ionization, with low pH (i.e., highly charged) PEI creating the smoothest surfaces. TEM images show homogeneous cross-sections, which suggest an interpenetrating network of PEI and PAA. Oxygen permeability of $(PEI_{10}/PAA_4)_8$ is less than 4.8×10^{-21} $cm^3 \cdot cm/cm^2 \cdot s \cdot Pa$ at a thickness of just 451 nm. The superior oxygen permeability of this all-polymer assembly can be attributed to a small free volume and the numerous interfaces created by the interpenetrating network and hydrogen bonding. Positive deviation of T_g (from the predictions of the Fox and Wood equations) for the LbL film confirms a strong association between PEI and PAA. This study marks the first all-polymer LbL assembly ever reported for oxygen barrier, which could be useful for food packaging, selective gas membranes and protection of flexible electronics.

CHAPTER IV

INFLUENCE OF CROSSLINKING ON OXYGEN AND MOISTURE BARRIER OF WEAK POLYELECTROLYTE MULTILAYER THIN FILMS*

4.1 Introduction

Electrostatic assemblies, with ionic bonding and physical crosslinks, are prone to lose some of their integrity by absorbing water or changing charge density with pH,[170, 209, 210] which leads to diminished gas barrier behavior.[8] Covalent crosslinking is an effective way to prevent this degradation of LbL thin films.[211, 212] It is known that more densely-packed molecular organization often exhibits improved mechanical behavior,[168] chemical stability,[213] conductivity,[214] and reduced oxygen or ion permeability.[215, 216] Polyelectrolyte mutilayers have already been successfully crosslinked with bifunctional aldehydes,[217, 218] carbodiimides,[219-221] anhydrides,[222] UV irradiation[211, 223, 224] and/or heat.[63, 213, 218, 225] It has been shown that heat-crosslinked poly(allylamine hydrochloride) (PAH)/poly(acrylic acid) (PAA) assemblies result in a passivating layer.[225] This same crosslinked system exhibits improved corrosion resistance,[167] modulus,[224] and ion transport selectivity.[215] As already mentioned, creating covalent bonds between amine and carboxylic acid groups also showed improved oxygen barrier in polyethylenimine (PEI) assembled with poly (acrylic acid) (PAA),[107] but there has never been a thorough

---

*Parts of this chapter are reprinted with permission from "Super Gas Barrier of All-Polymer Multilayer Thin Films" by You-Hao Yang etc., *Macromolecules* **2011**, *44*(6), 1450-1459. © 2011 American Chemistry Society.

study of the influence of crosslinking on gas permeability of these types of thin film assemblies.

In an effort to further improve the gas barrier of PEI/PAA assemblies and better understand the influence of crosslinking, glutaraldehyde (GA) was used first to study the blocking layer effect in terms of thickness and mass growth to different pH combinations (10/4, 8/6, 7/7 and 4/4). In addition to GA, 1-[3-(dimethylamino)propyl]-3-ethylcarbodiimide methiodide (EDC) and heat were examined with respect to concentration, temperature and/or time. Thickness of 10-bilayer PEI/PAA films can be tailored from 600 nm to 1300 nm using different crosslinking methods and parameters. GA and EDC showed larger film thickness with higher concentration, from 0.01 to 0.1M, while heating made films thinner as the crosslinking temperature and time were increased (up to 180 °C). FTIR spectra suggest that GA produces a higher extent of crosslinking with increasing concentration, while EDC requires lower concentration for the same crosslinking efficacy. Oxygen transmission rates at 0% and 100% RH show a strong connection between gas barrier and crosslinker concentration. 0.1M GA and 0.01M EDC exhibit the lowest OTR at 100% RH. The lowest oxygen permeability was achieved by an 8BL film crosslinked with 0.1M GA for 30 minutes. This PEI/PAA film has a 551 nm thickness and $P_{O2} < 5.9\times10^{-21}$ $cm^3 \cdot cm/cm^2 \cdot s \cdot Pa$, which is one order of magnitude lower than typical SiO_x nanocoatings.[150] Chemically-crosslinked films did little to reduce water vapor transmission rate, but a 50 BL film, thermally-crosslinked at 180 °C for 5 hours, reduces WVTR by 46% relative to the uncoated substrate. By optimizing the crosslinking conditions, one can create the best OTR and WVTR all-polymer coating. These simple post-treatments of PEI/PAA multilayers could potentially be used to improve food and flexible electronics packaging, gas separation membranes, and self-healing coatings.

4.2 Experimental

4.2.1 Materials and Substrates

Polymers and preparation of deposition mixtures were described in Section 3.2.1. Glutaraldyhyde (GA) (Aldrich) and 1-[3-(dimethylamino)propyl]-3-ethylcarbodiimide methiodide (EDC) (Aldrich) were used as crosslinking agents, in the form of 0.01, 0.05 and 0.10M aqueous solutions. Section 3.2.2 describes the substrates used in this study.

4.2.2 Film Deposition and Crosslinking

The deposition procedure used in this study was described in Section 3.2.3. Films were crosslinked by dipping into 0.01M, 0.05M and 0.1M GA or EDC solution for 3, 30 and 300 minutes. Thermal crosslinking was performed by heating the film in an oven at 120, 150 or 180°C for 1, 2, or 5 hours.

4.2.3 Film Characterization

Film growth and composition was measured using ellipsometry and QCM, respectively, as described in Section 3.2.4. In this case, crosslinked film thicknesses were measured with an alpha-SE Ellipsometer (J. A. Woollam Co., Inc., Lincoln, NE). Fourier transform infrared spectra (FTIR) were collected in the dry state with an

ALPHA-P10098-4 spectrometer (Bruker Optics Inc., Billerica, MA) in ATR mode. The FTIR analyses were done by normalizing the intensity of the band at 1548 cm^{-1} ($-COO^-$). Water vapor transmission rate (WVTR) tests were performed by MOCON with ASTM F-1249,[226] using a Permatran 3/33 G instrument (MOCON) at 23°C and 100%RH. All other characterizations are identical to those described in Section 3.2.4.

4.3 Results and Discussion

4.3.1 Film Growth of GA crosslinked PEI/PAA

PEI/PAA assemblies with four different PH combinations (10/4, 8/6, 7/7, 4/4) were crosslinked by glutaraldehyde (GA) after every ten bilayers of deposition. Figure 4.1 compares thickness growth with and without GA crosslinking. In all four systems, the films grow exponentially (or superlinearly) with and without crosslinking and all crosslinked systems are thinner than their uncrosslinked counterparts. These thickness trends suggest that different pH combinations exhibit different extents of crosslinking. The 30BL PEI_4/PAA_4 film exhibits an 11% thickness reduction, following crosslinking every ten bilayers, relative to an uncrosslinked film. For the same number of bilayers, PEI_7/PAA_7, PEI_8/PAA_6 and PEI_{10}/PAA_4 shrink by 22.2, 42.4 and 58.2%, respectively. The higher the pH of PEI, the greater the reduction in thickness due to glutaraldehyde’s reaction with the free primary amine groups. As the pH of PEI increases, so does the number of reactive, uncharged primary amine groups of PEI, leading to a tighter network and thinner resulting films.

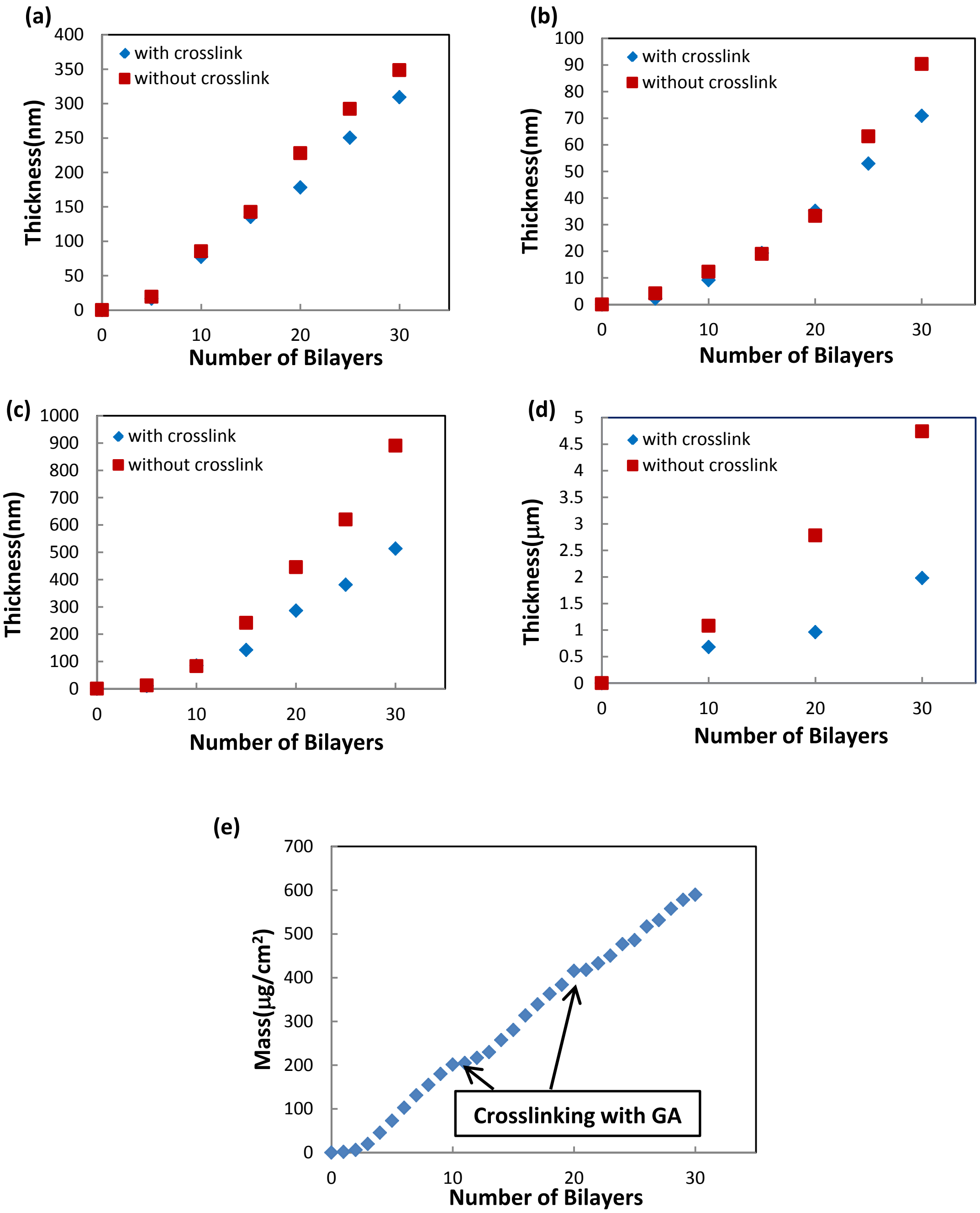

Figure 4.1. Film thickness as a function of bilayers deposited for LbL assemblies made with PEI_4/PAA_4 (a), PEI_7/PAA_7 (b), PEI_8/PAA_6 (c) and PEI_{10}/PAA_4 (d). (a),(b) and (c) were measured with ellipsometry, while (d) was measured with profilometry. Mass as function of deposited bilayers, for a 30 BL PEI_{10}/PAA_4 film (e), is shown to highlight the reset of film growth at 10 and 20 BL.[15]

Figure 4.1(e) shows the mass increase for every bilayer of $(PEI_{10}/PAA_4)_{30}$, with crosslinking at 10 and 20 BL. The two plateaus at 10 and 20 BL clearly demonstrate the inhibition effect of crosslinking that effectively "resets" the film growth. A similar inhibition effect, caused by creating a "blocking layer", has been observed by others.[193, 227] Crosslinking prevents interdiffusion of polymers into the underlying layers, which causes the growth to start over again (as though deposition were occurring on a bare substrate). This ability to reset the exponential growth process at a desired number of bilayers is another tool for tailoring LbL film thickness and properties.

4.3.2 Influence of Crosslinking on Film Thickness

Growth of PEI_{10}/PAA_4 assemblies, from 3 to 10BL, is shown in Figure 4.2(a). This system exhibits exponential growth typical of weak polyelectrolytes, similar to the well-studied PAH/PAA system.[56, 228-231] Exponential growth is attributed to an "in and out" diffusion mechanism that involves an endothermic polycation/polyanion complexation process.[190, 195, 219] Three different growth zones can be observed here: (1) island, (2) exponential and (3) linear. In the first few bilayers of deposition, polymers only cover part of the substrate surface, which results in relatively uneven surface coverage (known as islands) and slow growth (1~4BL). After several layers are deposited, the surface of the substrate becomes fully-covered, as islands coalesce with one another. In this stage, the "in and out" diffusion mechanism dominates the growth, resulting in the fastest growth (4~8BL). Eventually film growth slows and ultimately grows linearly due to the amount of charged groups for overcompensation reaching a saturation point (i.e., maximum value) (> 8BL).[228]

Chemical crosslinking of PEI_{10}/PAA_4 significantly alters the film thickness, as shown in Figure 4.2(a). 10BL PEI/PAA films were crosslinked with aqueous solutions of glutaraldehyde and 1-[3-(dimethylamino)propyl]-3-ethylcarbodiimide methiodide, using three concentrations (0.01M, 0.05M and 0.1M) and three residence times (3, 30 and 300 minutes). For GA, films became thicker with increasing concentration at a given crosslinking time (Fig. 4.2(b)). At a given concentration, the trend was not as clear. At 0.01M GA, thickness increased with increasing time, but at higher concentrations film thickness increased from 3 to 30 minutes and decreased from 30 to 300 minutes. This "peak" at 30 minutes is apparently related to the diffusion of GA molecules. When films were dipped into the GA solution, these molecules diffused into the PEI/PAA matrix and deposited onto energetically favorable reactive sites. Excess GA molecules presumably diffused out from the film and were rinsed away by DI water. With longer crosslinking time, the GA molecules were able to diffuse more deeply into the film, which also required a longer time for molecules to diffuse out. The larger film thickness for 30-minute crosslinking could be attributed to trapped molecules that did not have enough time to leave the polymer matrix. In the case of films crosslinked for 300 minutes, there is enough time for molecules to leave the matrix, which resulted in a smaller thickness. The lowest concentration of GA (0.01M), did not show this peak effect due to the low concentration allowing GA molecules diffuse in and out more quickly.

EDC crosslinking shows similar trends to GA, as shown in Figure 4.2(c). At the same crosslinking time, all films were thicker as EDC concentration increased. With 0.05 and 0.10M EDC, the largest thicknesses were observed with 30 minutes of crosslinking. In the case of 0.01M EDC, thickness increased with time up to 300 minutes. In higher concentration EDC solutions, there are more EDC molecules that can diffuse into the matrix and more time is needed for them to diffuse out. Lower concentration EDC, on the other hand, has fewer molecules in solution, which reduces diffusion time, much like with GA. The generally larger EDC-crosslinked film thickness, relative to GA, is likely due to larger molecular size (see Figure 4.3 for chemical structures). FTIR analysis of crosslinked films, decribed in the next section, provides more insight about the various reactions that occur in these systems.

Thermal crosslinking results in completely different trends than GA and EDC, as shown in Figure 4.2(d). PEI/PAA assemblies were thermally-crosslinked at 120, 150 and 180 °C for 1, 2 and 5 hours. 120°C crosslinked films, regardless of heating time, show very little change in thickness (ranging from 1.04 to 1.11 μm). At 150°C and 180°C, film thickness decreased as heating time increased (when compared to an unheated control). The fact that film thickness decreased 11% with 150°C and 20% with 180°C (after 5 hours of heating), while 120°C resulted in an 8% increase, suggests that this temperature is too low to induce significant crosslinking. Decreasing thickness at the higher temperatures is due to covalent bonds forming between acid and amine groups that pull the polymer chains closer to each other, as shown schematically in Figure 4.3(c).

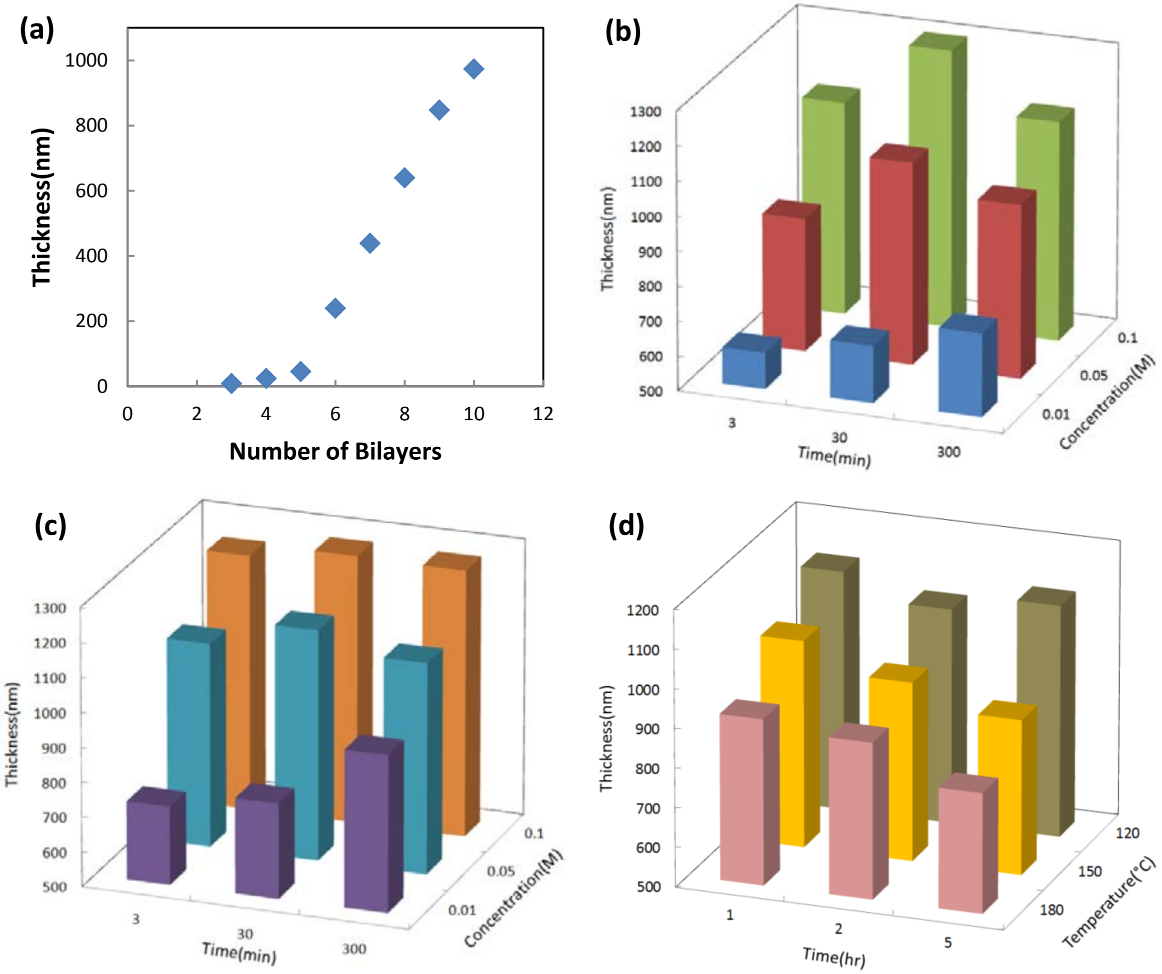

Figure 4.2. Ellipsometric thickness of PEI_{10}/PAA_4 assemblies as a function of bilayers deposited (a). The influence of GA (b), EDC (c) and heat (d) crosslinking on $(PEI_{10}/PAA_4)_{10}$ thickness is shown as a function of time, temperature and/or concentration.

4.3.3 FTIR Analysis of Crosslinked Films

Figure 4.3 shows the chemical reaction that occurs with each type of crosslinking. Glutaraldehyde reacts with the primary amine groups of PEI, forming a “Schiff base” (Fig. 4.3(a)), while EDC and heat create amide bonds between PEI and PAA. EDC acts as an activator in the process, generating a urea derivative as a side product (Fig. 4.3(b)).[220] Thermal crosslinking is a simple condensation reaction between

PEI and PAA that generates water as a byproduct (Fig. 4.3(c)). Each of these crosslinking mechanisms were verified by FTIR.

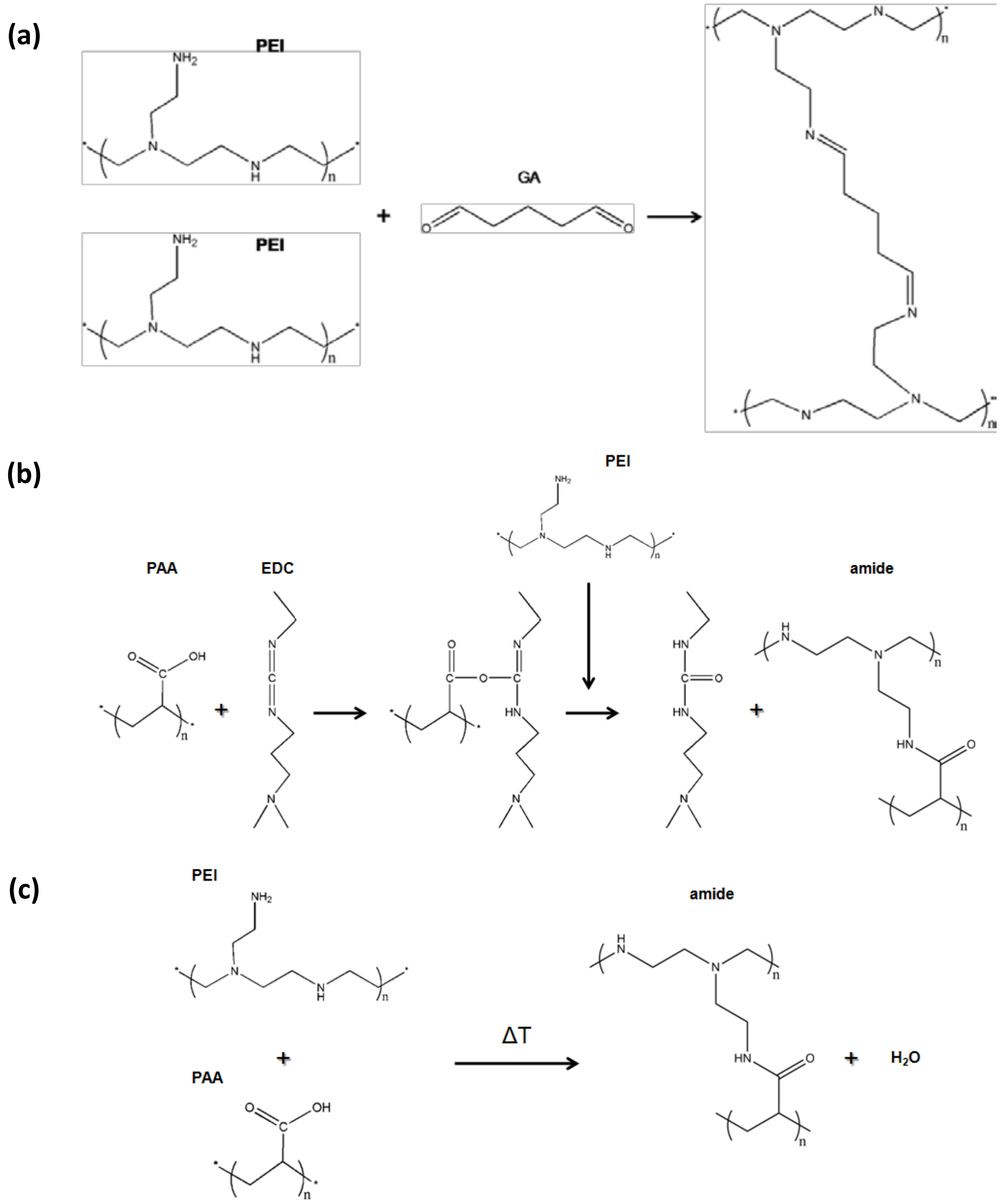

Figure 4.3. Chemistry of crosslinking for PEI/PAA assemblies exposed to GA (a), EDC (b) or heat (c).

Figure 4.4 shows the ATR-FTIR spectra of 10BL PEI_{10}/PAA_4 films crosslinked with varying GA concentrations and times. Assemblies crosslinked with 0.01M GA exhibited similar spectra, without generating new peaks (or shifted peaks), regardless of time (Fig. 4.4(a)). Increasing the GA concentration to 0.05M caused the peak at 1630 cm^{-1} ($–NH_2$, stretching) to diminish (Fig. 4.4(b)). The C=N stretching band is located from 1645-1665 cm^{-1},[232] so it is assumed that generating the Schiff base influenced the appearance of the adjacent peak. It should be noted that the intensity for Schiff bases is relatively low, so the peak is not clear in these spectra. This “smoothing out” effect is much clearer in films crosslinked with 0.10M GA, which indicates that higher concentration results in more crosslinking (Fig. 4.4(c)). These results confirm the proposed crosslinking mechanism (Fig. 4.4(a)) and suggest that the higher concentration solutions provide greater film crosslinking at a given time, which has also been observed by others.[233, 234]

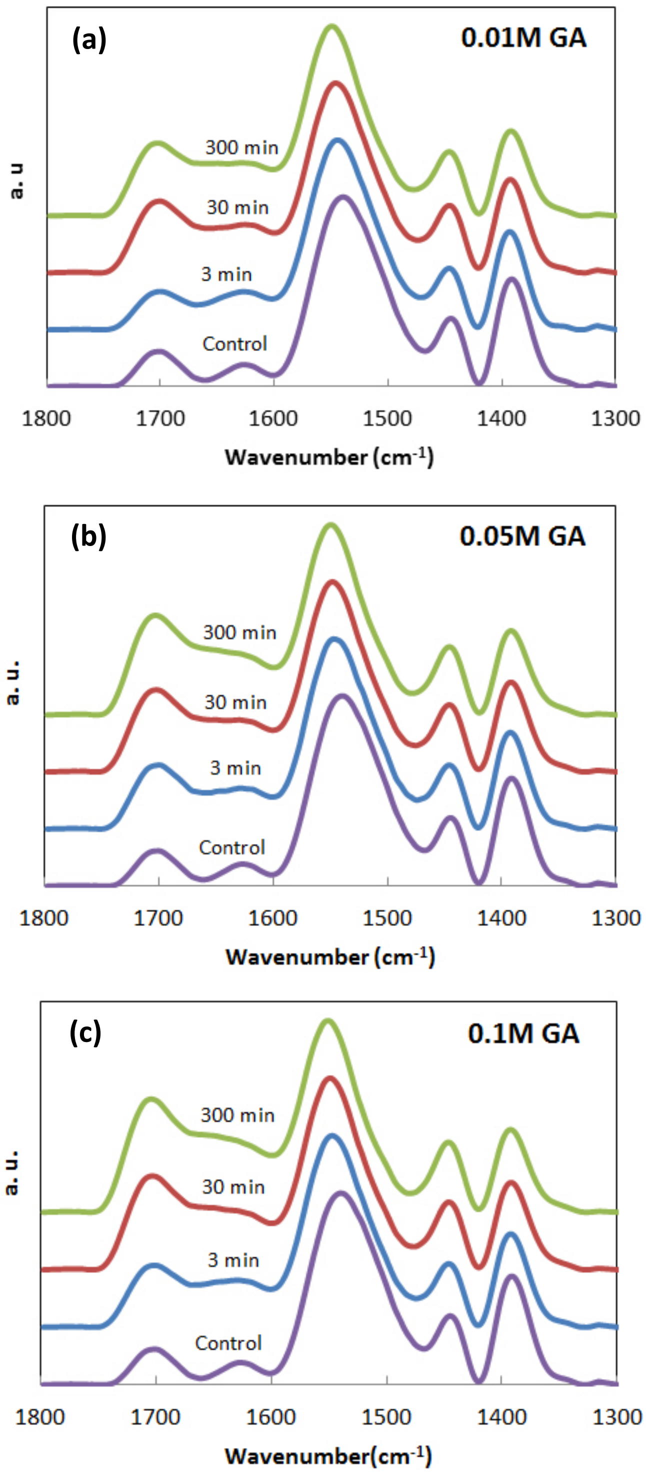

Figure 4.4. FTIR spectra of $(PEI_{10}/PAA_4)_{10}$ films crosslinked for varying times and with varying concentration of glutaraldehyde: 1300 to 1800 cm^{-1} (a-c). These spectra are intentionally overlaid with arbitrary offset for clarity.

The FTIR spectra of EDC crosslinked films are shown in Figure 4.5. All films crosslinked with EDC showed weaker intensity for the –COOH vibration band (located at 1710 cm^{-1}) because the carboxylic acid groups were activated by EDC to form amide bonds with PEI (Fig. 4.5(a)). The peak near 1630 cm^{-1} represents the C=O stretching band for the amide bond (amide I). From 0.01 to 0.1 M, this peak becomes more intensed with increasing crosslinking time, which can be explained by the generation of amide bonds with EDC. The –COOH vibration band gradually smooths out with increasing crosslinking time from 30 min to 300 min at all EDC concentrations. Additionally, the amide I peak intensity increased significantly, regardless of crosslinking time. A new peak generated at 1490 cm^{-1} can be observed at 300 min crosslinks for all EDC concentrations, which represents the $–O–CH_2$ band from the ester intermediate composed of PAA and EDC (Fig. 4.3(b)).

Thermally crosslinking PEI_{10}/PAA_4 assemblies requires a minimum temperature of 150°C for 5 hours. At 120°C there are no spectral changes relative to the control, regardless of heating time (Fig. 4.5(b)). Raising the temperature to 150°C produces similar results at 1 and 2 hours, but the amide I peak intensifies, and –COOH peak becomes weaker than the control, at 5 hours (Fig. 4.5(d)). These spectral changes indicate that some crosslinking has occurred. At 180°C, the intensity of the amide I peak becomes even more pronounced. All crosslinking times show intensified amide I peaks, while the intensity of peaks around 1543 cm^{-1} (the asymmetric stretching band for $–COO^-$) decreased. There is likely some overlap of this peak with the amide II band (40~60% N-H bending and 18~40% C-N stretching).[235] Among all the 180°C films, a decreasing trend is revealed between the apparent crosslink density, as evidenced by the intensity of the amide I band (~1543 cm^{-1}), and the heating time in these PEI/PAA films (Fig. 4.5(f)).

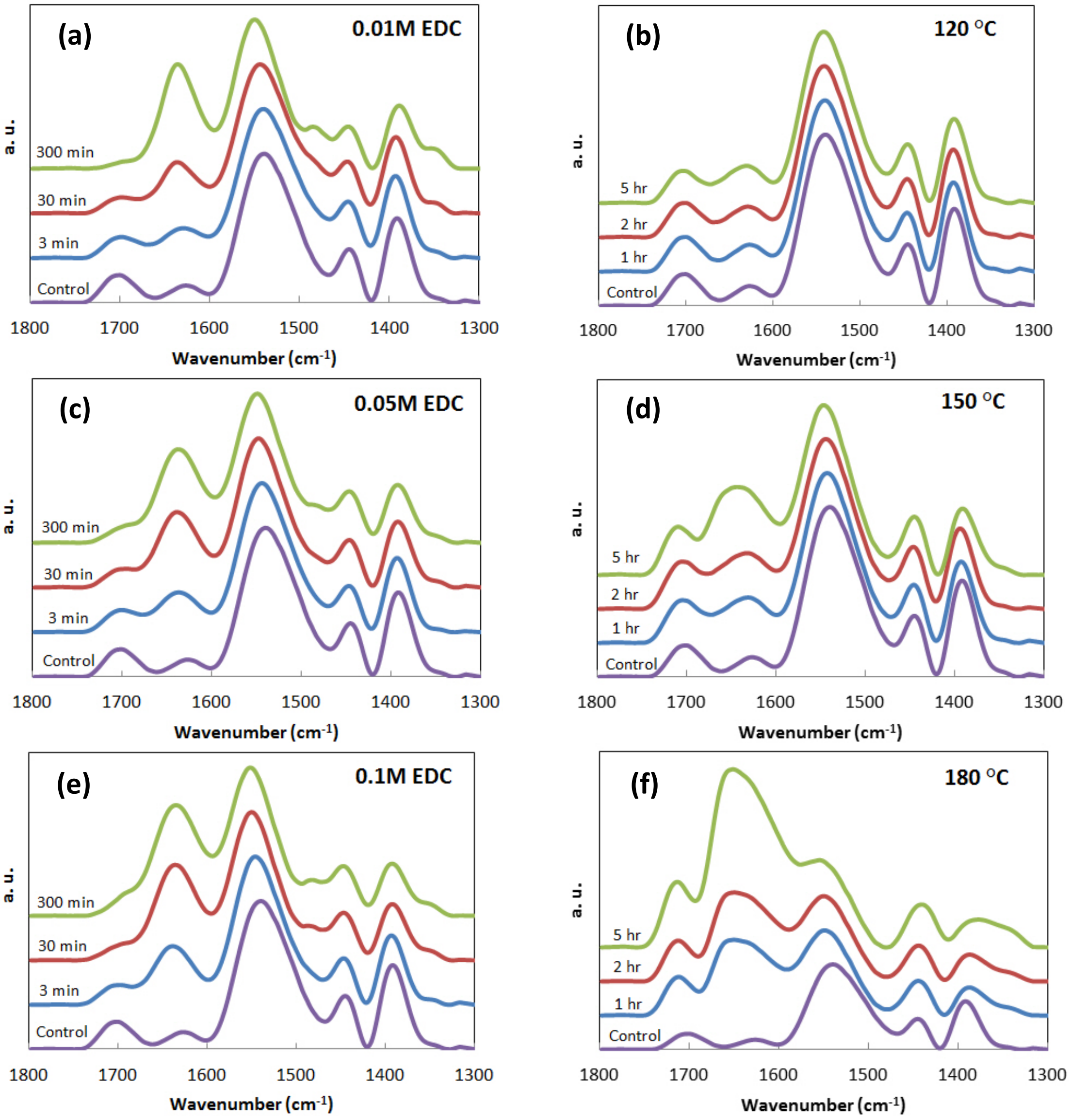

Figure 4.5. FTIR spectra of $(PEI_{10}/PAA_4)_{10}$ films crosslinked for varying times and with varying concentration of EDC (a), (c), (e) and heating at varying temperatures and times (b), (d) (f). These spectra are intentionally overlaid with arbitrary offset for clarity.

4.3.4 Topography of Crosslinked Films

AFM surface images of $(PEI_{10}/PAA_4)_{10}$ films, with and without 0.1M GA, 0.1M EDC or 150°C exposure, are shown in Figure 4.6. All films were crosslinked for 30 minutes for direct comparison. The GA-crosslinked film has a rougher surface than the control (Fig. 4.6(b) and (f)), while both EDC and thermally crosslinked films have smoother surfaces than the control (Fig. 4.6(c), (d), (g) and (h)). GA crosslinking creates covalent bonds between PEI layers by generating a Schiff base (Fig. 4.3(a)), which tightens the initial molecular arrangement. EDC and thermal crosslinking, on the other hand, create covalent linkages by connecting amine groups from PEI and carboxylic acid groups from PAA, which fill the uneven “free sites” and make the overall surface smoother. Root-mean-square (RMS) surface roughnesses were measured with 20 × 20 μm scans. The order of RMS roughness is: GA (118.1 nm) > control (90.5 nm) > thermal (58.1 nm) > EDC (55.4 nm). After crosslinking, GA increased roughness by 30%, while thermal and EDC reduced roughness by 35% and 38%, respectively. A similar smoothing effect by EDC, on PAH/PAA assemblies, was previously demonstrated by Caruso.[220] Crosslinking provides a direct way to manipulate surface morphology of LbL films, which could be useful for surface patterning or tailoring hydrophilicity.

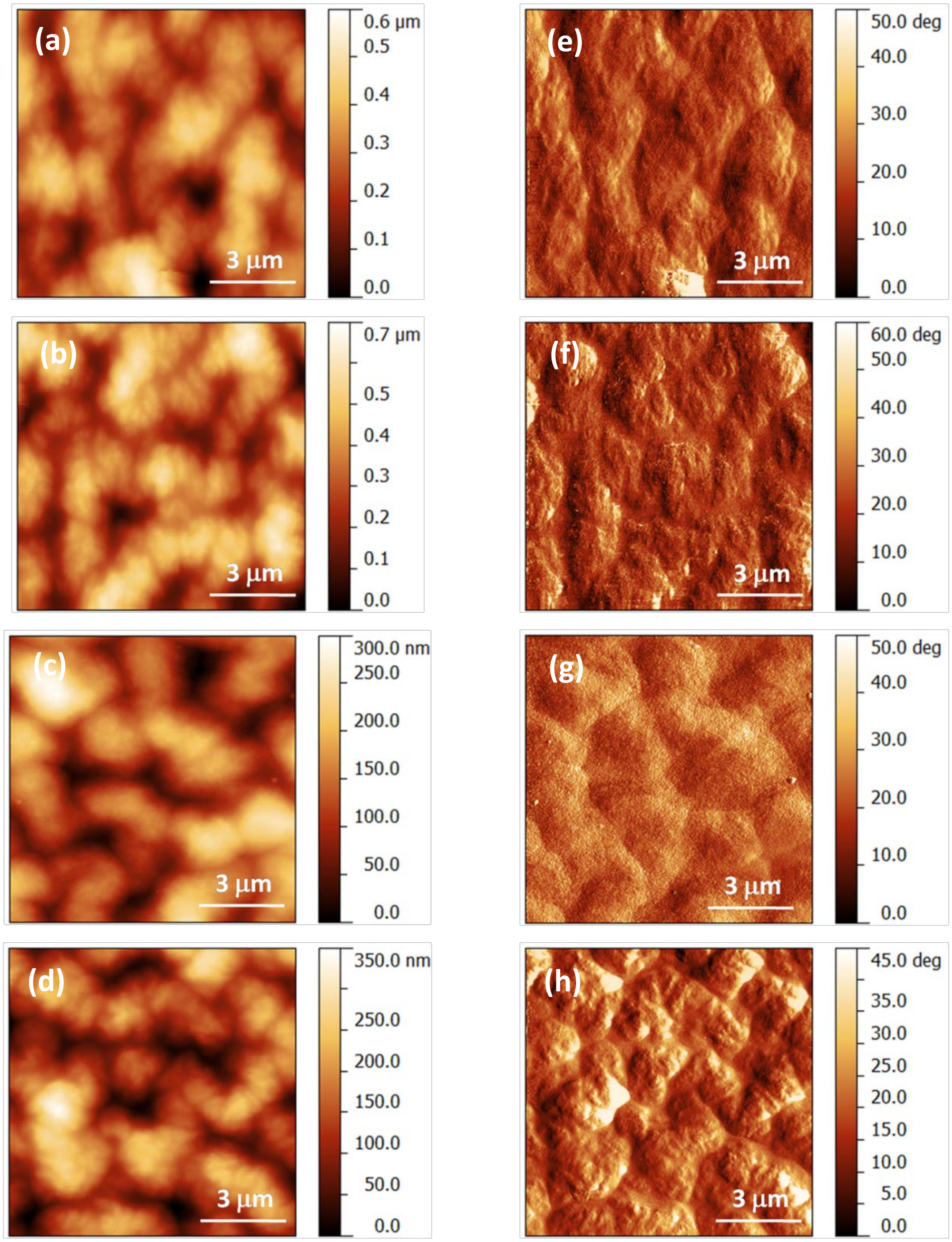

Figure 4.6. AFM surface images of $(PEI_{10}/PAA_4)_{10}$ films prepared with varying crosslinking conditions: control (a)(e), 0.1M GA (b)(f), 0.1M EDC (c)(g), 150°C (d)(h). (a)-(d) are height images and (e)-(h) are phase images. All crosslinking was performed for 30 minutes.

4.3.5 Oxygen and Moisture Barrier of Crosslinked Films

Oxygen transmission rates (OTR) of PEI_{10}/PAA_4 assemblies on PET were measured at 23 °C and 0% or 100% RH, as shown in Figure 4.7. $(PEI_{10}/PAA_4)_8$ films, crosslinked with varying concentrations (0.01, 0.05 and 0.10M) of GA for 30 minutes, show a three orders of magnitude reduction in OTR relative to the uncoated substrate (OTR = 8.48 $cc/m^2 \cdot day$ for 179 μm thick PET film) under dry conditions (Fig. 4.7(a)). An 8BL PEI_{10}/PAA_4 thin film with no crosslinking, and crosslinked with 0.10M GA, reaches the instrumental undetectable limit (OTR < 0.005 $cc/m^2 \cdot day$). It is interesting to see that intermediate GA concentrations resulted in increased OTR. Higher GA concentration correlates to higher extent of crosslinking in PEI_{10}/PAA_4 thin films (Fig. 4.4), so it is assumed that the observed reduction in barrier came from reduced film thickness and incomplete crosslinking (OTR is a thickness dependent property). Table 4.1 summarizes oxygen barrier and film thickness data for these chemically-crosslinked assemblies. With 0.01M GA, an 8BL assembly's thickness is reduced 30%, while it is only reduced 14% with 0.10M GA. At 100% RH, 0.01M and 0.05M GA both fail to reduce OTR relative to the uncrosslinked $(PEI_{10}/PAA_4)_8$ thin film, which correlates with the 0% RH results. The highest crosslink density, from 0.10M GA, reduces the OTR from 0.61 to 0.09 $cc/m^2 \cdot atm \cdot day$ (Fig. 4.7(b)), which is two orders of magnitude below uncoated PET. Although similar to GA, crosslinking with EDC results in some interesting differences in thin film OTR.

At 0% RH, the OTR of $(PEI_{10}/PAA_4)_8$ increased slightly from undetectable to 0.0062 $cc/m^2 \cdot day$ with 0.01M EDC, and became much higher with 0.05M (0.305 cc/m^2

· atm · day), while 0.10M EDC decreased the OTR back to 0.0062 cc/m^2 · atm · day (Fig. 4.7(c)). With a constant crosslinking time, the extent of reaction increased as the EDC concentration increased. It is clear from Table 4.1 that film thickness is less influence by EDC and the resulting lower density films exhibit poorer barrier than GA-crosslinked films. At 100% RH, the 0.01M EDC crosslinked film shows the most OTR improvement compared to the two higher concentrations (Fig. 4.7(d)). It is likely that the optimum crosslinking concentration for EDC is < 0.01M. With greater EDC concentration, more crosslinking generates more urea derivatives that may plasticize the film and reduce the oxygen barrier. Permeability values in Table 4.1 were obtained by multiplying film thickness by OTR. GA crosslinking yields reduced permeability with increasing concentration, while the most dilute EDC crosslinking exhibits the lowest oxygen permeability. Crosslinking with 0.10M GA also produces the best barrier at 100% RH. With an oxygen permeability of $< 5.9 \times 10^{-21}$ · cm^3 · cm/cm^2 · s · Pa under dry conditions, this nanocoating is better than 100 nm SiO$_x$ ($P_{O2} = 1.05 \times 10^{-20}$ · cm^3 · cm/cm^2 · s · Pa)[150] and may be more economical for commercial-scale coating of packaging film.

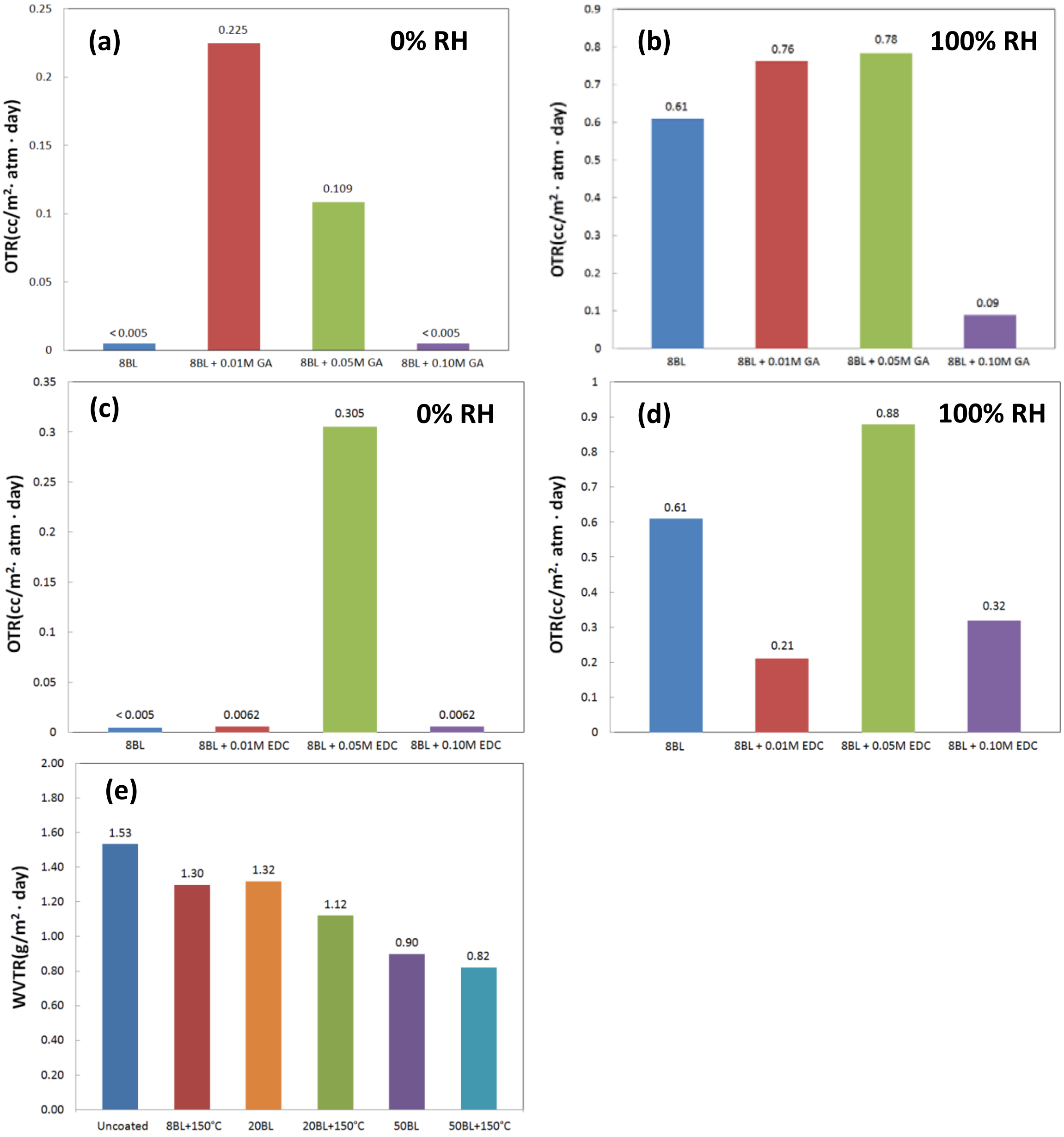

Figure 4.7. Oxygen transmission rate of PEI_{10}/PAA_4 assemblies on PET at 0% (a)(c) and 100% RH (b)(d). Water vapor transmission rate of PEI_{10}/PAA_4 films on PET (e). These films were crosslinked with GA (a)(b) or EDC (c)(d) for 30 minutes or heated (e) for 5 hours.

Table 4.1. Oxygen permeability of $(PEI_{10}/PAA_4)_8$ assemblies on PET film at 23°C.

Recipe	OTR (cc/m^2 · day · atm) 0% RH	 100% RH	Film Thickness (nm)	Permeability(×10^{-16} · cm^3 · cm/cm^2 · s · Pa) Film[a]	 Total
Bare PET	8.48	8.48	N/A	N/A	17.3
8BL	<0.005[b]	0.61	640	<0.000068[b]	<0.0096
8BL+0.01M GA	0.23	0.76	445	0.0023	0.46
8BL+0.05M GA	0.11	0.78	501	0.0013	0.22
8BL+0.10M GA	<0.005	0.09	551	<0.000059	<0.0096
8BL+0.01M EDC	0.0062	0.21	483	0.000068	0.013
8BL+0.05M EDC	0.31	0.88	526	0.0038	0.63
8BL+0.10M EDC	0.0062	0.32	603	0.000085	0.012

[a] Film permeability was decoupled from the total permeability using a previously described method.[146]

[b] The low end detection limit for an Ox Tran 2/21 L module is 0.005 cc/m^2 · day.

Thermally-crosslinked $(PEI_{10}/PAA_4)_8$ films (at 120 or 150°C for 5 hours) exhibited higher dry OTR (0.26 and 0.36 cc/m^2 · atm · day for 120 and 150°C, respectively) than an uncrosslinked film. Elevated OTR was also observed at 100% RH (0.90 and 1.22 cc/m^2 · atm · day for 120 and 150°C, respectively) relative to an unheated film (0.61 cc/m^2 · atm · day). Reduced thickness and a low level of crosslinking are the two factors causing higher OTR. Simple dehydration at 120 °C can account for reduced thickness (from 640 to 382 nm) without any crosslinking. Although heating at 150°C for

5 hours results in amide crosslinks (Fig. 4.5(d)), the significant decrease in thickness (from 640 to 507 nm) appears to counteract the benefit of crosslinking.

Gas transport through materials can be attributed to two mechanisms: (1) Fickian flow by a diffusion-solubility model, which is mostly observed in homogeneous polymeric materials or (2) flow through defects, such as pinholes or micro-channels.[128] PEI/PAA assemblies are believed to have defect-free surfaces, as shown in Figure 4.6. Oxygen transport through a PEI/PAA multilayer film is expected to be better described by the diffusion-solubility model based on this observation. This model describes molecular transport through a homogeneous material in several steps. Penetrants are first adsorbed onto the barrier surface, which then dissolve into the material. Gas molecules next diffuse through the thickness, moving out of one phase and re-dissolveing into another phase to continue the process. In a single-phase material, the permeability of Fickian flow depends on both diffusivity and solubility (Equation 2.5). With two components and numerous acid/base interfaces, the PEI/PAA thin film assembly is believed to have a scrambled-egg structure,[202] similar to a highly interpenetrated network.[203] The chaotic aggregation among carboxylic acid groups and amine groups makes it difficult for gas molecules to dissolve, diffuse and re-dissolve. Interactions with PEI, PAA, and the PEI/PAA interfaces all contribute to slowing molecular motion through the film. Unlike traditional macroscopic polymer blends, LbL assembly results in “nano-blends” of the two ingredients, with many more interfaces that trap gas molecules and create a high oxygen barrier.

Another contributing factor to the high oxygen barrier in these films is reduced free volume.[236] The high glass transition temperature for this PEI_{10}/PAA_4 assembly was previously used to show that PEI and PAA are more attracted to each other than they are to themselves.[15] This strong attraction reduces free volume that can be further reduced by crosslinking. Covalent crosslinking not only reduces the free volume of PEI/PAA, it also provides a better humid oxygen barrier by reducing swellability. In a high humidity environment, LbL films often swell and lose integrity,[200, 201] which increases permeability to oxygen molecules passing through. Crosslinking the “free” functional groups ($-NH_2$ of PEI and -COOH of PAA) in the present assemblies decreases the number of hydrophilic groups within the film, thereby making it more hydrophobic. Crosslinking also reduces the ability of the film to swell, which was expected to improve water barrier in these systems.

Water vapor transmission rates (WVTR) were tested on 8BL films crosslinked with GA, EDC or heat at varying concentrations and temperatures. Unlike with oxygen, WVTR values show only 16 ~ 20 % improvement (1.23~1.30 $g/m^2 \cdot day$) relative to the uncoated substrate (1.53 $g/m^2 \cdot day$). Heated assemblies were chosen for further WVTR testing because water is driven out during crosslinking. Figure 4.7(e) shows WVTR as a function of the number of PEI_{10}/PAA_4 bilayers deposited on PET, with and without exposure to 150 °C for 5 hours. Water vapor transmission rate decreased with increasing bilayers. For 20BL (3.3 μm) and 50BL (7.3 μm) films, the WVTR decreased 15% and 9% compared to their uncrosslinked counterparts, respectively. A crosslinked 8BL film is very similar to the 20BL film without heat treatment, which demonstrates that thermal crosslinking creates a more moisture-resistant structure. The lowest WVTR came from the 50BL heated film, which decreased the WVTR of PET from 1.53 to 0.82 $g/m^2 \cdot day$ (~46% reduction). In general, thickness and structure are both important for reducing WVTR. Although heating decreases the number of permeable pathways in the structure by creating amide bonds, the simultaneous reduction of thickness counteracts this to some extent. The electrostatic attraction among PEI/PAA charged groups can also be dissociated by water, creating more diffusion pathways.

4.4 Conclusions

Super gas barrier thin films, composed of PEI and PAA, were successfully deposited via LbL assembly and crosslinked using glutaraldyhyde, 1-[3-(dimethylamino)propyl]-3-ethylcarbodiimide methiodide and/or heating with varying concentration, temperature and time. Thicknesses of chemically-crosslinked films exhibit a "peak effect" that is attributed to lack of diffusion time that causes some swelling. Films crosslinked with lower concentration (< 0.05M) and longer time (> 3min) are thicker. Thermally-crosslinked films exhibit reduced thickness with longer crosslinking time at or above 150 °C. Covalent bond formation, due to the various crosslinking mechanisms, was confirmed by FTIR. All IR spectra indicate higher crosslinking density with longer crosslinking time. AFM images highlight the ability to tailor the surface roughness of these PEI/PAA films with crosslinking method. GA makes the surface rougher, while EDC and thermal crosslinking both make film smoother.

Oxygen transmission rates of chemically-crosslinked PEI_{10}/PAA_4 assemblies are improved at 100% RH relative to uncrosslinked films. Maximum barrier improvements occur at different GA and EDC concentrations, suggesting that crosslinker chemistry influences barrier. A 551 nm thick, 8BL PEI/PAA assembly exhibits an oxygen permeability ($< 5.9 \times 10^{-21}$ $cm^3 \cdot cm/cm^2 \cdot s \cdot Pa$) that rivals SiO_x. Thermally-crosslinked films showed some improvement in moisture barrier, but this required a high number of layers. This marks the first systematic study of crosslinking and its influence on the barrier properties of LbL assemblies. These films are inherently hydrophilic and more work needs to be done with hydrophobic crosslinkers and/or addition of impermeable particles to make significant reductions in WVTR. The improved oxygen barrier under high humidity, and modest improvement in water vapor barrier, is promising for food packaging, selective gas membranes and protection of flexible electronics.

CHAPTER V

SUPER GAS BARRIER OF GRAPHENE-POLYMER MULTILAYER THIN FILMS

5.1 Introduction

Graphene, a single atomic sheet of graphite, has quickly become one of the most studied nanomaterials since its isolation in 2004.[237] The tremendous interest in graphene lies in its one-atom-thick structure, with a densely packed honeycomb crystal lattice, which is capable of exhibiting unprecedented electrical conductivity,[105, 238] thermal conductivity,[239] and mechanical properties.[240, 241] High surface to volume ratio makes this material difficult to work with due to the strong van der Waals attraction between single layer graphene sheets, so most of the graphene-related work uses chemically or thermally modified graphene.[242-244] Graphene oxide (GO), obtained from exfoliation of graphite oxide, is widely used to create graphene sheets by chemical reduction.[245-247] Unlike graphene, GO can be stabilized in aqueous solution without the need for chemical stabilizers.[246] There is some debate surrounding the structure of GO, but the Lerf-Klinowski model, shown in Figure 5.1, is currently the most accepted one (i.e., unoxidized aromatic regions containing benzene rings, epoxide and hydroxyl groups, alongside oxidized regions with aliphatic six-membered rings).[248, 249] Parts of the edges of GO sheets have carboxylic acid groups that impart negative charges when exfoliated in water. These negatively-charged, high aspect ratio (l/d ~ 1000) nanoplatelets are known to be impermeable to most gases,[187] much like clay, making them of great interest for the preparation of gas barrier nanocomposites.

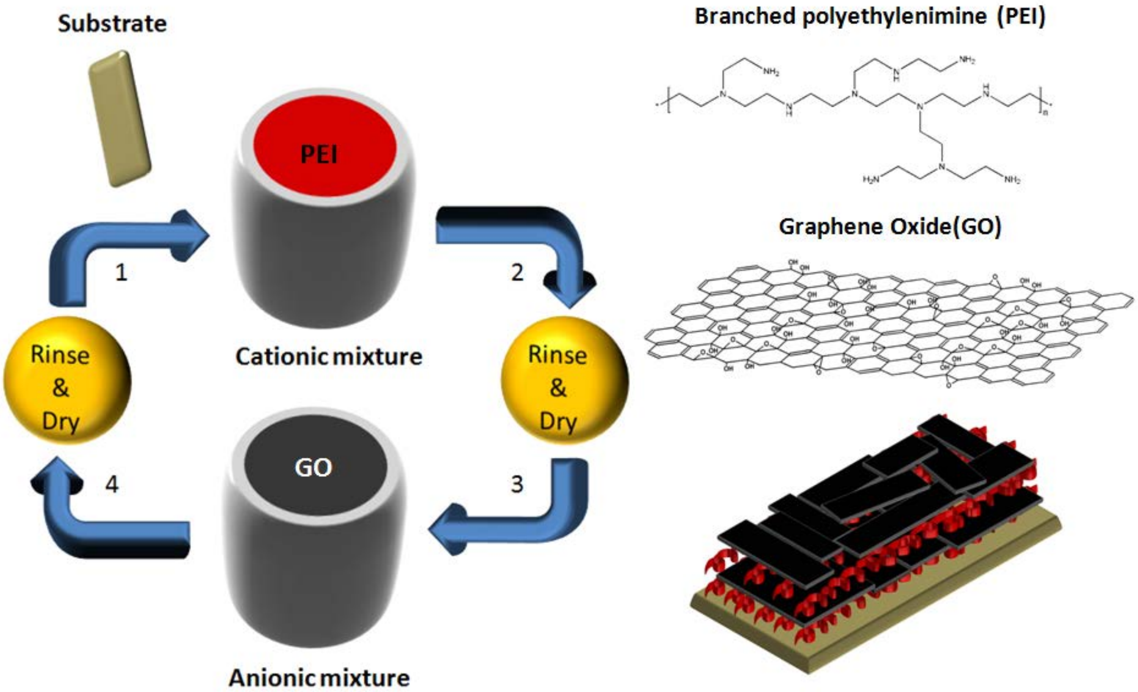

Figure 5.1. Schematic of layer-by-layer deposition of grapheme oxide and polyethylenimine. Steps 1-4 are repeated until the desired number of bilayers are achieved. The structure of GO was adapted from ref 245.

Thin films capable of preventing gas or water molecules from permeating through a polymer film remain a major challenge for food and flexible electronics packaging.[250-252] Reactive gases (e.g. O_2) and moisture cause food to perish, create electrical ‘”shorts” in microelectronics, and reduce the life span of electrodes. Metalized films,[127, 253] SiO_x coatings[146, 149] and nanoplatelet-filled polymer composites[114, 254, 255] have all been studied to circumvent these problems. Inorganic thin films have excellent intrinsic barrier behavior, but they tend to suffer from pinholes or defects generated by bending or stretching.[256, 257] Polymer composites have better mechanical properties, but nanoparticle aggregation reduces barrier and transparency.[258-260]

Layer-by-layer (LbL) assembly offers the opportunity to alternately deposit polymer and nanoparticles onto a substrate as nanometer thick layers via electrostatic attraction or hydrogen bonding.[12, 13] This precisely controlled deposition of ingredients has already been used to generate super gas barrier thin films.[8, 15, 129, 207] Tailoring aqueous deposition mixture concentration,[49] temperature,[261] pH[52] and exposure time,[188] allows LbL film properties like thickness, transparency, and gas permeability to be precisely controlled. Although never before studied for gas barrier, graphene has been deposited in LbL assemblies for solar cells,[262] energy storage[21] and selective gas sensing.[32]

In the present work, single layers of graphene oxide are alternately deposited with brached polyethylenimine (PEI) to investigate the oxygen barrier of these thin film assemblies. Thickness and mass exhibit linear growth at a rate of 4.3 ~ 5.0 nm per PEI/GO bilayer (with 88 ~ 91 wt% GO loading in the deposited films). Atomic force microscopy (AFM) shows discrete single layer graphene sheets on the surface and cross-sectional transmission electron microscopy (TEM) images show the well-separated graphene sheets inside of the polymer matrix, suggesting a perfectly oriented nanobrick wall structure. A 10 bilayer film deposited on PET, made with 0.1 wt% PEI and 0.2 wt% GO mixtures, is only 91 nm thick and has an oxygen transmission rate (OTR) of 0.12 cc m^{-2} day^{-1} (or an oxygen permeability 2.5×10^{-20} cm^3 cm cm^{-2} s^{-1} Pa^{-1}), which is comparable to a 100 nm SiO_x nanocoating[150] and two orders of magnitude better than a

25 μm EVOH copolymer film.[263] This study marks the first graphene-based gas barrier coating prepared using layer-by-layer assembly and the lowest oxygen permeability obtained by any graphene-based composite. With the ability to combine gas barrier with electrical conductivity of graphene though reduction of graphene oxide,[264] these films could be promising for flexible electronics.

5.2 Experimental

5.2.1 Preparation of Deposition Mixtures

Single layer graphene oxide (GO) (CheapTubes, Brattleboro, VT) was exfoliated in DI water by 10W ultrasonication for 10 minutes with a MISONIX XL-2000 tip sonicator (Qsonica, Melville, New York). Anionic GO suspensions of 0.01, 0.05 and 0.2 wt% were prepared by sonicating 100 ml volumes. In order to prevent depletion, GO suspensions were replaced after every ten bilayers of deposition. All other materials are identical to those described in Chapter III (Section 3.2.1).

5.2.2 Substrates

All substrates are identical to those described in Chapter III (Section 3.2.2).

5.2.3 Layer-by-layer Film Deposition

The deposition process is identical to that described in Chapter III (Section 3.2.3).

5.2.4 Thin Film Characterization

Film thickness on silicon wafers was measured with an alpha-SE Ellipsometer (J. A. Woollam Co., Inc., Lincoln, NE). All other characterization techniques are the same as Chapter III (Section 3.2.4).

5.3 Results and Discussion

5.3.1 Film Growth of PEI/GO

The layer-by-layer deposition process for PEI/GO is shown schematically in Figure 5.1. LbL films are abbreviated as $(PEI/GO_x)_y$, where x is the concentration of GO deposition suspension and y is the number of bilayers deposited. In all cases, the aqueous PEI solution was 0.1 wt%. The growth of $PEI/GO_{0.01}$ and $PEI/GO_{0.05}$ assemblies are shown in Figure 5.2. Each film grows linearly with increasing number of bilayers deposited (Fig. 5.2(a)). The average thickness of $PEI/GO_{0.05}$ is 17% greater than $PEI/GO_{0.01}$ (4.3 nm and 5.0 nm per bilayer for $PEI/GO_{0.01}$ and $PEI/GO_{0.05}$, respectively). Higher concentration GO suspension results in more platelets deposited, which in turn attracts more PEI to achieve charge overcompensation. Greater platelet deposition is also believed to cause more stacking of GO platelets (mostly two or three platelets per stack). Mass growth measured by QCM is similar to thickness growth, exhibiting linear trends for both GO concentrations (Fig. 5.2(b)). The total mass of $(PEI/GO_{0.05})_{20}$ is 31% heavier than $(PEI/GO_{0.01})_{20}$. $(PEI/GO_{0.01})_{20}$ has 88 wt% GO, while $(PEI/GO_{0.05})_{20}$ has 91 wt% GO, suggesting some modest stacking of platelets at higher concentration. With knowledge of both film mass and thickness, density of $(PEI/GO_{0.01})_{20}$ is calculated to be

~ 1.94 g/cm^3 [$(PEI/GO_{0.05})_{20}$ density is ~ 2.00 g cm^{-3}]. These values are close to theoretical densities calculated using the known density of PEI (~1) and graphite (~2.2). Only LbL deposition can produce truly dense nanocomposites with such a high platelet loading.

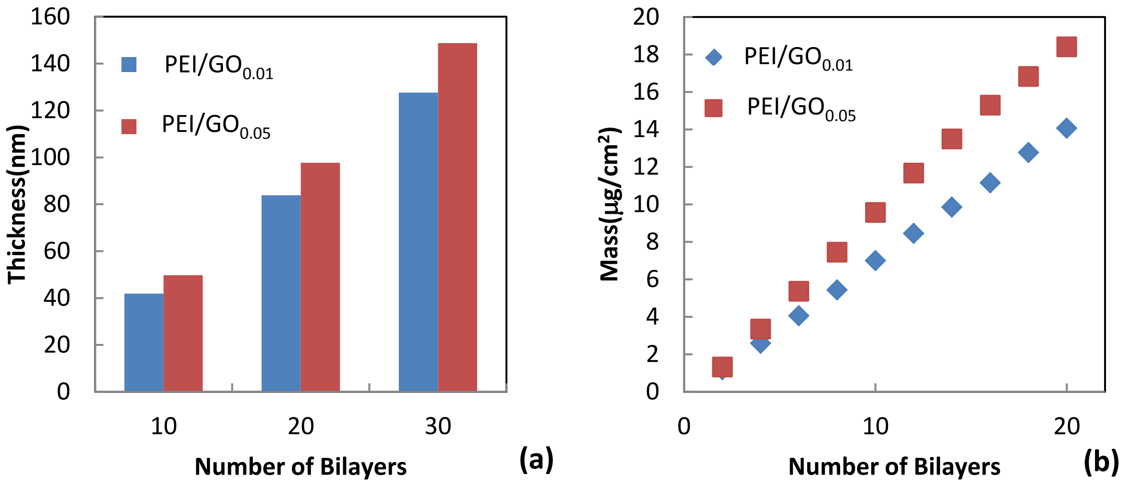

Figure 5.2. Film thickness (a) and mass (b) as a function of bilayers deposited for PEI/GO assemblies. The subscript on GO indicates the suspension concentration used (0.01 or 0.05 wt%).

5.3.2 Film Morphology of PEI/GO

This high graphene oxide loading, and near perfect orientation of platelets, is shown in TEM cross-sectional images of $(PEI/GO_{0.01})_{30}$ (Fig. 5.3(a)) and $(PEI/GO_{0.05})_{30}$ (Fig. 5.3(b)). The dark lines in these images are the GO sheets. These oriented graphene oxide sheets are separated by lighter-colored PEI nanolayers to form a nanobrick wall structure similar to previously reported PEI and montmorillonite clay assemblies.[8] The waviness in these images is due to stress relief during microtome sectioning of the film.

Surface topographies of PEI/GO$_{0.01}$ (Fig. 5.3(c)) and PEI/GO$_{0.05}$ (Fig. 5.3(d)) single bilayer films were imaged by AFM. Platelet structures can be seen at both concentrations. These images suggest single GO platelets are very poly-dispersed, with diameters between 0.2 and 3.0 μm. It also appears that both concentrations deposit mostly exfoliated single platelets, which is the result of the electrostatic repulsion among negatively-charged GO platelets. This combination of high loading of impermeable nanoplatelets, and orientation of these platelets with their largest dimension parallel to the substrate, is a recipe for excellent oxygen barrier.

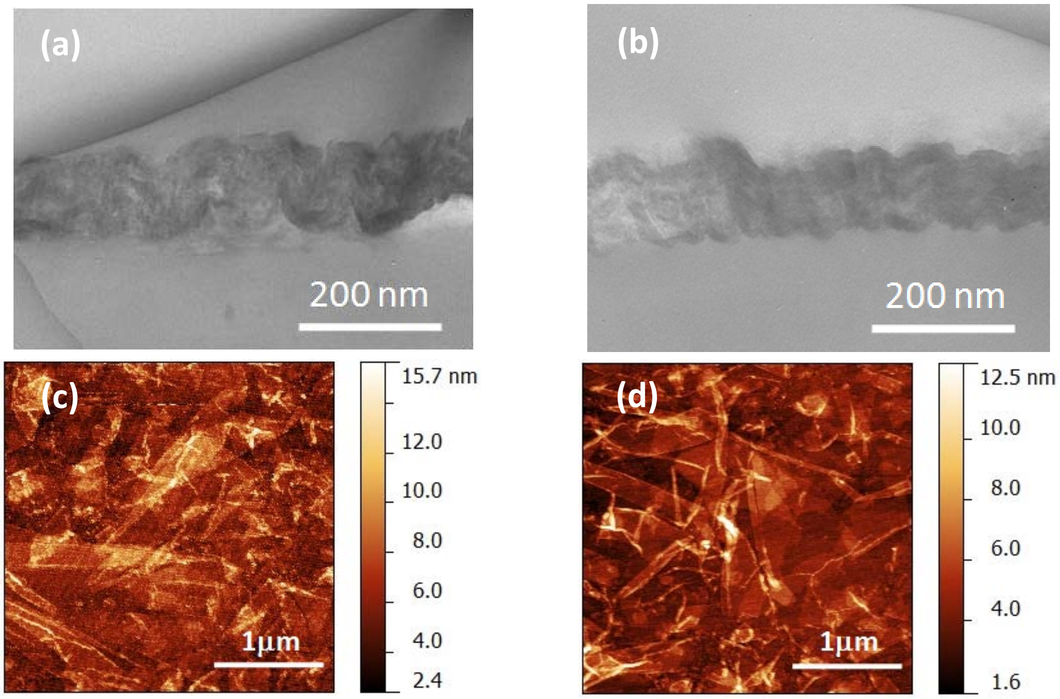

Figure 5.3.TEM cross-sectional images of (PEI/GO)$_{30}$ on PS using 0.01wt% (a) and 0.05wt% (b) GO deposition suspensions. The double arrow bars highlight the thickness of the films. AFM surface images of (PEI/GO)$_{1}$, on Si wafers, made with 0.01 (c) or 0.05wt% (d) GO deposition suspensions.

5.3.3 Oxygen Barrier of PEI/GO

Oxygen transmission rates (OTR) of PEI/GO films deposited on a 179 μm PET substrate were measured at 23 °C and 0% (or 100%) RH, as shown in Figure 5.4. At 0% RH, OTR decreases with increasing the number of bilayers deposited. For $(PEI/GO_{0.01})_{10}$, OTR of the uncoated PET drops from 8.48 to 1.23 cc/m^2 · day. Increasing the number of bilayers to 20 and 30 further decreases the OTR to 0.46 and 0.27 cc/m^2 · day, respectively (Fig. 5.4(a)). $PEI/GO_{0.05}$ exhibits the same decreasing OTR trend as $PEI/GO_{0.01}$, but with lower values at the same number of bilayers that indicates better lateral platelet packing. The $(PEI/GO_{0.05})_{30}$ film reduces the OTR by a factor of 45 relative to the uncoated PET substrate (Fig. 5.4(b)). Concentration of GO in the aqueous deposition suspension is more pronounced at 10BL, while the OTR reduction from 10 to 20BL (and 20 to 30BL) for each concentration is relatively similar. At 100% RH, the OTR of $PEI/GO_{0.05}$ assemblies increased relative to the same number of bilayers at 0% RH (Fig. 5.4(c)). This reduced barrier was less than a factor of two and much less significant than what has been observed in clay-polymer assemblies.[129, 265] OTR of 10BL films with 0.01, 0.05 and 0.2 wt% GO are shown in Figure 5.4(d). A $(PEI/GO_{0.2})_{10}$ has an OTR of 0.12 cc/m^2 · day, which is lower than $(PEI/GO_{0.05})_{30}$ and a factor of 71 lower than uncoated PET. Similar to clay,[50] increasing the GO concentration in suspension also increases the GO concentration inside of the LbL films, which results in more overlapping platelets and limits the diffusion pathway for oxygen molecules. The OTR of $(PEI/GO_{0.05})_{20}$ is better than $(PEI/MMT_{0.05})_{20}$ by a factor of 20 due to a much larger aspect ratio (α_{MMT} ~ 200 and α_{GO} ~ 1000).[50]

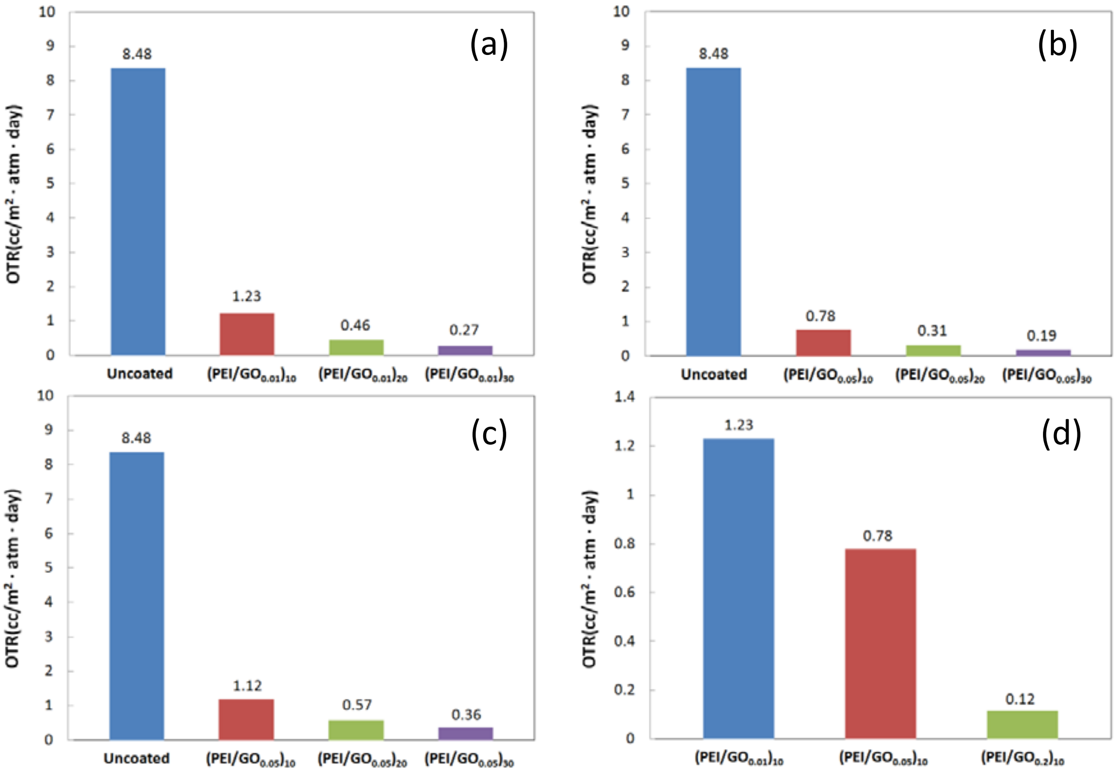

Figure 5.4. Oxygen transmission rate of PEI/GO assemblies on PET at 23°C and 0% RH made with 0.01 (a) or 0.05 wt% GO (b) suspensions. OTR of films made with 0.05 wt% GO suspensions at 23°C and 100% RH (c). OTR of 10BL PEI/GO made with varying GO concentrations (d).

Table 5.1 summarizes thickness and barrier properties of these PEI/GO assemblies. All PEI/GO thin films have oxygen permeability around $10^{-19} \sim 10^{-20}$ $cm^3 \cdot cm/cm^2 \cdot s \cdot Pa$. $(PEI/GO_{0.2})_{10}$, with a thickness of 91 nm, has an oxygen permeability of 2.5×10^{-20} $cm^3 \cdot cm/cm^2 \cdot s \cdot Pa$, which is within the same order of magnitude as a typical SiO_x nanocoating[150] and two orders of magnitude better than a 25 μm EVOH copolymer film.[263] This is also the lowest oxygen permeability ever reported for any graphene-based material.[266-268] This tremendous barrier comes from an extremely "tortuous pathway" best decribed by Cussler.[86] Polymer composites with impermeable platelets generate a brick wall structure with multiple parallel channels inside of the matrix. When gas molecules travel perpendicularly through the film, they tend to wiggle through the permeable polymer channels until they find a slit in the platelet layer to penetrate into the next channel. A description of Cussler's model, as it pertains to these polymer-platelet assemblies, and schematic of this structure has been reported previously.[8, 50, 107] One can argue that a perfectly aligned nanobrick wall structure is achieved by using layer-by-layer assembly, with PEI as mortar and GO platelets as nanobricks. This unique structure, creates a longer diffusion length than composites made by simple mixing. Moreover, the hydroxyl groups along the edge of graphene oxide (Fig. 5.1) also contribute to some hydrogen bonding with permeating oxygen molecules, further contributing to reduced oxygen permeability. The oxygen permeability of $(PEI/GO_{0.2})_{10}$ is five orders of magnitude lower than a PVA/GO composite and eight orders of magnitude lower than a PS/GO composite prepared by simple mixing.[266, 267]

Table 5.1. Oxygen permeability of PEI/GO assemblies on PET.

Recipe	OTR[a] ($cc/m^2 \cdot day \cdot atm$)		Film Thickness (nm)	Permeability ($\times 10^{-16} \cdot cm^3 \cdot cm/cm^2 \cdot s \cdot Pa$)	
	0% RH	100% RH		Assembly[b]	Total
179 μm PET	8.48	8.48	N/A	N/A	17.3
$(PEI/GO_{0.01})_{10}$	1.28	N/A	42	0.0014	2.62
$(PEI/GO_{0.01})_{20}$	0.43	N/A	84	0.00087	0.88
$(PEI/GO_{0.01})_{30}$	0.27	N/A	128	0.00082	0.55
$(PEI/GO_{0.05})_{10}$	0.77	1.20	50	0.00097	1.58
$(PEI/GO_{0.05})_{20}$	0.31	0.57	98	0.00072	0.63
$(PEI/MMT_{0.05})_{20}$[c]	6.12	N/A	52	0.0256	12.52
$(PEI/GO_{0.05})_{30}$	0.19	0.36	149	0.00066	0.39
$(PEI/GO_{0.2})_{10}$	0.12	N/A	91	0.00025	0.25
$(PEI/MMT_{0.2})_{10}$[d]	5.60	N/A	28	0.914	1001.91

[a] OTR measured at 23°C by MOCON using an Oxtran 2/21ML instrument in accordance with ASTM D-3985.[199]

[b] Film permeability was decoupled from the total permeability using a previously described method. [146]

[c] This result is from ref[50].

[d] This result is from ref[8].

5.4 Conclusions

Layer-by-layer thin films, assembled with polyethylenimine and graphene oxide, were shown to have a high GO loading (88 ~ 91 wt%), high transparency and extremely low oxygen permeability. A 91 nm film, consisting of 10 bilayers of PEI and GO, exhibits an oxygen permeability of 2.5×10^{-20} $cm^3 \cdot cm/cm^2 \cdot s \cdot Pa$, which is the same order of magnitude as SiO_x nanocoatings and five or more orders of magnitude better than traditional polymer-GO bulk composites (i.e., thick film). This impressive gas barrier comes from a tightly packed nanobrick wall structure that creates super tortuosity and diffusion length for oxygen molecules. These films exhibit the lowest oxygen permeability of any published graphene-based polymer composite. With the ability to also impart electrical conductivity through an aqueous reduction process,[269] a single film could potentially be both transparent electrode and barrier for flexible electronics.

CHAPTER VI

INFLUENCE OF DEPOSITION TIME ON LAYER-BY-LAYER GROWTH OF CLAY-BASED THIN FILMS*

6.1 Introduction

Montmorillonite (MMT) and laponite (LAP) are two of the most commonly used smectite clays, comprised of silicon-oxygen tetrahedral sheets and aluminum or magnesium oxygen-hydroxyl octahedral sheets.[108] For both of these clay types, one octahedral sheet is sandwiched by two tetrahedral sheets, which forms a 2:1 layer structure (Fig. 2.2). When added to water, these negatively charged sheets exfoliate completely through a cation exchange process.[108] The thickness of each exfoliated montmorillonite platelet is around 1 nanometer, and the lateral dimension is 200 nanometers on average.[110] Laponite is a synthetic clay, whose single crystal is disc shaped with a thickness around 0.92 nanometers and uniform diameter around 25 nanometers.[270] In other words, montmorillonite is a polydisperse natural clay with aspect ratio ranging from 200~1000 and laponite is a synthetic clay with a nearly monodisperse aspect ratio around 27.

Despite intense study of various parameters that control LbL film growth[47, 48, 51-56], the influence of deposition time has received little attention.[10, 56]In the present work, layer-by-layer assembly of polyethylenimine with MMT and LAP is studied, with a

---

*Reprinted with permission from "Influence of Deposition Time on Layer-by-Layer Growth of Clay-Based Thin Films" by You-Hao Yang etc., *Industrial & Engineering Chemistry Research* **2010**, *49*(18), 8501-8509. © 2010 American Chemistry Society.

focus on the influence of the deposition time on film growth. Ellipsometry and reflectometry data show linear thickness growth with all exposure times (ranging from 5 s to 5 min). Quartz crystal microbalance (QCM) data indicate that the mass of laponite-based films are more sensitive to deposition time than montmorillonite, which was found to be nearly unaltered. Thin film densities of the two clay systems were also calculated to better explain the dependency of deposition time. TEM images and XRD data confirm the layered structure and consistent gallery spacing with varying deposition times. SEM and AFM images provide topography and roughness comparisons between the different clays and deposition times. Finally, oxygen permeability of PEI/MMT assemblies reveal exceptional barrier behavior for both short and long deposition time, suggesting the ability to build LbL films at a much faster rate.

6.2 Experimental

6.2.1 Preparation of Deposition Mixtures

Laponite (Laponite RD, Southern Clay, Gonzales, TX) and sodium montmorillonite (Cloisite Na^+ Southern Clay, Gonzalez, TX) clays were exfoliated in deionized water, creating 1.0 wt% anionic mixtures, whose unaltered pH levels are 10.1~10.2 and 9.7~9.8, respectively. Other materials are identical to those described in Chapter III (Section 3.2.1).

6.2.2 Substrates

X-ray diffraction (XRD) measurements are made on piranha treated silicon wafers coated with a given assembly. Other substrates are identical to those described in Chapter III (Section 3.2.2).

6.2.3 Layer-by-layer Film Deposition

The overall deposition process is shown in Figure 6.1. First, a given substrate was dipped into the polycation (PEI) solution for 5 minutes. Then the substrate was rinsed with deionized water for 30 seconds and dried with a stream of filtered air. After the first positively charged layer was adsorbed, the substrate was dipped into the anionic (MMT or LAP) suspension for another 5 minutes followed by another rinsing and drying cycle. Starting from the second deposition cycle, the remaining number of bilayers were created using deposition times ranging from 5 seconds to 5 minutes, as specified in the text or figures. One polymer-clay bilayer is abbreviated as $(PEI/MMT)_1$ or $(PEI/ LAP)_1$. Except for MOCON samples, all other LbL films were made by hand dipping.

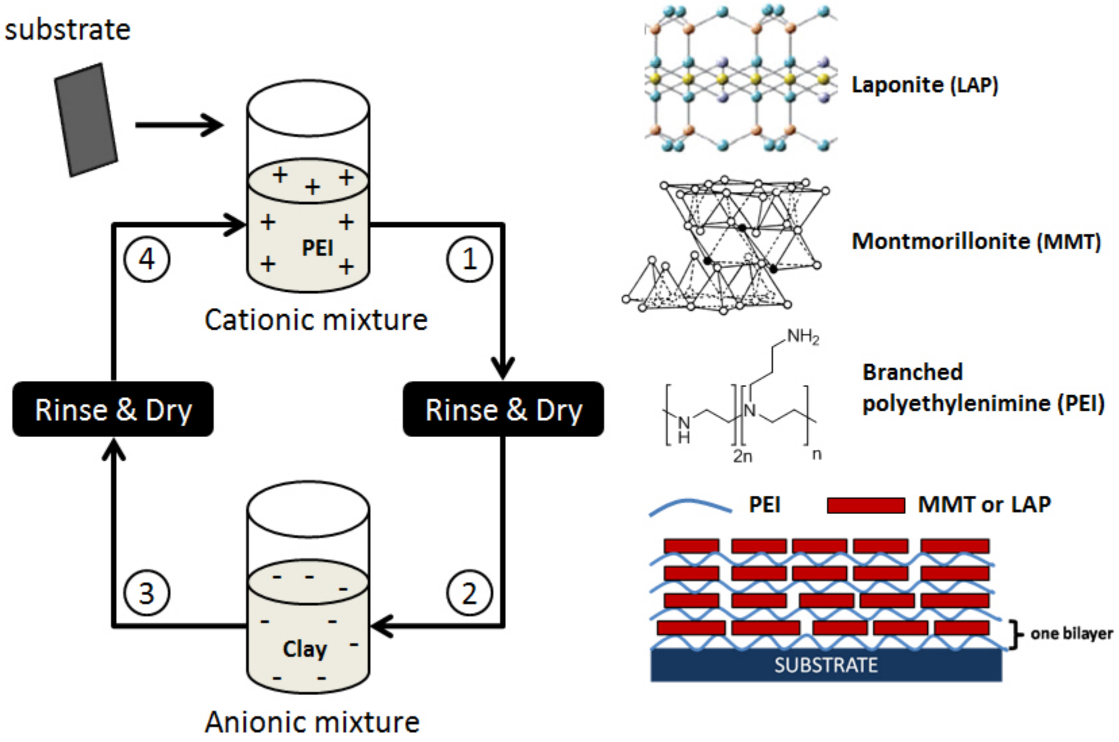

Figure 6.1. Schematic of the layer-by-layer deposition process for clay-based assemblies. Steps 1-4 are repeated until the desired number of bilayers are deposited.[188]

6.2.4 Thin Film Characterization

An F20 Thin Film Reflectometer (Filmetrics, San Diego, CA) was used to measure the thickness as a confirmation of ellipsometry. Atomic force microscope (AFM) (Nanoscience Instruments, Inc., Phoenix, AZ) images were gathered in tapping mode with XYNCHR and ACL-A cantilever tips. A Bruker AXS D8 Advanced Bragg-Brentano X-ray diffractometer (CuKα, $\lambda = 1.541$Å; Bruker AXS Inc., Madison, WI) was used for powder and glancing-angle XRD. Surface morphologies of coated PET films were imaged by a Quanta 600 FE-SEM (FEI Company, Hillsboro, OR). Samples were coated with 4 nm Pt/Pd before imaging. Other characterization methods are identical to those described in Chapter III (Section 3.2.4)

6.3 Results and Discussion

6.3.1 Influence of Deposition Time on Film Growth

Ellipsometery and reflectometry data in Figure 6.2 show linear thickness growth for both LAP and MMT systems at varying deposition times. For the LAP system, thickness growth rate increases significantly with increasing deposition time. The thickness of $(PEI/LAP)_{30}$ with 300 second dips is about 92% thicker than with 5 second. On the other hand, the thickness growth rate of the MMT system remained relatively constant with increasing deposition time. Thickness of $(PEI/MMT)_{30}$ with 300 second dips is only about 22% thicker than 5 second. QCM data, shown in Figure 6.3, also show linear growth in both the LAP and MMT systems for different deposition times. For the LAP system, mass growth increased from 11.3 to 15.5 $\mu g/cm^2$ as deposition time increased from 10 seconds to 300 seconds. For the MMT system, 10 seconds and 60 seconds show nearly the same growth rate, while 300 seconds shows faster mass growth than the others. The average mass and thickness per bilayer, and the calculated densities, are summarized in Table 6.1.

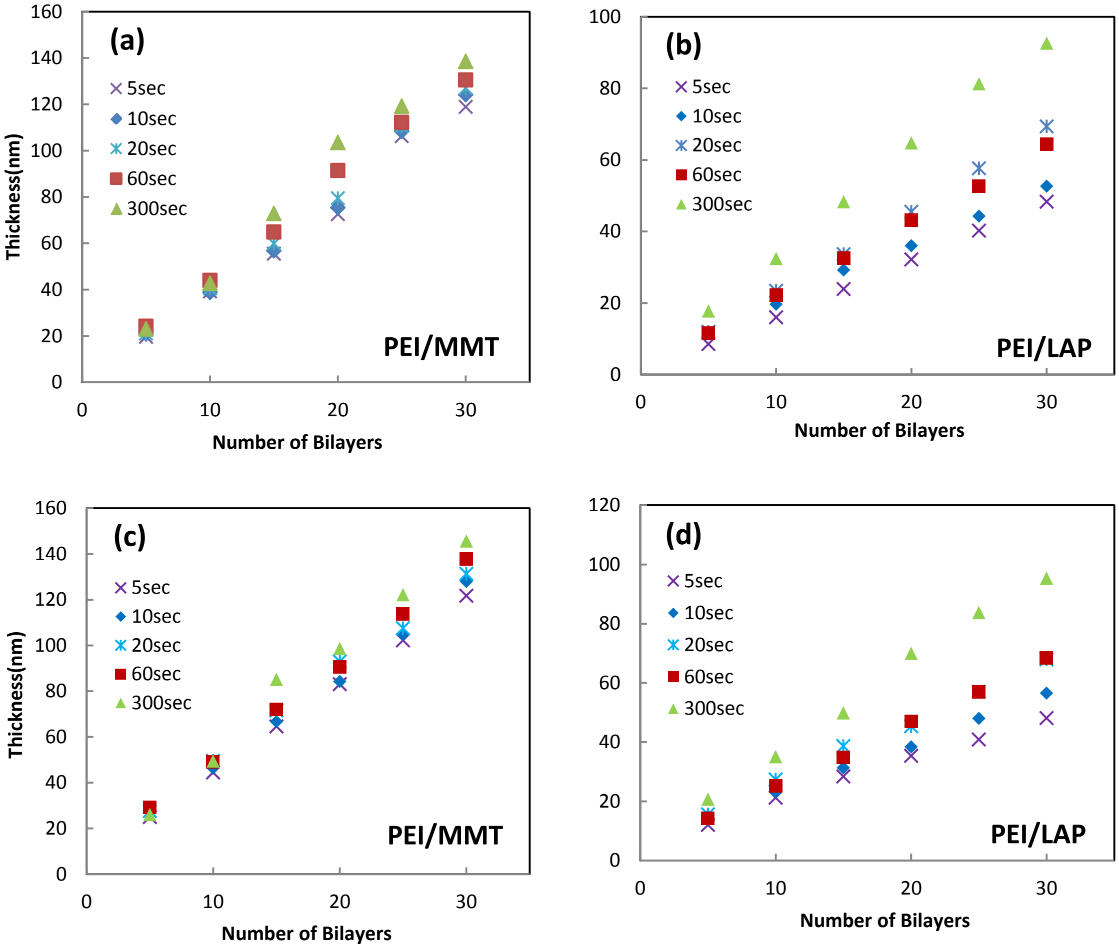

Figure 6.2. Film thickness as a function of bilayers deposited for LbL assemblies made with varying deposition times. Ellipsometry (a,b) and reflectometry (c,d) show very similar growth trends, which confirms the accuracy of these measurements.[188]

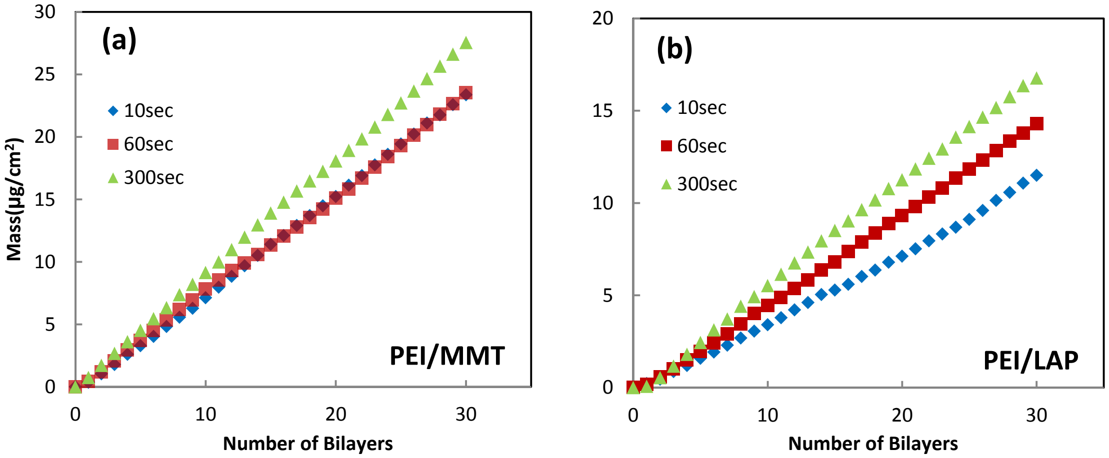

Figure 6.3. Mass per deposited bilayers for assemblies made with varying deposition times, as measured with QCM. PEI/MMT(a) and PEI/LAP(b).[188]

Table 6.1. Thickness, weight and density per bilayer for PEI/clay thin films.[188]

	MMT			LAP		
Dip Time (sec)	thickness (nm)	weight (μg/cm^2)	density (g/cm^3)	thickness (nm)	weight (μg/cm^2)	density (g/cm^3)
10	4.14	0.78	1.88	1.63	0.38	2.35
60	4.35	0.78	1.80	2.14	0.48	2.22
300	4.62	0.92	1.99	3.09	0.56	1.81

The hypothesized mechanism for the difference in growth between MMT and LAP, for long and short deposition times, is illustrated in Figure 6.4. For the MMT system, more platelets are deposited in long deposition times than in short deposition times, which can be confirmed by the QCM data in Figure 6.3 that shows greater mass at longer time. Even with greater mass, the thickness remains almost the same based upon ellipsometry and reflectometry data (Fig. 6.2(a) and (b)). It is assumed that the large aspect ratio of MMT platelets allows them to bridge defects in the underlying PEI layer, making the total thickness the same with fewer deposited platelets relative to longer deposition time. For the LAP system, more platelets are also deposited for longer deposition times (Fig. 6.3), but unlike the MMT system, the films grow thicker with longer deposition times. This trend can be explained by the geometry of the LAP platelet[270], with nearly ten times smaller diameter than MMT, which can be deposited into the defects of every PEI layer. In short deposition times, fewer LAP platelets are deposited and stay inside of polymer interchain gaps or voids. Instead of lying on top of polymer layers, LAP platelets prefer to stay inside of interchain or intrachain voids because of the stronger electrostatic attractions. Moreover, free surfaces of the polymer layer can be decreased by inserting LAP platelets, which can also decrease the total surface energy of the structure.

With long deposition times, the structure is more like the MMT system, which has a full coverage clay layer stacking on top of every polymer layers. Long dip time allows more polymer and clay to be deposited, creating fewer free surfaces and voids in polymer layers. LAP platelets can only stack on top of polymer layers, creating a stratified clay layers and an overall thicker film than short dip time. Since the density of clay is higher than polymer (PEI: 1.03 g/cm^3, LAP: 2.53 g/cm^3, MMT: 2.86 g/cm^3), the overall density of an LbL film is controlled by the deposited components and layering structure. Table 6.1 shows the thickness, mass and calculated density measured from ellipsometry and QCM. In the MMT system, densities of the three films seem to stay in the same range from 1.8 g/cm^3 to 2.0 g/cm^3 regardless of dip time. In the LAP system, both weight and thickness increase with increasing dip time. It should be noted that the increase of weight is slower than the increase of thickness, which results in the decrease of calculated density as the dip time increases. The slower thickness increase from short dip time comes from the geometric effect of LAP platelets mentioned above, which contribute the most to the increasing density trend with decreasing the deposition time.

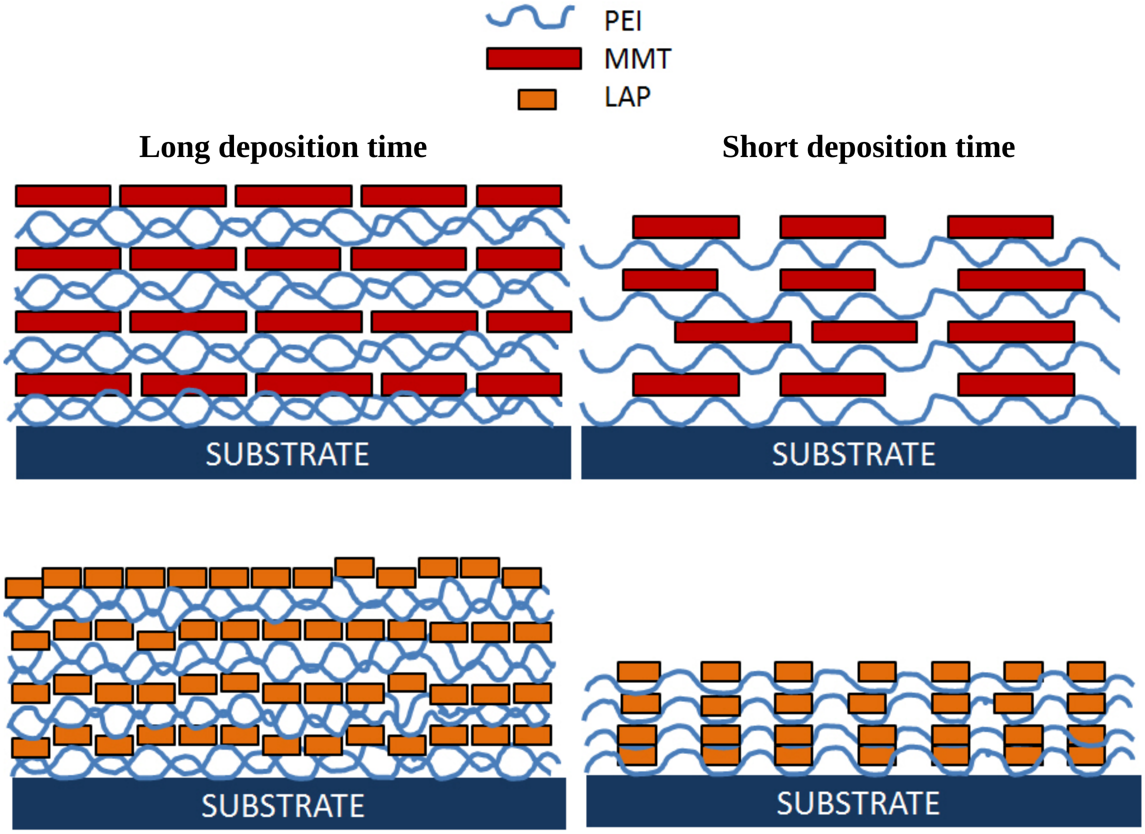

Figure 6.4. Proposed film growth mechanism for PEI/MMT and PEI/LAP with different deposition times. The larger MMT platelets are able to bridge defects in the underlying PEI layer, which allows overall film thickness to be relatively unaltered by deposition time. Laponite platelets are nearly an order of magnitude smaller in diameter, so thickness varies greatly with deposition time due to an inability to bridge.[188]

In an effort to clarify the individual dependences of deposition times, long and short times were mixed and matched for LAP and MMT. Ten seconds was chosen as the shortest deposition time and 300 seconds as the longest. Figure 6.5 shows the thickness growth profile using the shortest and longest deposition times for PEI/MMT and PEI/LAP systems, respectively. An average thickness comparison per bilayer for these systems is summarized in Table 6.2. QCM data, shown in Figure 6.6, also shows the same linear growth profile as the ellipsometry results (Fig. 6.5). For PEI, the mass with either clay system remains unaltered as the deposition time changes from 10 seconds to 300 seconds, with clay held constant at either 10 seconds or 300 seconds, which reveals a rapid adsorption rate. When the substrate is dipped into the polymer solution, the mobile polymer chains can easily deposit onto the negatively charged sites in a short time.

Interlayer diffusion is another contributor to polymer deposition consistency,[16] because excess polymer can diffuse more deeply into the film and bind to vacant negatively charged sites, which causes each polymer layer to be more fully packed. For MMT, thickness and mass per bilayer for differential deposition time combinations shows the same result as identical deposition time experiments (compare Tables 6.1 and 6.2). Individually tuning deposition time for either PEI or MMT does not result in significant changes in either thickness or mass growth. For LAP, unlike MMT, the film gets 70 to 99% thicker and 45 to 60% heavier per bilayer when tuning only LAP deposition time from 10 seconds to 300 seconds. When tuning only PEI dip time, the thickness and mass remains the same (Table 6.2). The significant difference between

MMT and LAP can be attributed to their order of magnitude difference in diameters and restricted mobility relative to PEI.

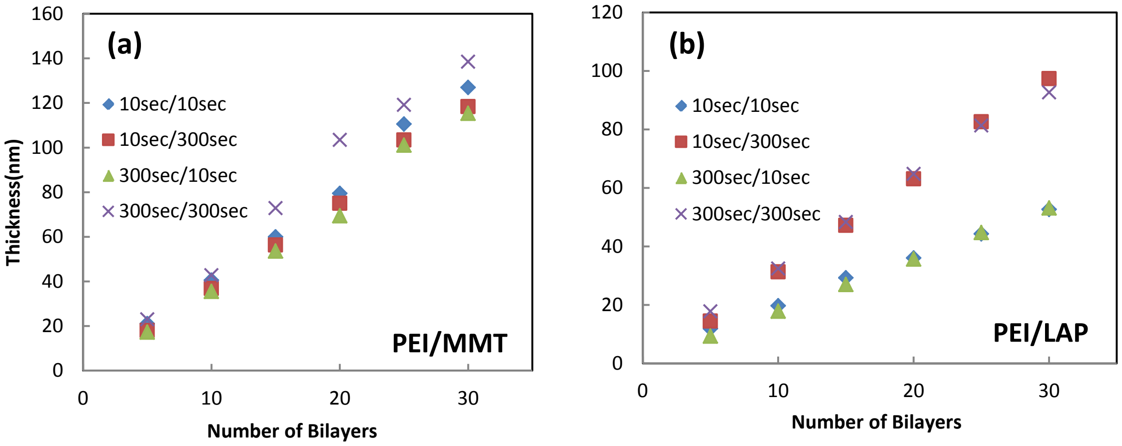

Figure 6.5. Film thickness as a function of bilayers deposited for LbL assemblies made with varying deposition time combinations for PEI/MMT (a) and PEI/LAP (b).[188]

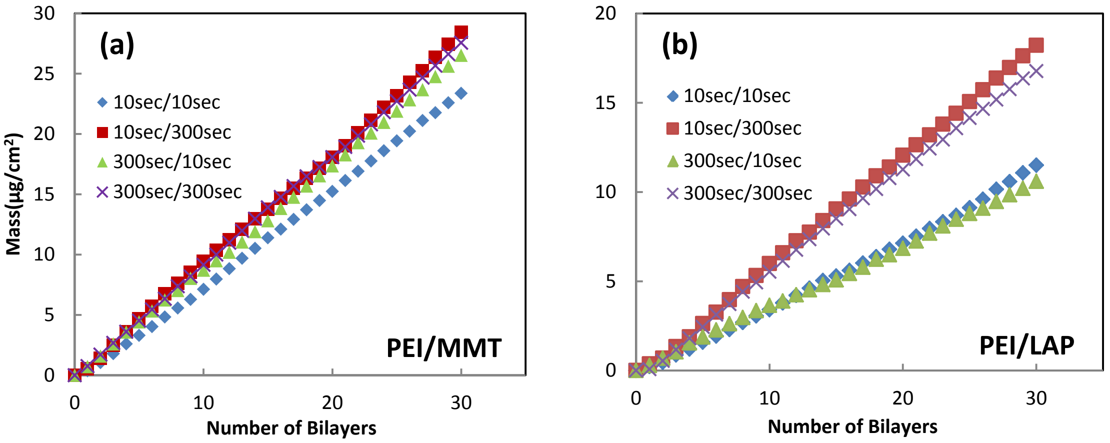

Figure 6.6. Mass deposited for assemblies made with varying deposition time combinations. PEI/MMT (a) and PEI/LAP (b).[188]

Table 6.2. Thickness, weight, and density per bilayer for PEI/MMT and PEI/LAP thin films made with combination deposition times.[188]

	MMT			LAP		
Dip Time (sec)	thickness (nm)	weight (μg/cm^2)	density (g/cm^3)	thickness (nm)	weight (μg/cm^2)	density (g/cm^3)
10/10	4.14	0.78	1.88	1.63	0.38	2.31
10/300	3.95	0.95	2.40	3.25	0.61	1.88
300/10	3.84	0.88	2.30	1.72	0.36	2.09
300/300	4.62	0.92	1.99	3.09	0.56	1.81

6.3.2 Influence of Deposition Time on Film Microstructure

Figure 6.7 shows TEM cross sections of four films with 10 and 300 second deposition times for the $(PEI/LAP)_{30}$ and $(PEI/MMT)_{30}$ systems. Each film was fabricated on PS substrates and embedded in epoxy to facilitate sectioning. The 300 seconds film is clearly thicker than 10 seconds for PEI/LAP (Fig. 6.7(a) and 6.7(b)), while in the PEI/MMT system, the film thickness remains almost the same between 10 and 300 seconds (Fig. 6.7(c) and (d)). A layered structure can be observed from the images of the PEI/MMT system, which also illustrates the exfoliation of these polymer-clay nanocomposites.[113] Stress relaxation in the films during diamond knife sectioning causes the films to appear wavy. These TEM images help to confirm the hypothesized mechanism for the difference in growth (Fig. 6.4).

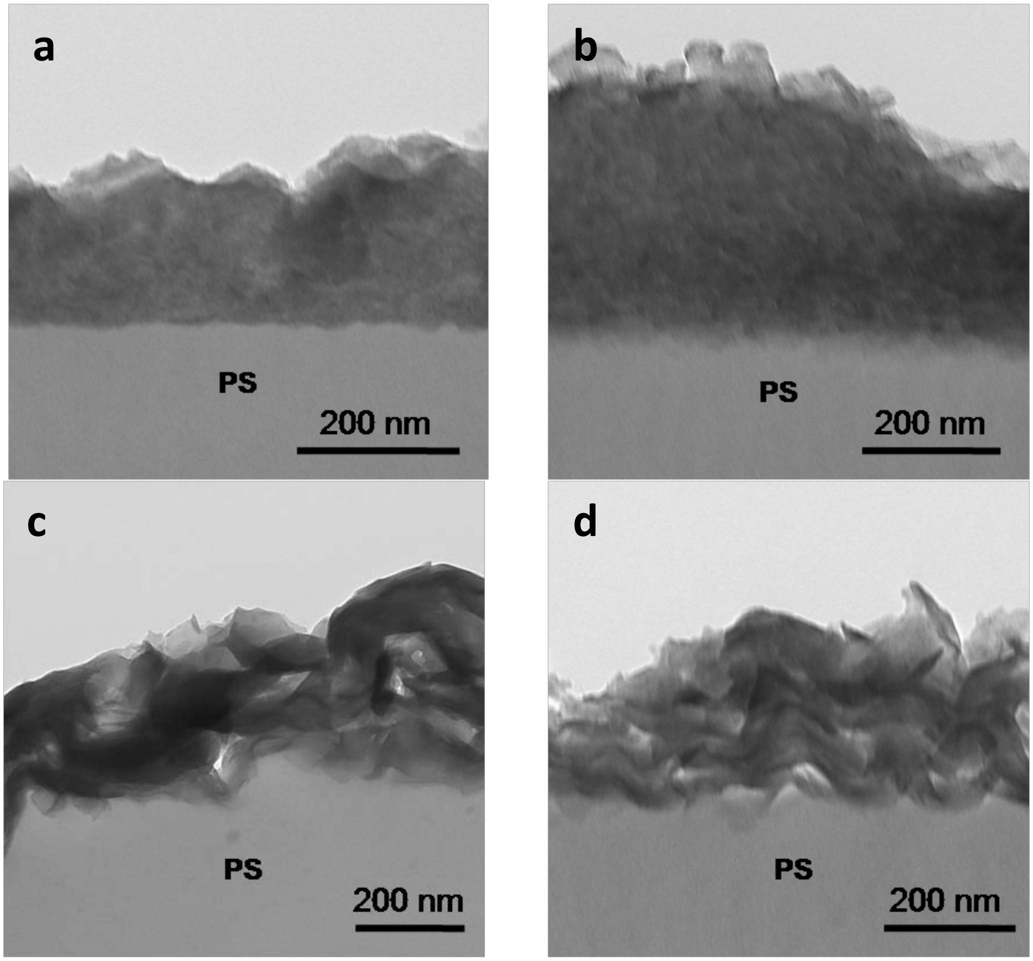

Figure 6.7. TEM cross-sectional images of $(PEI/LAP)_{30}$ on PS with 10 sec (a) and 300 sec (b) deposition times for both ingredients. $(PEI/MMT)_{30}$ on PS is also shown for 10 sec (c) and 300 sec (d) deposition times.[188]

Figure 6.8 shows SEM surface images of assemblies deposited on PET using long and short deposition times. The PEI/LAP system shows a similar uniform cobblestone pattern for both 10 and 300 second deposition times (Fig. 6.8(a) and (b)). For the PEI/MMT system, more MMT platelets are observed with 300 second dips than for 10 seconds (Fig. 6.8(c) and (d)), which agrees with the QCM results previously discussed. Silicon wafers coated with 2 bilayers of PEI and clay were imaged by AFM.

As shown in Figure 6.9, the height and phase images of the $(PEI/LAP)_2$ films for 10 and 300 second depositions have a cobblestone pattern. The film prepared with 300 second dips seems to have greater packing of LAP platelets on the top layer. The overall topography for LAP is similar for different deposition times, which is the same as the 30-bilayer SEM images.

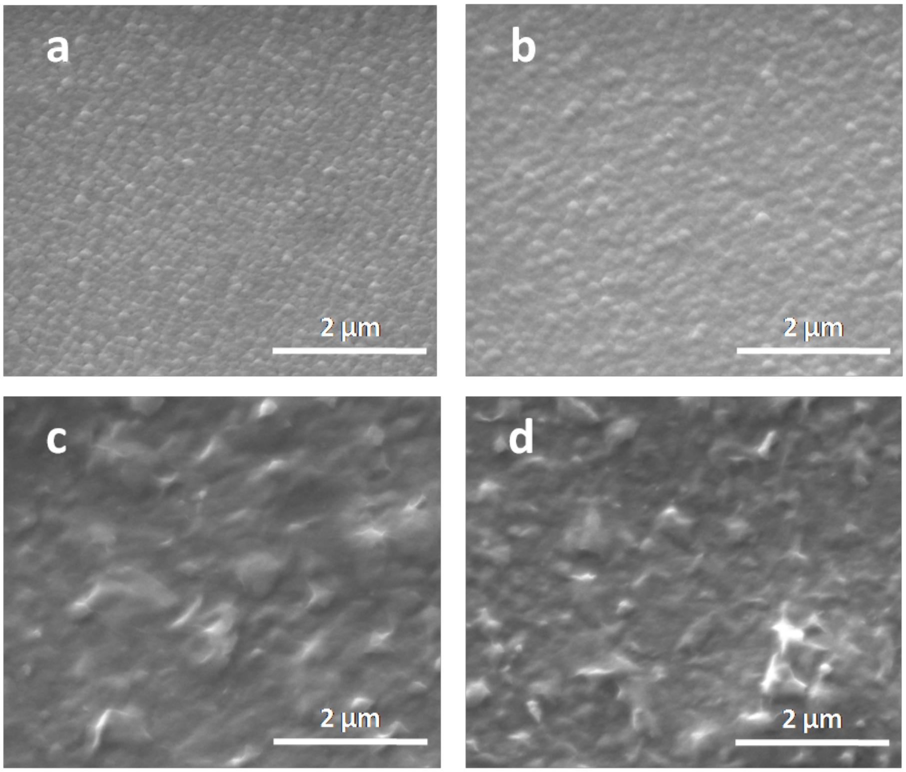

Figure 6.8. SEM surface images of $(PEI/LAP)_{30}$ on PET with 10 sec (a) and 300 sec (b) deposition times for both ingredients. $(PEI/MMT)_{30}$ on PET is also shown for 10 sec (c) and 300 sec (d) deposition times.[188]

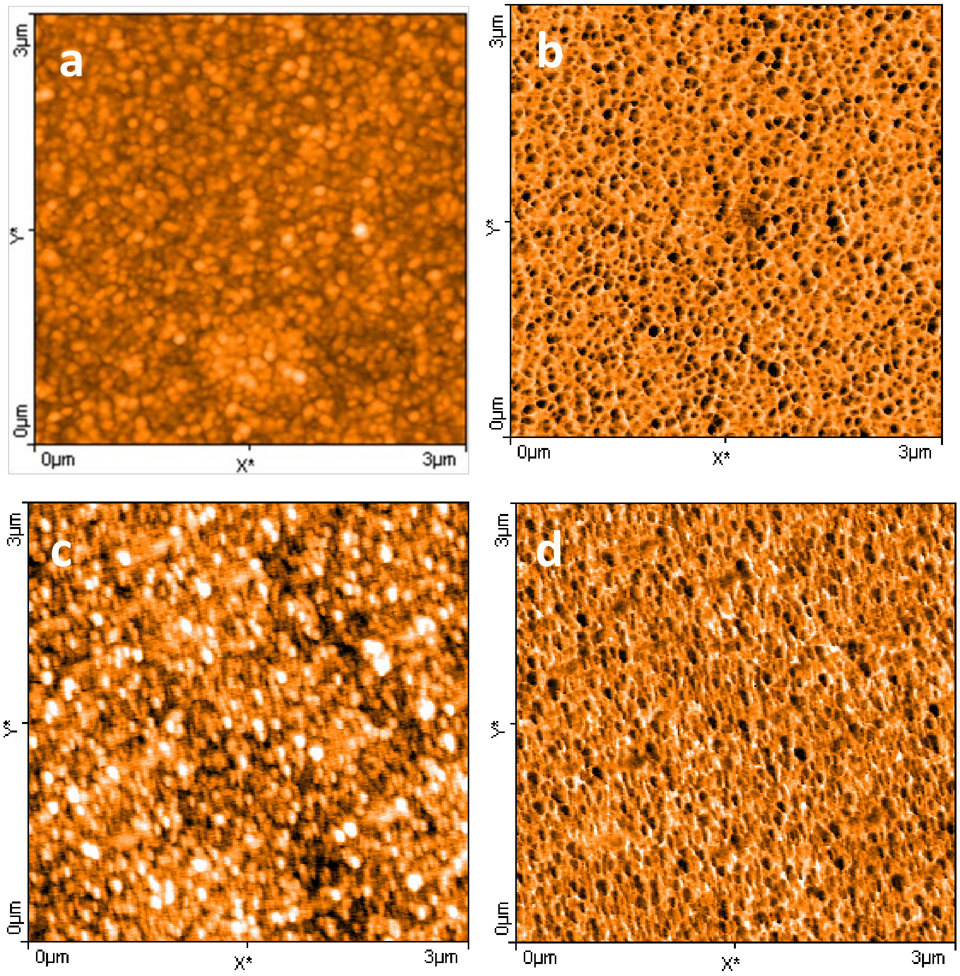

Figure 6.9. AFM height (a, c) and phase (b, d) surface images of $(PEI/LAP)_2$ films. Films were made with 10 sec (a, b) and 300 sec (c, d) deposition times.[188]

Figure 6.10 shows the height and phase images for $(PEI/MMT)_2$. MMT is a natural clay, which contributes to its less uniform topography at both 10 and 300 seconds. Moreover, the 300 second film shows a more close packed arrangement of MMT platelets that highlights the polydispersity and larger size of this clay relative to LAP (Fig. 6.9). Shorter deposition time allows fewer MMT platelets to deposit onto the substrate, which makes the surface rougher than longer deposition time. The rms surface roughness of $(PEI/MMT)_2$ is 31.5 nm for 10 seconds and 21.6 nm for 300 seconds, while $(PEI/LAP)_2$ is 3.6 nm for 10 seconds and 2.6 for 300 seconds. All the roughness values were calculated using 20 × 20 μm areas. In both PEI/MMT and PEI/LAP systems, smoother films are achieved with longer deposition time, which is supported by all of the images shown in Figures 6.8-10.

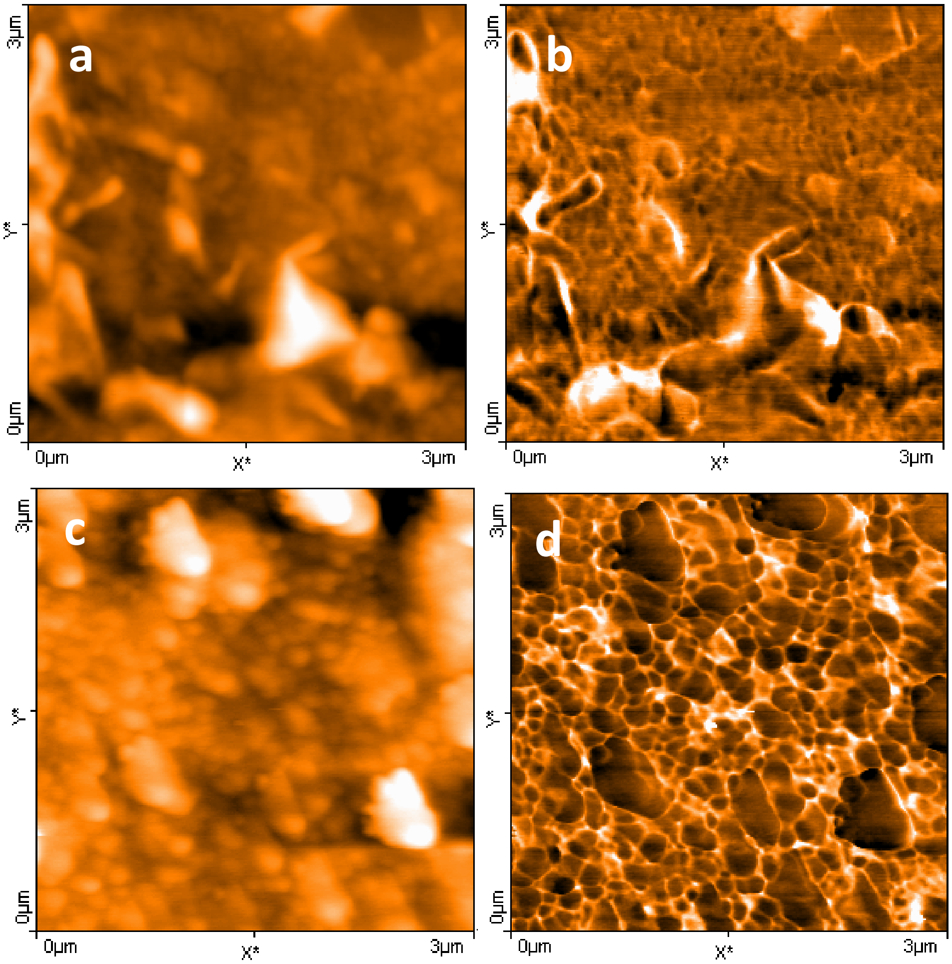

Figure 6.10. AFM height (a, c) and phase (b, d) surface images of $(PEI/MMT)_2$ films. Films were made with 10 sec (a, b) and 300 sec (c, d) deposition times.[188]

Figure 6.11(a) shows the XRD patterns of neat LAP powder and two LbL films made with varying deposition times. Neat LAP powder exhibits a peak at 6.8° that corresponds to a basal distance (d_{001}) of 12.98 Å. This spacing agrees with the reported value in the literature.[271] As the thickness of each LAP platelet is about 1 nm, the gallery spacing is then ~ 3 Å. The pattern for the 10 seconds PEI/LAP system shows a peak at 6.1° (d_{001}=14.47 Å), while 300 seconds has a slightly higher angle at 6.24° (d_{001}=14.15 Å). In both cases, intercalation of polymer during deposition results in increased platelet spacing. A similar trend is observed with the MMT-based films, as shown in Figure 6.11(b). Neat MMT powder shows a peak at 7.73° (d_{001}=11.43 Å) that reduces to 6.41° (d_{001}=13.77 Å) for 10 seconds and 6.38° (d_{001}=13.85 Å) for 300 seconds. Similar to LAP, the increased gallery spacing can also be attributed to intercalated polymer chains, which are 2.34 Å for 10 seconds and 2.42 Å for 300 seconds. The level of intercalation appears to be more influenced by clay type than deposition time. These results suggest that short deposition time can generate a comparable through thickness structure to films made with long deposition time. This is an important result for those seeking to use this methodology in a commercial setting.

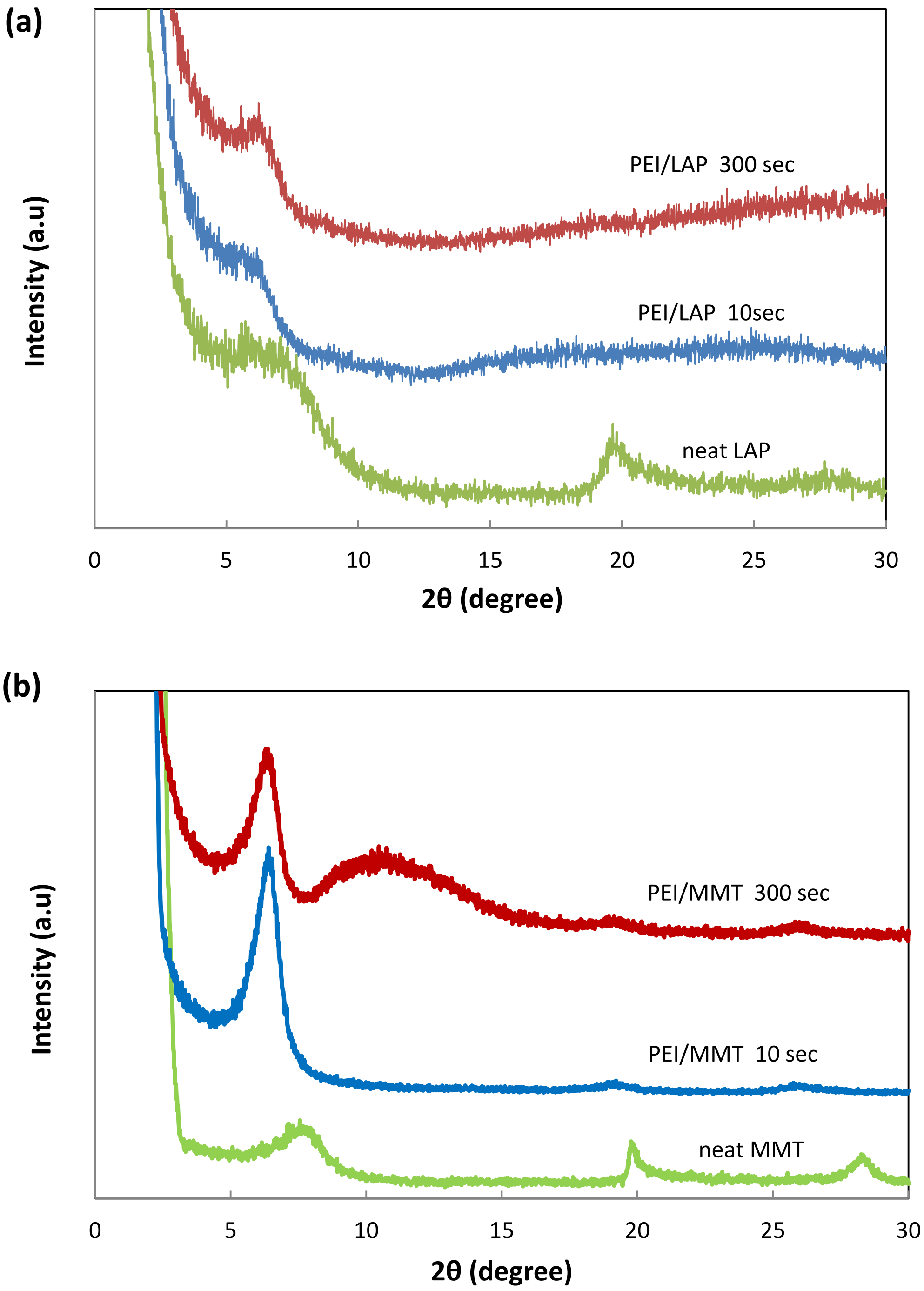

Figure 6.11. XRD patterns for neat LAP and 30-BL films made by varying the deposition time of PEI and LAP solutions (a). The same patterns are shown for MMT (b).[188]

6.3.3 Influence of Deposition Time on Oxygen Barrier Behavior

Similar clay-polymer assemblies have already been shown to achieve low oxygen transmission rates (OTR < 0.005 cc/m^2 · day at 23°C and 0% RH) on PET film using one minute dip times.[8, 129] Table 6.3 summarizes the OTR results for 30-bilayer thin films deposited on 7-mil PET with varying dip times. Compared with uncoated PET, all four (PEI/MMT)$_{30}$ films with different deposition times exhibit significant improvement in oxygen barrier performance (i.e., reduced OTR by orders of magnitude). The 10sec/10sec film reduce the OTR from 8.48 cc/m^2 · day to 0.168 cc/m^2 · day, while all the other dip times (1min/1min, 5min/5min and 10sec/5min) achieve an undetectable value (<0.005 cc/m^2 · day). Barrier is an important property for a variety of packaging applications and it is also very sensitive to small defects.

This impressive barrier for composites less than 150 nm thick is attributed to the high clay concentration (> 89 wt %) and near perfect alignment perpendicular to the permeating gas.[8, 86] Polymer chains intercalate with the MMT platelets during deposition, increasing the interlayer spacing and creating a brick wall nanostructure, which decreases the permeability of oxygen molecules. Although these four films have similar thickness, the 10sec/10sec film exhibits a weaker barrier than the others. With very short dip time in clay, fewer MMT platelets are deposited (as suggested by lower weight in Table 6.2), creating a more loosely-packed structure (see Fig. 6.4) that would be expected to have reduced barrier. The permeability values in Table 6.3 are obtained by multiplying film thickness by OTR. Except for the shortest dip time for clay, these OTR results suggest a very similar, relatively defect-free, structure that is independent of dip time. Even the 10sec/10sec film achieves a permeability close to that of SiO_x,[5, 142, 272, 273] making it an interesting alternative for transparent food, or flexible electronics, packaging.

Table 6.3. Oxygen permeability of $(PEI/MMT)_{30}$ assemblies on PET film.[188]

Dip Time (PEI/MMT) (sec)	OTR (cc/m^2 · day · atm)	Film Thickness (nm)	Permeability(×10^{-6} cc/m · day · atm)	
			Film[a]	Total
Bare PET	8.48	N/A	N/A	1517.92
10/10	0.168	124.08	0.0425	300.93
60/60	<0.005[b]	130.44	<0.0013[b]	<0.9[b]
300/300	<0.005	138.49	<0.0014	<0.9
10/300	<0.005	118.35	<0.0012	<0.9

[a] Film permeability was decoupled from the total permeability using a previously described method .[146]

[b] The low end detection limit for an Ox Tran 2/21 L module is 0.005 cc/m^2 · day.

6.4 Conclusions

The influence of deposition time on film growth and microstructure of clay-based layer-by-layer assemblies was studied. Large diameter MMT platelets (d ~ 200nm) showed little sensitivity to deposition time in terms of film growth, but density increased (and roughness decreased) with longer deposition times. It is believed that these large platelets can bridge film defects in the underlying polymer layer. The PEI/LAP system, in contrast, shows strong dip time dependence in film growth because of the smaller diameter of LAP (d ~ 25nm), which makes them less able to bridge recesses in the polymer layer. TEM cross-sectional images show thicker PEI/LAP films with longer deposition time. SEM and AFM surface images show a highly-ordered cobblestone pattern for the PEI/LAP system for all deposition times, while PEI/MMT shows less uniformity and organization at short times. Low OTR results demonstrate that high quality films can be assembled when decreasing the deposition time of PEI. Generally speaking, short dip times (< 1 min.) appear to generate similar films to longer times in terms of thickness and structure, especially in the case of larger clay platelets. This work should be served as a step toward achieving faster deposition of multifunctional LbL films, which is a key issue facing their commercial use.

CHAPTER VII

CONCLUSIONS AND FUTURE WORK

The ultimate goal of this dissertation research was to improve the processing and oxygen barrier behavior of nanocoatings deposited on permeable polymeric substrates. Polymer-polymer and polymer-nanoplatelet layer-by-layer assemblies both reduce the oxygen transmission rate more than three orders of magnitudes relative to an uncoated PET, with coating thickness ranging from 100 ~ 500 nm. Crosslinking these films improves oxygen barrier at high humidity. Furthermore, Polymer-clay assemblies can be processed with relatively fast deposition cycles. This works lays the foundation for the use of layer-by-layer assembly as an effective fabrication technology for making ultrathin, transparent super gas barrier layers that are important for a variety of packaging applications.

7.1 Super Gas Barrier of Weak Polyelectrolytes Thin Films

Layer-by-layer multilayer films fabricated with two weak polyelectrolytes, PEI and PAA, exhibited a pH-dependent behavior in terms of growth, microstructure and oxygen barrier. A $(PEI_{10}/PAA_{4})_{30}$ film, with the lowest combined polymer charge density, is 50 times thicker than a $(PEI_{7}/PAA_{7})_{30}$ film, which has the highest combined charge. Surface roughness of a low charge density film is higher than the film with high charge density. Compared to other pH combinations, only PEI_{10}/PAA_{4} obtained a high oxygen barrier. An 8BL PEI_{10}/PAA_{4} film, with a thickness 451 nm, exhibits an undetectable OTR < 0.005 $cc/m^2 \cdot day$ and an oxygen permeability < 4.8×10^{-21} $cm^3 \cdot cm/cm^2 \cdot s \cdot Pa$. Due to the scrambled egg structure, with numerous cation/anion interfaces created by LbL, this film is believed to be the first all-polymer material, with low oxygen permeability, which can compete with SiO_x nanocoatings. This relatively simple recipe may be of use for a variety of packaging applications, such as food and flexible electronics packaging.

7.2 Influence of Crosslinking on Gas Barriers of Weak Polyelectrolyte Thin Films

The influence of crosslinking on PEI/PAA films was examined with regard to three methods: GA, EDC and heat. Different crosslinking concentrations, temperatures and times resulted in thickness variations, ranging from 600 to 1300 nm, for crosslinked 10BL films. FTIR spectra confirm that covalent bonds were created by this crosslinking, with increasing extent of reaction accompanied by increasing the crosslinker concentration or temperature. 8BL films crosslinked with 0.1M GA or 0.01M EDC exhibit the lowest OTR at 100% RH, indicating that PEI/PAA films gain some water resistance after crosslinking. A 50BL film crosslinked at 150°C exhibits a 46% WVTR improvement, indicating that PEI/PAA films are still quite water permeable and more works need to be done. This study marks the first systematic study of crosslinking and its influence on the barrier properties of LbL assemblies.

7.3 Super Gas Barrier of Polymer-Graphene Oxide Films

PEI/GO multilayer thin films were made via LbL with varying GO concentrations. Films grow linearly with average bilayer thickness from 4.3 to 5.0 nm as deposition solution concentration is varied from 0.01 to 0.05 wt%. QCM results show these films are highly GO loaded, with mass fraction of 88~91% in 20BL PEI/GO films. AFM images show individual GO sheets on the film surface, with an aspect ratio from 0.2 to 3 μm. Cross-sectional TEM images show well-separated GO sheets inside of the polymer matrix, suggesting a perfectly oriented nanobrick wall structure. A 10BL PEI/$GO_{0.2}$ film, with a thickness of 91 nm, achieves an oxygen permeability of 2.5×10^{-20} $cm^3 \cdot cm/cm^2 \cdot s \cdot Pa$, which is comparable to a 100 nm SiO_x nanocoating. At the same number of bilayers, the barrier performance of PEI/GO is orders of magnitude better than PEI/MMT due to greater aspect ratio. This study demonstrates super gas barrier thin films made with GO as the impermeable platelet. This system could be furthered optimized for applications like transparent electrodes and barrier for flexible electronics, perhaps in a single thin film.

7.4 Influence of Deposition Time on Polymer-Clay Thin Films

LbL assemblies fabricated using PEI with two different aspect ratio clays, MMT and LAP, were examined in terms of various deposition times, from 5 seconds to 5 minutes. Ellipsometry and QCM growth both show that PEI/LAP films are more dip time dependent than PEI/MMT because smaller aspect ratio clay can reside in morphological polymer defects, while larger aspect ratio clay bridges onto those defects.

XRD suggests the gallery spacing between clay layers is insensitive to dip time, which is a key structural parameter linked to both mechanical and transport properties of these types of films. By changing the deposition time of PEI from 5 minutes to 10 seconds, and keeping the same deposition time of MMT, the OTR remains undetectable (< 0.005 $cc/m^2 \cdot day$), which indicates that high gas barrier films can be processed very quickly. This is an important revelation that increases the likelihood of commercial success for these nanocoatings.

7.5 Future Research Plans

From the results in Chapters III and IV, it is clear that PEI/PAA assemblies exhibit good oxygen barrier under dry conditions, but relatively poor barrier under humid conditions due to the hydrophilic nature of the polymers. Especially for moisture barrier, little WVTR decrease was observed in these films. New approaches for making more water resistant LbL films are needed for commercial applications. Chapter V showed promising barrier results from PEI/GO bilayer films. Increased platelet spacing in these films further improves the gas barrier performance. Additionally, chemical reduction of GO could potentially make a gas barrier film electrically conductive, which will improve this film’s usefulness. Three areas of future research are described here as ways to address these challenges.

7.5.1 Non-Aqueous LbL Multilayer Films

Thin films fabricated with PEI and PAA are hydrophilic due to the aqueous deposition environment, allowing water molecules to easily transport through the structure. Although crosslinking these films create covalent bonds and enhanced moisture resistance, the improvement is very limited. In addition to water, other solvents can be used to successfully grow LbL films.[274, 275] The idea is to use solvents to generate films with reduced moisture sensitivity and study their oxygen and moisture barrier. Figure 7.1(a) shows that a PEI and PAA dissolved in ethanol can be used to grow LbL assemblies. Ethanol-based PEI/PAA films are thinner than water-based PEI/PAA films, with only 235 nm at 30BL (4.74 μm for water-based). The linear growth trend of ethanol-based PEI/PAA is also different from exponentially growing water-based PEI/PAA. The OTR performance of this system at 23°C and 0% RH is shown in Figure 7.1(b). This OTR is not as good as water-based PEI/PAA, on a bilayer number basis, because of the lack of thickness and a lack of cation/anion interfaces that comes with interdiffusion. It is anticipated that this sacrifice in oxygen barrier might be offset by a lower WVTR since there is no water in ethanol-based PEI/PAA. In addition to ethanol, other solvents such as butanol, toluene, and tetrahydrofuran can also be investigated. This study could provide the gas barrier community with a generalized understanding of solvent influence on gas and moisture barrier.

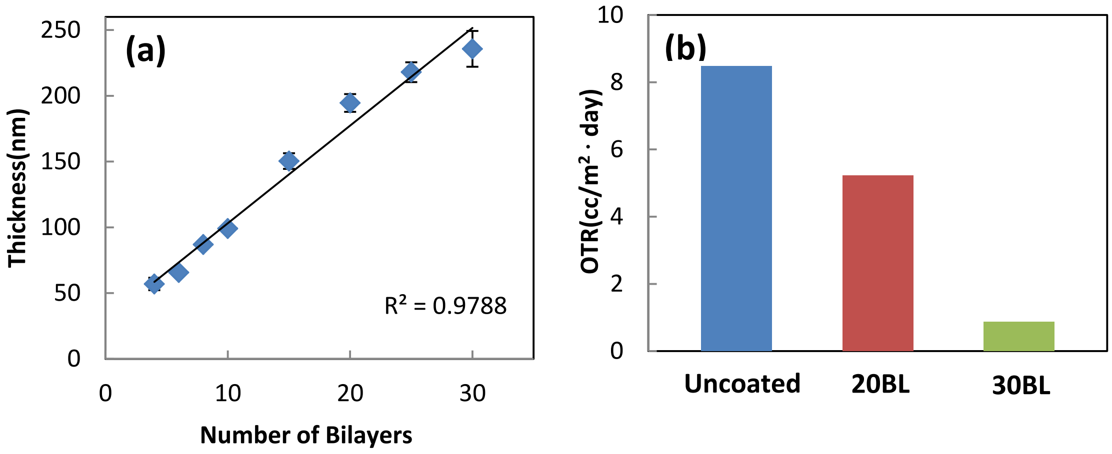

Figure 7.1. Thickness as a function of bilayers deposited from ethanol-based solutions of PEI and PAA (a). Oxygen transmission rates of ethanol-based PEI/PAA assemblies on PET film (b).

7.5.2 Quadlayer Graphene Oxide Films

PEI/GO films exhibit superior oxygen barrier with increasing number of GO layers. Similar to clay, an exfoliated single GO sheet is gas-impermeable.[187] Increasing the distance between clay platelets by adding more polymer layers has been shown to improve barrier relative to PEI/MMT bilayers, with only 4 MMT layers needed to achieve an undetectable OTR.[107] GO exhibited a better oxygen barrier than MMT with the same number of bilayers (Chapter V), which should mean that GO sheets in a PEI/PAA/PEI/GO quadlayer (QL) will also be better. Figure 7.2 shows the growth of PEI/PAA/PEI/GO from 2 to 9 QL. Unlike with clay, this system exhibits linear growth and is 87 nm thick at 9QL. In addition to the direct comparison of OTR between GO and MMT quadlayer systems, transmission rates of other gases (e.g., carbon dioxide, nitrogen and hydrogen) needs to be tested. The epoxide and hydroxyl groups on GO surfaces may result in more hydrogen bonding than MMT. Adding more PEI/PAA or other polymers between GO layers is another option to achieve greater platelet spacing and improved gas barrier. Since the interdiffusion of polymers play some role in oxygen barrier, decreasing the GO concentration (to provide PEI/PAA interdiffusion) may also help to increase the barrier. This GO quadlayer barrier could be useful for both packaging and gas separation membranes.

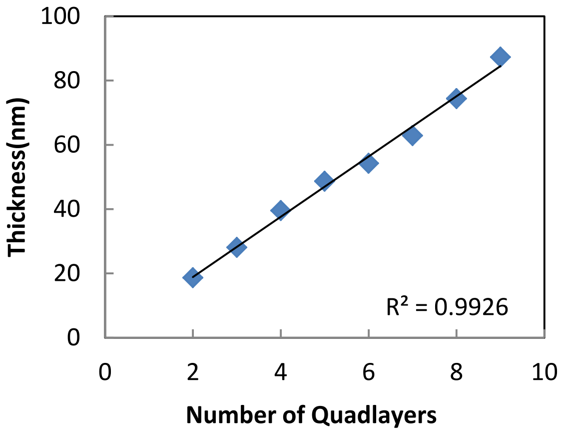

Figure 7.2. Thickness as a function of PEI/PAA/PEI/GO quadlayers deposited.

7.5.3 Conductive LbL Films with Reduced Graphene Oxide

Graphene oxide sheets are insulating due to the epoxide and hydroxyl groups that disrupt the conjugated structure. Chemical reduction of GO with hydrazine can restore electrical conductivity by rebuilding the double bonds, as shown in Figure 7.3(a).[246] LbL films with GO nanoplatelets, with outstanding gas barrier, can be reduced to become electrically conductive. The hazardous nature and cost of hydrazine makes this route somewhat impractical, so an environmental friendly reduction method using ascorbic acid (Vitamin C) is a better option.[269] Figure 7.3(b) shows sheet resistance as a function of reduction time of 20BL PEI/GO with 1.0 wt% ascorbic acid at 80°C. This initially insulating thin film becomes conductive after 2 hours of reduction. Optimizing the experimental parameters (concentration of ascorbic acid, reduction time, reduction temperature, and number of bilayers) could potentially make this film both electrical conductive and gas impermeable. Other reduction methods, such as heating can also be investigated.[276]

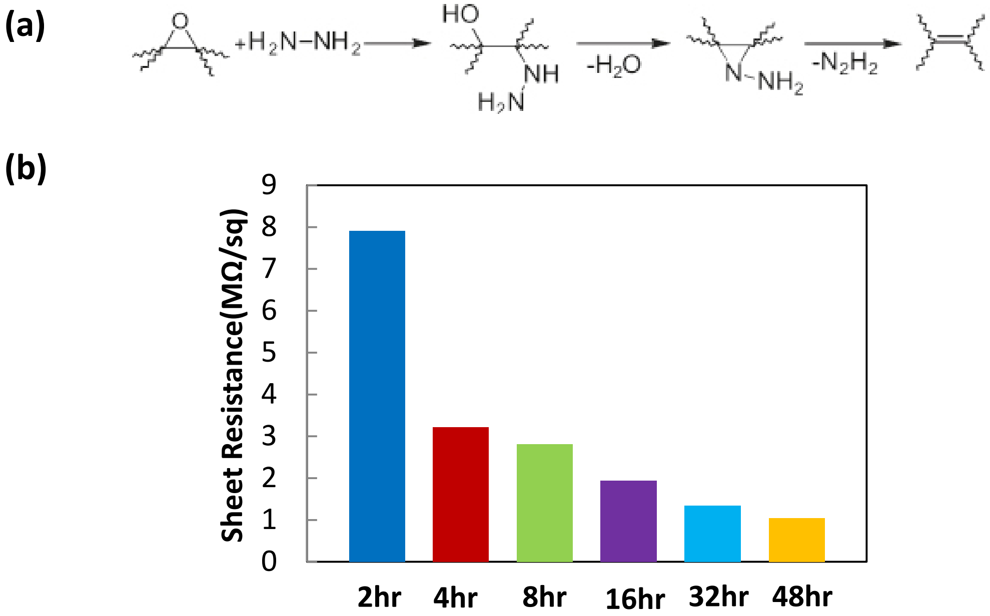

Figure 7.3. Reduction mechanism of graphene oxide by hydrazine (a).[246] Sheet resistance of $(PEI/GO)_{20}$ films on PET as a function of reduction time by ascorbic acid (b).

REFERENCES

1. World Packaging Organisation. Market Statistics and Future Trends in Global Packaging. http://www.worldpackaging.org (accessed Jun 1, 2012).

2. Piringer, O. G.; Baner, A. L. *Plastic Packaging Materials for Food : Barrier Function, Mass Transport, Quality Assurance, and Legislation*. Wiley-VCH: New York, NY, 2000.

3. Strupinsky, G.; Brody, A. L. *Polymers, Laminations & Coatings Conference* **1998**, 119-140.

4. Brooks, D. W.; Giles, G. A.; Knovel (Firm). *PET Packaging Technology*. CRC Press: Boca Raton, FL, 2002.

5. Bieder, A.; Gruniger, A.; von Rohr, P. R. *Surface & Coatings Technology* **2005,** 200, (1-4), 928-931.

6. Sothornvit, R.; Hong, S. I.; An, D. J.; Rhim, J. W. *Lwt-Food Science and Technology* **2010,** 43, (2), 279-284.

7. Tetsuka, H.; Ebina, T.; Nanjo, H.; Mizukami, F. *Journal of Materials Chemistry* **2007,** 17, (33), 3545-3550.

8. Priolo, M. A.; Gamboa, D.; Grunlan, J. C. *Acs Applied Materials & Interfaces* **2010,** 2, (1), 312-320.

9. Bertrand, P.; Jonas, A.; Laschewsky, A.; Legras, R. *Macromolecular Rapid Communications* **2000,** 21, (7), 319-348.

10. Decher, G.; Schlenoff, J. B. *Multilayer Thin Films: Sequential Assembly of Nanocomposite Materials*. Wiley-VCH: New York, NY, 2003.

11. Hammond, P. T. *Advanced Materials* **2004,** 16, (15), 1271-1293.

12. Lvov, Y.; Ariga, K.; Ichinose, I.; Kunitake, T. *Journal of the American Chemical Society* **1995,** 117, (22), 6117-6123.

13. Stockton, W. B.; Rubner, M. F. *Macromolecules* **1997,** 30, (9), 2717-2725.

14. Kohli, P.; Blanchard, G. J. *Langmuir* **2000,** 16, (10), 4655-4661.

15. Yang, Y. H.; Haile, M.; Park, Y. T.; Malek, F. A.; Grunlan, J. C. *Macromolecules* **2011,** 44, (6), 1450-1459.

16. Picart, C.; Mutterer, J.; Richert, L.; Luo, Y.; Prestwich, G. D.; Schaaf, P.; Voegel, J. C.; Lavalle, P. *Proceedings of the National Academy of Sciences of the United States of America* **2002,** 99, (20), 12531-12535.

17. Lvov, Y.; Decher, G.; Mohwald, H. *Langmuir* **1993,** 9, (2), 481-486.

18. Yoo, D.; Shiratori, S. S.; Rubner, M. F. *Macromolecules* **1998,** 31, (13), 4309-4318.

19. Franzl, T.; Koktysh, D. S.; Klar, T. A.; Rogach, A. L.; Feldmann, J.; Gaponik, N. *Applied Physics Letters* **2004,** 84, (15), 2904-2906.

20. Jaffar, S.; Nam, K. T.; Khademhosseini, A.; Xing, J.; Langer, R. S.; Belcher, A. M. *Nano Letters* **2004,** 4, (8), 1421-1425.

21. Wang, X. G.; Wang, D. G. *Langmuir* **2011,** 27, (5), 2007-2013.

22. Huang, Y.; Duan, X. F.; Wei, Q. Q.; Lieber, C. M. *Science* **2001,** 291, (5504), 630-633.

23. Kotov, N. A.; Dekany, I.; Fendler, J. H. *Journal of Physical Chemistry* **1995,** 99, (35), 13065-13069.

24. Caruso, R. A.; Susha, A.; Caruso, F. *Chem Mater* **2001,** 13, (2), 400-409.

25. Gole, A.; Murphy, C. J. *Chem Mater* **2005,** 17, (6), 1325-1330.

26. Weintraub, B.; Chang, S.; Singamaneni, S.; Han, W. H.; Choi, Y. J.; Bae, J. H.; Kirkham, M.; Tsukruk, V. V.; Deng, Y. L. *Nanotechnology* **2008,** 19, (43).

27. Aroca, R. F.; Goulet, P. J. G.; dos Santos, D. S.; Alvarez-Puebla, R. A.; Oliveira, O. N. *Analytical Chemistry* **2005,** 77, (2), 378-382.

28. Mamedov, A. A.; Kotov, N. A.; Prato, M.; Guldi, D. M.; Wicksted, J. P.; Hirsch, A. *Nature Materials* **2002,** 1, (3), 190-194.

29. Ma, R. Z.; Sasaki, T.; Bando, Y. *Journal of the American Chemical Society* **2004,** 126, (33), 10382-10388.

30. Keller, S. W.; Kim, H. N.; Mallouk, T. E. *Journal of the American Chemical Society* **1994,** 116, (19), 8817-8818.

31. Zhang, S. C.; Shen, J. D.; Fu, H. B.; Dong, W. Y.; Zheng, Z. J.; Shi, L. Y. *Journal of Solid State Chemistry* **2007,** 180, (4), 1456-1463.

32. Ji, Q. M.; Honma, I.; Paek, S. M.; Akada, M.; Hill, J. P.; Vinu, A.; Ariga, K. *Angewandte Chemie-International Edition* **2010,** 49, (50), 9737-9739.

33. Ariga, K.; Lvov, Y.; Kunitake, T. *Journal of the American Chemical Society* **1997,** 119, (9), 2224-2231.

34. Zandi, M.; Hashemi, S. A.; Aminayi, P.; Hosseinali, F. *Journal of Applied Polymer Science* **2011,** 119, (1), 586-594.

35. Mirenda, M.; Strassert, C. A.; Dicelio, L. E.; Roman, E. S. *Acs Appl Mater Inter* **2010,** 2, (6), 1556-1560.

36. Tsukruk, V. V.; Rinderspacher, F.; Bliznyuk, V. N. *Langmuir* **1997,** 13, (8), 2171-2176.

37. Kim, D. H.; Karan, P.; Goring, P.; Leclaire, J.; Caminade, A. M.; Majoral, J. P.; Gosele, U.; Steinhart, M.; Knoll, W. *Small* **2005,** 1, (1), 99-102.

38. Lazzara, T. D.; Lau, K. H. A.; Abou-Kandil, A. I.; Caminade, A. M.; Majoral, J. P.; Knoll, W. *Acs Nano* **2010,** 4, (7), 3909-3920.

39. Araki, K.; Wagner, M. J.; Wrighton, M. S. *Langmuir* **1996,** 12, (22), 5393-5398.

40. Guldi, D. M.; Pellarini, F.; Prato, M.; Granito, C.; Troisi, L. *Nano Letters* **2002,** 2, (9), 965-968.

41. Richert, L.; Lavalle, P.; Payan, E.; Shu, X. Z.; Prestwich, G. D.; Stoltz, J. F.; Schaaf, P.; Voegel, J. C.; Picart, C. *Langmuir* **2004,** 20, (2), 448-458.

42. Haynie, D. T.; Balkundi, S.; Palath, N.; Chakravarthula, K.; Dave, K. *Langmuir* **2004,** 20, (11), 4540-4547.

43. Lvov, Y. M.; Lu, Z. Q.; Schenkman, J. B.; Zu, X. L.; Rusling, J. F. *Journal of the American Chemical Society* **1998,** 120, (17), 4073-4080.

44. Toellner, L.; Fischlechner, M.; Ferko, B.; Grabherr, R. M.; Donath, E. *Clinical Chemistry* **2006,** 52, (8), 1575-1583.

45. Ladam, G.; Schaaf, P.; Decher, G.; Voegel, J. C.; Cuisinier, F. J. G. *Biomolecular Engineering* **2002,** 19, (2-6), 273-280.

46. Dimitrova, M.; Arntz, Y.; Lavalle, P.; Meyer, F.; Wolf, M.; Schuster, C.; Haikel, Y.; Voegel, J. C.; Ogier, J. *Advanced Functional Materials* **2007,** 17, (2), 233-245.

47. Shimazaki, Y.; Nakamura, R.; Ito, S.; Yamamoto, M. *Langmuir* **2001,** 17, (3), 953-956.

48. Sui, Z. J.; Salloum, D.; Schlenoff, J. B. *Langmuir* **2003,** 19, (6), 2491-2495.

49. Ferreira, M.; Rubner, M. F. *Macromolecules* **1995,** 28, (21), 7107-7114.

50. Priolo, M. A.; Holder, K. M.; Gamboa, D.; Grunlan, J. C. *Langmuir* **2011,** 27, (19), 12106-12114.

51. Mermut, O.; Barrett, C. J. *Journal of Physical Chemistry B* **2003,** 107, (11), 2525-2530.

52. Shiratori, S. S.; Rubner, M. F. *Macromolecules* **2000,** 33, (11), 4213-4219.

53. McAloney, R. A.; Sinyor, M.; Dudnik, V.; Goh, M. C. *Langmuir* **2001,** 17, (21), 6655-6663.

54. Buscher, K.; Graf, K.; Ahrens, H.; Helm, C. A. *Langmuir* **2002,** 18, (9), 3585-3591.

55. Tan, H. L.; McMurdo, M. J.; Pan, G. Q.; Van Patten, P. G. *Langmuir* **2003,** 19, (22), 9311-9314.

56. Podsiadlo, P.; Michel, M.; Lee, J.; Verploegen, E.; Kam, N. W. S.; Ball, V.; Lee, J.; Qi, Y.; Hart, A. J.; Hammond, P. T.; Kotov, N. A. *Nano Letters* **2008,** 8, (6), 1762-1770.

57. Zhai, L.; Cebeci, F. C.; Cohen, R. E.; Rubner, M. F. *Nano Letters* **2004,** 4, (7), 1349-1353.

58. Zhang, L.; Sun, J. Q. *Macromolecules* **2010,** 43, (5), 2413-2420.

59. Ogawa, T.; Ding, B.; Sone, Y.; Shiratori, S. *Nanotechnology* **2007,** 18, (16), -.

60. Podsiadlo, P.; Paternel, S.; Rouillard, J. M.; Zhang, Z. F.; Lee, J.; Lee, J. W.; Gulari, L.; Kotov, N. A. *Langmuir* **2005,** 21, (25), 11915-11921.

61. Dvoracek, C. M.; Sukhonosova, G.; Benedik, M. J.; Grunlan, J. C. *Langmuir* **2009,** 25, (17), 10322-10328.

62. Etienne, O.; Gasnier, C.; Taddei, C.; Voegel, J. C.; Aunis, D.; Schaaf, P.; Metz-Boutigue, M. H.; Bolcato-Bellemin, A. L.; Egles, C. *Biomaterials* **2005,** 26, (33), 6704-6712.

63. Kim, B. S.; Park, S. W.; Hammond, P. T. *Acs Nano* **2008,** 2, (2), 386-392.

64. Chung, A. J.; Rubner, M. F. *Langmuir* **2002,** 18, (4), 1176-1183.

65. Quinn, J. F.; Caruso, F. *Macromolecules* **2005,** 38, (8), 3414-3419.

66. Daiko, Y.; Katagiri, K.; Matsuda, A. *Chem Mater* **2008,** 20, (20), 6405-6409.

67. Park, Y. T.; Ham, A. Y.; Grunlan, J. C. *Journal of Physical Chemistry C* **2010,** 114, (14), 6325-6333.

68. Park, J.; Fouche, L. D.; Hammond, P. T. *Advanced Materials* **2005,** 17, (21), 2575-2579.

69. Cho, C. Y.; Valverde, L.; Ozin, G. A.; Zacharia, N. S. *Langmuir* **2010,** 26, (16), 13637-13643.

70. Tokuhisa, H.; Hammond, P. T. *Advanced Functional Materials* **2003,** 13, (11), 831-839.

71. Du, N.; Zhang, H.; Chen, J.; Sun, J. Y.; Chen, B. D.; Yang, D. R. *Journal of Physical Chemistry B* **2008,** 112, (47), 14836-14842.

72. Choudalakis, G.; Gotsis, A. D. *Eur Polym J* **2009,** 45, (4), 967-984.

73. Dury-Brun, C.; Chalier, P.; Desobry, S.; Voilley, A. *Food Rev Int* **2007,** 23, (3), 199-255.

74. Knudsen, M. *The Kinetic Theory of Gases: Some Modern Aspects*. Methuen & Co. Ltd.: London, 1934.

75. Yamasaki, A.; Inoue, H. *J Membrane Sci* **1991,** 59, (3), 233-248.

76. Li, D.; Hwang, S. T. *J Membrane Sci* **1991,** 59, (3), 331-352.

77. Kim, S.; Ehrman, S. H. *Langmuir* **2007,** 23, (5), 2497-2504.

78. Barrer, R. M. *J Phys Chem-Us* **1957,** 61, (2), 178-189.

79. Brandt, W. W. *J Phys Chem-Us* **1959,** 63, (7), 1080-1084.

80. Pace, R. J.; Datyner, A. *J Polym Sci Pol Phys* **1979,** 17, (10), 1675-1692.

81. Dibenedetto, A. T. *J Polym Sci Part A* **1963,** 1, (11), 3477.

82. Fujita, H.; Kishimoto, A.; Matsumoto, K. *T Faraday Soc* **1960,** 56, (3), 424-437.

83. Barrer, R. M.; Barrie, J. A.; Slater, J. *J Polym Sci* **1958,** 27, (115), 177-197.

84. Koros, W. J.; Paul, D. R.; Rocha, A. A. *J Polym Sci Pol Phys* **1976,** 14, (4), 687-702.

85. Nielsen, L. E. *J. Macromol. Sci. (Chem).* **1967,** A1, (5), 929-942.

86. Cussler, E. L.; Hughes, S. E.; Ward, W. J.; Aris, R. *J Membrane Sci* **1988,** 38, (2), 161-174.

87. Koros, W. J. *Barrier Polymers and Structures*. American Chemical Society: Washington, DC, 1990.

88. Klopffer, M. H.; Flaconneche, B. *Oil Gas Sci Technol* **2001,** 56, (3), 223-244.

89. Barrer, R. M. *Nature* **1937,** 140, 106-107.

90. Frisch, H. L. *Polym Eng Sci* **1980,** 20, (1), 2-13.

91. Stern, S. A. *J Membrane Sci* **1994,** 94, 1-65.

92. Chen, B.; Evans, J. R. G.; Greenwell, H. C.; Boulet, P.; Coveney, P. V.; Bowden, A. A.; Whiting, A. *Chem Soc Rev* **2008,** 37, (3), 568-594.

93. Sen, S.; Thomin, J. D.; Kumar, S. K.; Keblinski, P. *Macromolecules* **2007,** 40, (11), 4059-4067.

94. Lee, K. Y.; Kim, K. H.; Jeoung, S. K.; Ju, S. I.; Shim, J. H.; Kim, N. H.; Lee, S. G.; Lee, S. M.; Lee, J. K.; Paul, D. R. *Polymer* **2007,** 48, (14), 4174-4183.

95. Fornes, T. D.; Yoon, P. J.; Keskkula, H.; Paul, D. R. *Polymer* **2001,** 42, (25), 9929-9940.

96. Yoon, P. J.; Fornes, T. D.; Paul, D. R. *Polymer* **2002,** 43, (25), 6727-6741.

97. Zhu, J.; Uhl, F. M.; Morgan, A. B.; Wilkie, C. A. *Chem Mater* **2001,** 13, (12), 4649-4654.

98. Gojny, F. H.; Wichmann, M. H. G.; Fiedler, B.; Kinloch, I. A.; Bauhofer, W.; Windle, A. H.; Schulte, K. *Polymer* **2006,** 47, (6), 2036-2045.

99. Du, B. X.; Guo, Z. H.; Fang, Z. P. *Polym Degrad Stabil* **2009,** 94, (11), 1979-1985.

100. Li, Y. C.; Schulz, J.; Mannen, S.; Delhom, C.; Condon, B.; Chang, S.; Zammarano, M.; Grunlan, J. C. *Acs Nano* **2010,** 4, (6), 3325-3337.

101. Li, Y. C.; Mannen, S.; Schulz, J.; Grunlan, J. C. *Journal of Materials Chemistry* **2011,** 21, (9), 3060-3069.

102. Picard, E.; Vermogen, A.; Gerard, J. F.; Espuche, E. *J Membrane Sci* **2007,** 292, (1-2), 133-144.

103. Fredrickson, G. H.; Bicerano, J. *J Chem Phys* **1999,** 110, (4), 2181-2188.

104. Nazarenko, S.; Meneghetti, P.; Julmon, P.; Olson, B. G.; Qutubuddin, S. *J Polym Sci Pol Phys* **2007,** 45, (13), 1733-1753.

105. Nguyen, S. T.; Stankovich, S.; Dikin, D. A.; Dommett, G. H. B.; Kohlhaas, K. M.; Zimney, E. J.; Stach, E. A.; Piner, R. D.; Ruoff, R. S. *Nature* **2006,** 442, (7100), 282-286.

106. Sun, L. Y.; Boo, W. J.; Clearfield, A.; Sue, H. J.; Pham, H. Q. *J Membrane Sci* **2008,** 318, (1-2), 129-136.

107. Priolo, M. A.; Gamboa, D.; Holder, K. M.; Grunlan, J. C. *Nano Letters* **2010,** 10, (12), 4970-4974.

108. Pinnavaia, T. J. *Science* **1983,** 220, (4595), 365-371.

109. Usuki, A.; Kojima, Y.; Kawasumi, M.; Okada, A.; Fukushima, Y.; Kurauchi, T.; Kamigaito, O. *J Mater Res* **1993,** 8, (5), 1179-1184.

110. Ploehn, H. J.; Liu, C. Y. *Industrial & Engineering Chemistry Research* **2006,** 45, (21), 7025-7034.

111. Giannelis, E. P.; Krishnamoorti, R.; Manias, E. *Adv Polym Sci* **1999,** 138, 107-147.

112. Usuki, A.; Koiwai, A.; Kojima, Y.; Kawasumi, M.; Okada, A.; Kurauchi, T.; Kamigaito, O. *Journal of Applied Polymer Science* **1995,** 55, (1), 119-123.

113. Chen, B. *British Ceramic Transactions* **2004,** 103, (6), 241-249.

114. Dubois, P.; Alexandre, M. *Materials Science & Engineering R-Reports* **2000,** 28, (1-2), 1-63.

115. Pinnavaia, T. J.; Beall, G. W. *Polymer-Clay Nanocomposites*. John Wiley: New York, NY, 2000.

116. Lan, T.; Kaviratna, P. D.; Pinnavaia, T. J. *Chem Mater* **1995,** 7, (11), 2144-2150.

117. Osman, M. A.; Rupp, J. E. P.; Suter, U. W. *Polymer* **2005,** 46, (19), 8202-8209.

118. Biswas, M.; Ray, S. S. *New Polymerization Techniques and Synthetic Methodologies* **2001,** 155, 167-221.

119. Takahashi, S.; Goldberg, H. A.; Feeney, C. A.; Karim, D. P.; Farrell, M.; O'Leary, K.; Paul, D. R. *Polymer* **2006,** 47, (9), 3083-3093.

120. Lape, N. K.; Nuxoll, E. E.; Cussler, E. L. *J Membrane Sci* **2004,** 236, (1), 29-37.

121. Lange, J.; Wyser, Y. *Packag Technol Sci* **2003,** 16, (4), 149-158.

122. Yan, M.; Kim, T. W.; Erlat, A. G.; Pellow, M.; Foust, D. F.; Liu, H.; Schaepkens, M.; Heller, C. M.; McConnelee, P. A.; Feist, T. P.; Duggal, A. R. *Proceedings of the Ieee* **2005,** 93, (8), 1468-1477.

123. Wagner, J. R. *Multilayer Flexible Packaging*, 1st ed.; Elsevier: Boston, MA, 2010.

124. Leterrier, Y. *Prog Mater Sci* **2003,** 48, (1), 1-55.

125. Lagaron, J. M.; Gimenez, E.; Catala, R.; Gavara, R. *Macromolecular Chemistry and Physics* **2003,** 204, (4), 704-713.

126. Mittal, V. *Barrier Properties of Polymer Clay Nanocomposites*. Nova Science Publishers: New York, NY, 2010.

127. Jamieson, E. H. H.; Windle, A. H. *Journal of Materials Science* **1983,** 18, (1), 64-80.

128. Chatham, H. *Surface & Coatings Technology* **1996,** 78, (1-3), 1-9.

129. Jang, W. S.; Rawson, I.; Grunlan, J. C. *Thin Solid Films* **2008,** 516, (15), 4819-4825.

130. Gohil, R. M. *J Appl Polym Sci* **2011,** 120, (4), 2324-2336.

131. Porter, R. S.; Wang, L. H. *Polymer* **1992,** 33, (10), 2019-2030.

132. Faisant, J. B.; Ait-Kadi, A.; Bousmina, M.; Deschenes, L. *Polymer* **1998,** 39, (3), 533-545.

133. Yeh, J. T.; Huang, S. S.; Yao, W. H.; Wang, I. J.; Chen, C. C. *J Appl Polym Sci* **2004,** 92, (4), 2528-2537.

134. De Petris, S.; Laurienzo, P.; Malinconico, M.; Pracella, M.; Zendron, M. *J Appl Polym Sci* **1998,** 68, (4), 637-648.

135. Da Silva, L.; Bretas, R. E. S. *Polym Eng Sci* **2000,** 40, (6), 1414-1428.

136. Jickells, S. M.; Poulin, J.; Mountfort, K. A.; Fernandez-Ocana, M. *Food Addit Contam* **2005,** 22, (8), 768-782.

137. Finson, E.; Felts, J. *Tappi J* **1995,** 78, (1), 161-165.

138. Barker, C. P.; Kochem, K. H.; Revell, K. M.; Kelly, R. S. A.; Badyal, J. P. S. *Thin Solid Films* **1995,** 257, (1), 77-82.

139. Crawford, G. P. *Flexible Flat Panel Displays*. John Wiley & Sons: Hoboken, NJ, 2005.

140. Choy, K. L. *Prog Mater Sci* **2003,** 48, (2), 57-170.

141. Walther, M.; Heming, M.; Spallek, M. *Surf Coat Tech* **1996,** 80, (1-2), 200-202.

142. Lewis, J. S.; Weaver, M. S. *Ieee Journal of Selected Topics in Quantum Electronics* **2004,** 10, (1), 45-57.

143. Reichelt, K.; X, J. *Thin Solid Films* **1990,** 191, (1), 91-126.

144. Leterrier, Y.; Boogh, L.; Andersons, J.; Manson, J. A. E. *J Polym Sci Pol Phys* **1997,** 35, (9), 1449-1461.

145. Adamantiadi, A.; Badeka, A.; Kontominas, M. G. *Food Addit Contam* **2001,** 18, (11), 1046-1054.

146. Roberts, A. P.; Henry, B. M.; Sutton, A. P.; Grovenor, C. R. M.; Briggs, G. A. D.; Miyamoto, T.; Kano, A.; Tsukahara, Y.; Yanaka, M. *J Membrane Sci* **2002,** 208, (1-2), 75-88.

147. Sproul, W. D.; Graham, M. E.; Wong, M. S.; Lopez, S.; Li, D.; Scholl, R. A. *J Vac Sci Technol A* **1995,** 13, (3), 1188-1191.

148. Iwamori, S.; Gotoh, Y.; Moorthi, K. *Surf Coat Tech* **2003,** 166, (1), 24-30.

149. Spontak, R. J.; Erlat, A. G.; Clarke, R. P.; Robinson, T. C.; Haaland, P. D.; Tropsha, Y.; Harvey, N. G.; Vogler, E. A. *Journal of Physical Chemistry B* **1999,** 103, (29), 6047-6055.

150. Inagaki, N.; Tasaka, S.; Hiramatsu, H. *Journal of Applied Polymer Science* **1999,** 71, (12), 2091-2100.

151. Wuu, D. S.; Chen, T. N.; Wu, C. C.; Chiang, C. C.; Chen, Y. P.; Horng, R. H.; Juang, F. S. *Chem Vapor Depos* **2006,** 12, (4), 220-224.

152. Jiang, J.; Benter, M.; Taboryski, R.; Bechgaard, K. *Journal of Applied Polymer Science* **2010,** 115, (5), 2767-2772.

153. Sobrinho, A. S. D.; Czeremuszkin, G.; Latreche, M.; Dennler, G.; Wertheimer, M. R. *Surf Coat Tech* **1999,** 116, 1204-1210.

154. Gruniger, A.; von Rohr, P. R. *Thin Solid Films* **2004,** 459, (1-2), 308-312.

155. Xu, B.; Zheng, Q.; Song, Y. H.; Shangguan, Y. *Polymer* **2006,** 47, (8), 2904-2910.

156. Yano, K.; Usuki, A.; Okada, A. *J Polym Sci Pol Chem* **1997,** 35, (11), 2289-2294.

157. Osman, M. A.; Mittal, V.; Morbidelli, M.; Suter, U. W. *Macromolecules* **2003,** 36, (26), 9851-9858.

158. Kim, J. K.; Hu, C. G.; Woo, R. S. C.; Sham, M. L. *Compos Sci Technol* **2005,** 65, (5), 805-813.

159. Osman, M. A.; Mittal, V.; Suter, U. W. *Macromol Chem Physic* **2007,** 208, (1), 68-75.

160. Ray, S. S.; Yamada, K.; Okamoto, M.; Ueda, K. *Nano Lett* **2002,** 2, (10), 1093-1096.

161. Garcia, A.; Eceolaza, S.; Iriarte, M.; Uriarte, C.; Etxeberria, A. *J Membrane Sci* **2007,** 301, (1-2), 190-199.

162. Iler, R. K. *J Colloid Interf Sci* **1966,** 21, (6), 569-594.

163. Decher, G.; Hong, J. D. *Makromolekulare Chemie-Macromolecular Symposia* **1991,** 46, 321-327.

164. Decher, G.; Hong, J. D.; Schmitt, J. *Thin Solid Films* **1992,** 210, (1-2), 831-835.

165. de Villiers, M. M.; Otto, D. P.; Strydom, S. J.; Lvov, Y. M. *Adv Drug Deliver Rev* **2011,** 63, (9), 701-715.

166. Sukhishvili, S. A.; Granick, S. *J Am Chem Soc* **2000,** 122, (39), 9550-9551.

167. Dai, J. H.; Sullivan, D. M.; Bruening, M. L. *Industrial & Engineering Chemistry Research* **2000,** 39, (10), 3528-3535.

168. Moya, S.; Dahne, L.; Voigt, A.; Leporatti, S.; Donath, E.; Mohwald, H. *Colloids and Surfaces a-Physicochemical and Engineering Aspects* **2001,** 183, 27-40.

169. Hammond, P. T. *Aiche J* **2011,** 57, (11), 2928-2940.

170. Schlenoff, J. B.; Ly, H.; Li, M. *Journal of the American Chemical Society* **1998,** 120, (30), 7626-7634.

171. Decher, G. *Science* **1997,** 277, (5330), 1232-1237.

172. Choi, J.; Rubner, M. F. *Macromolecules* **2005,** 38, (1), 116-124.

173. Gui, Z. L.; Qian, J. W.; Du, B. Y.; Yin, M. J.; An, Q. F. *J Colloid Interf Sci* **2009,** 340, (1), 35-41.

174. Yu, X.; Pishko, M. V. *Biomacromolecules* **2011,** 12, (9), 3205-3212.

175. Lvov, Y.; Decher, G.; Sukhorukov, G. *Macromolecules* **1993,** 26, (20), 5396-5399.

176. Laufer, G.; Carosio, F.; Martinez, R.; Camino, G.; Grunlan, J. C. *Journal of Colloid and Interface Science* **2011,** 356, (1), 69-77.

177. Qi, Z. M.; Honma, I.; Ichihara, M.; Zhou, H. S. *Advanced Functional Materials* **2006,** 16, (3), 377-386.

178. Grunlan, J. C.; Choi, J. K.; Lin, A. *Biomacromolecules* **2005,** 6, (2), 1149-1153.

179. McKenzie, K. J.; Marken, F.; Hyde, M.; Compton, R. G. *New J Chem* **2002,** 26, (5), 625-629.

180. Kotov, N. A.; Haraszti, T.; Turi, L.; Zavala, G.; Geer, R. E.; Dekany, I.; Fendler, J. H. *Journal of the American Chemical Society* **1997,** 119, (29), 6821-6832.

181. Jang, W. S.; Grunlan, J. C. *Review of Scientific Instruments* **2005,** 76, (10), 104901.

182. Podsiadlo, P.; Kaushik, A. K.; Arruda, E. M.; Waas, A. M.; Shim, B. S.; Xu, J. D.; Nandivada, H.; Pumplin, B. G.; Lahann, J.; Ramamoorthy, A.; Kotov, N. A. *Science* **2007,** 318, (5847), 80-83.

183. Carosio, F.; Laufer, G.; Alongi, J.; Camino, G.; Grunlan, J. C. *Polymer Degradation and Stability* **2011,** 96, (5), 745-750.

184. Lee, D.; Rubner, M. F.; Cohen, R. E. *Nano Lett* **2006,** 6, (10), 2305-2312.

185. Bravo, J.; Zhai, L.; Wu, Z. Z.; Cohen, R. E.; Rubner, M. F. *Langmuir* **2007,** 23, (13), 7293-7298.

186. Polymer Nanocomposites Laboratory. http://nanocomposites.tamu.edu (accessed Jun 1, 2012).

187. McEuen, P. L.; Bunch, J. S.; Verbridge, S. S.; Alden, J. S.; van der Zande, A. M.; Parpia, J. M.; Craighead, H. G. *Nano Letters* **2008,** 8, (8), 2458-2462.

188. Yang, Y. H.; Malek, F. A.; Grunlan, J. C. *Industrial & Engineering Chemistry Research* **2010,** 49, (18), 8501-8509.

189. Elbert, D. L.; Herbert, C. B.; Hubbell, J. A. *Langmuir* **1999,** 15, (16), 5355-5362.

190. Laugel, N.; Betscha, C.; Winterhalter, M.; Voegel, J. C.; Schaaf, P.; Ball, V. *Journal of Physical Chemistry B* **2006,** 110, (39), 19443-19449.

191. Porcel, C.; Lavalle, P.; Decher, G.; Senger, B.; Voegel, J. C.; Schaaf, P. *Langmuir* **2007,** 23, (4), 1898-1904.

192. Al-Hariri, L. A.; Reisch, A.; Schlenoff, J. B. *Langmuir* **2011,** 27, (7), 3914-3919.

193. Zacharia, N. S.; DeLongchamp, D. M.; Modestino, M.; Hammond, P. T. *Macromolecules* **2007,** 40, (5), 1598-1603.

194. Yoo, P. J.; Nam, K. T.; Qi, J. F.; Lee, S. K.; Park, J.; Belcher, A. M.; Hammond, P. T. *Nature Materials* **2006,** 5, (3), 234-240.

195. Picart, C.; Lavalle, P.; Hubert, P.; Cuisinier, F. J. G.; Decher, G.; Schaaf, P.; Voegel, J. C. *Langmuir* **2001,** 17, (23), 7414-7424.

196. Mendelsohn, J. D.; Barrett, C. J.; Chan, V. V.; Pal, A. J.; Mayes, A. M.; Rubner, M. F. *Langmuir* **2000,** 16, (11), 5017-5023.

197. Liston, E. M.; Martinu, L.; Wertheimer, M. R. *Journal of Adhesion Science and Technology* **1993,** 7, (10), 1091-1127.

198. Gamboa, D.; Priolo, M. A.; Ham, A.; Grunlan, J. C. *Review of Scientific Instruments* **2010,** 81, (3), 036103.

199. ASTM D3985-05 Standard Test Method for Oxygen Gas Transmission Rate Through Plastic Film and Sheeting Using a Coulometric Sensor. ASTM International: West Conshohocken, PA, 2005.

200. Nolte, A. J.; Treat, N. D.; Cohen, R. E.; Rubner, M. F. *Macromolecules* **2008,** 41, (15), 5793-5798.

201. Wong, J. E.; Rehfeldt, F.; Hanni, P.; Tanaka, M.; Klitzing, R. V. *Macromolecules* **2004,** 37, (19), 7285-7289.

202. Philipp, B.; Dautzenberg, H.; Linow, K. J.; Kotz, J.; Dawydoff, W. *Progress in Polymer Science* **1989,** 14, (1), 91-172.

203. Aoki, T.; Kawashima, M.; Katono, H.; Sanui, K.; Ogata, N.; Okano, T.; Sakurai, Y. *Macromolecules* **1994,** 27, (4), 947-952.

204. Fox, T. G. *Bull. Am. Phys. Soc.* **1956,** 1, (2), 123.

205. Wood, L. A. *Journal of Polymer Science* **1958,** 28, (117), 319-330.

206. Jiang, M.; Li, M.; Xiang, M. L.; Zhou, H. *Polymer Synthesis Polymer-Polymer Complexation* **1999,** 146, 121-196.

207. Levasalmi, J. M.; McCarthy, T. J. *Macromolecules* **1997,** 30, (6), 1752-1757.

208. Liou, C. C.; Wu, H. F.; Brodbelt, J. S. *Journal of the American Society for Mass Spectrometry* **1994,** 5, (4), 260-273.

209. Harris, J. J.; Bruening, M. L. *Langmuir* **2000,** 16, (4), 2006-2013.

210. Losche, M.; Schmitt, J.; Decher, G.; Bouwman, W. G.; Kjaer, K. *Macromolecules* **1998,** 31, (25), 8893-8906.

211. Chen, J. Y.; Huang, L.; Ying, L. M.; Luo, G. B.; Zhao, X. S.; Cao, W. X. *Langmuir* **1999,** 15, (21), 7208-7212.

212. Dai, J. H.; Jensen, A. W.; Mohanty, D. K.; Erndt, J.; Bruening, M. L. *Langmuir* **2001,** 17, (3), 931-937.

213. Yang, S. Y.; Rubner, M. F. *Journal of the American Chemical Society* **2002,** 124, (10), 2100-2101.

214. Chen, J. H.; Asano, M.; Yamaki, T.; Yoshida, M. *Journal of Applied Polymer Science* **2006,** 100, (6), 4565-4574.

215. Balachandra, A. M.; Dai, J. H.; Bruening, M. L. *Macromolecules* **2002,** 35, (8), 3171-3178.

216. Ku, B. C.; Froio, D.; Steeves, D.; Kim, D. W.; Ahn, H.; Ratto, J. A.; Blumstein, A.; Kumar, J.; Samuelson, L. A. *Journal of Macromolecular Science-Pure and Applied Chemistry* **2004,** A41, (12), 1401-1410.

217. Tuong, S. D.; Lee, H.; Kim, H. *Macromolecular Research* **2008,** 16, (4), 373-378.

218. Tong, W. J.; Gao, C. Y.; Mohwald, H. *Chem Mater* **2005,** 17, (18), 4610-4616.

219. Richert, L.; Boulmedais, F.; Lavalle, P.; Mutterer, J.; Ferreux, E.; Decher, G.; Schaaf, P.; Voegel, J. C.; Picart, C. *Biomacromolecules* **2004,** 5, (2), 284-294.

220. Schuetz, P.; Caruso, F. *Advanced Functional Materials* **2003,** 13, (12), 929-937.

221. Mauser, T.; Dejugnat, C.; Sukhorukov, G. B. *Macromolecular Rapid Communications* **2004,** 25, (20), 1781-1785.

222. Ducker, R. E.; Montague, M. T.; Leggett, G. J. *Biointerphases* **2008,** 3, (3), 59-65.

223. Park, M. K.; Deng, S. X.; Advincula, R. C. *Journal of the American Chemical Society* **2004,** 126, (42), 13723-13731.

224. Lehaf, A. M.; Moussallem, M. D.; Schlenoff, J. B. *Langmuir* **2011,** 27, (8), 4756-4763.

225. Harris, J. J.; DeRose, P. M.; Bruening, M. L. *Journal of the American Chemical Society* **1999,** 121, (9), 1978-1979.

226. ASTM F1249-06 Standard Test Method for Water Vapor Transmission Rate Through Plastic Film and Sheeting Using a Modulated Infrared Sensor. ASTM International: West Conshohocken, PA, 2006.

227. Garza, J. M.; Schaaf, P.; Muller, S.; Ball, V.; Stoltz, J. F.; Voegel, J. C.; Lavalle, P. *Langmuir* **2004,** 20, (17), 7298-7302.

228. Bieker, P.; Schonhoff, M. *Macromolecules* **2010,** 43, (11), 5052-5059.

229. Sun, B.; Jewell, C. M.; Fredin, N. J.; Lynn, D. M. *Langmuir* **2007,** 23, (16), 8452-8459.

230. Shen, L. Y.; Fu, J. H.; Fu, K.; Picart, C.; Ji, J. A. *Langmuir* **2010,** 26, (22), 16634-16637.

231. Fu, J. H.; Ji, J.; Shen, L. Y.; Kueller, A.; Rosenhahn, A.; Shen, J. C.; Grunze, M. *Langmuir* **2009,** 25, (2), 672-675.

232. Bellamy, L. J. *The Infra-red Spectra of Complex Molecules.* 3rd ed.; Chapman and Hall: New York, NY, 1975.

233. Morcellet, M.; Ghoul, M.; Bacquet, M. *Water Research* **2003,** 37, (4), 729-734.

234. Gao, C. Y.; Tong, W. J.; Mohwald, H. *Macromolecules* **2006,** 39, (1), 335-340.

235. Farris, S.; Song, J. H.; Huang, Q. R. *Journal of Agricultural and Food Chemistry* **2010,** 58, (2), 998-1003.

236. Pinnau, I.; Toy, L. G. *J Membrane Sci* **1996,** 116, (2), 199-209.

237. Novoselov, K. S.; Geim, A. K.; Morozov, S. V.; Jiang, D.; Zhang, Y.; Dubonos, S. V.; IV, G.; Firsov, A. A. *Science* **2004,** 306, (5696), 666-669.

238. Geim, A. K.; Novoselov, K. S.; Morozov, S. V.; Jiang, D.; Katsnelson, M. I.; Grigorieva, I. V.; Dubonos, S. V.; Firsov, A. A. *Nature* **2005,** 438, (7065), 197-200.

239. Balandin, A. A.; Ghosh, S.; Bao, W. Z.; Calizo, I.; Teweldebrhan, D.; Miao, F.; Lau, C. N. *Nano Letters* **2008,** 8, (3), 902-907.

240. Hone, J.; Lee, C.; Wei, X. D.; Kysar, J. W. *Science* **2008,** 321, (5887), 385-388.

241. Zhang, Q. H.; Zhao, X.; Chen, D. J.; Lu, P. *Macromolecules* **2010,** 43, (5), 2357-2363.

242. Li, D.; Muller, M. B.; Gilje, S.; Kaner, R. B.; Wallace, G. G. *Nature Nanotechnology* **2008,** 3, (2), 101-105.

243. Wang, G. X.; Shen, X. P.; Wang, B.; Yao, J.; Park, J. *Carbon* **2009,** 47, (5), 1359-1364.

244. McAllister, M. J.; Li, J. L.; Adamson, D. H.; Schniepp, H. C.; Abdala, A. A.; Liu, J.; Herrera-Alonso, M.; Milius, D. L.; Car, R.; Prud'homme, R. K.; Aksay, I. A. *Chem Mater* **2007,** 19, (18), 4396-4404.

245. Dreyer, D. R.; Park, S.; Bielawski, C. W.; Ruoff, R. S. *Chemical Society Reviews* **2010,** 39, (1), 228-240.

246. Nguyen, S. T.; Stankovich, S.; Dikin, D. A.; Piner, R. D.; Kohlhaas, K. A.; Kleinhammes, A.; Jia, Y.; Wu, Y.; Ruoff, R. S. *Carbon* **2007,** 45, (7), 1558-1565.

247. Fan, Z. J.; Wang, K.; Wei, T.; Yan, J.; Song, L. P.; Shao, B. *Carbon* **2010,** 48, (5), 1686-1689.

248. Lerf, A.; He, H. Y.; Forster, M.; Klinowski, J. *Journal of Physical Chemistry B* **1998,** 102, (23), 4477-4482.

249. Klinowski, J.; He, H. Y.; Forster, M.; Lerf, A. *Chemical Physics Letters* **1998,** 287, (1-2), 53-56.

250. Phillips, C. A. *International Journal of Food Science and Technology* **1996,** 31, (6), 463-479.

251. Bhattacharya, S. K.; Tummala, R. R. *Microelectronics Journal* **2001,** 32, (1), 11-19.

252. Robeson, L. M.; Paul, D. R. *Polymer* **2008,** 49, (15), 3187-3204.

253. Erlat, A. G.; Henry, B. M.; Ingram, J. J.; Mountain, D. B.; McGuigan, A.; Howson, R. P.; Grovenor, C. R. M.; Briggs, G. A. D.; Tsukahara, Y. *Thin Solid Films* **2001,** 388, (1-2), 78-86.

254. Sholl, D. S.; Newsome, D. A. *Nano Letters* **2006,** 6, (9), 2150-2153.

255. Kalaitzidou, K.; Fukushima, H.; Drzal, L. T. *Carbon* **2007,** 45, (7), 1446-1452.

256. Barker, C. P.; Kochem, K. H.; Revell, K. M.; Kelly, R. S. A.; Badyal, J. P. S. *Thin Solid Films* **1995,** 259, (1), 46-52.

257. Felts, J. T. *Journal of Plastic Film and Sheeting* **1993,** 9, (2), 139-158.

258. Garcia, M. G.; Marchese, J.; Ochoa, N. A. *Journal of Applied Polymer Science* **2010,** 118, (4), 2417-2424.

259. Zoppi, R. A.; das Neves, S.; Nunes, S. P. *Polymer* **2000,** 41, (14), 5461-5470.

260. Caseri, W. R. *Materials Science and Technology* **2006,** 22, (7), 807-817.

261. Ye, S. Q.; Wang, C. Y.; Liu, X. X.; Tong, Z. *Journal of Controlled Release* **2005,** 106, (3), 319-328.

262. Loh, K. P.; Wang, Y.; Tong, S. W.; Xu, X. F.; Ozyilmaz, B. *Advanced Materials* **2011,** 23, (13), 1514-1518.

263. Mark, J. E. *Polymer Data Handbook*. 2nd ed.; Oxford University Press: New York, NY, 2009.

264. Shin, H. J.; Kim, K. K.; Benayad, A.; Yoon, S. M.; Park, H. K.; Jung, I. S.; Jin, M. H.; Jeong, H. K.; Kim, J. M.; Choi, J. Y.; Lee, Y. H. *Advanced Functional Materials* **2009,** 19, (12), 1987-1992.

265. Grunlan, J. C.; Grigorian, A.; Hamilton, C. B.; Mehrabi, A. R. *Journal of Applied Polymer Science* **2004,** 93, (3), 1102-1109.

266. Compton, O. C.; Kim, S.; Pierre, C.; Torkelson, J. M.; Nguyen, S. T. *Advanced Materials* **2010,** 22, (42), 4759-4763.

267. Kim, H. M.; Lee, J. K.; Lee, H. S. *Thin Solid Films* **2011,** 519, (22), 7766-7771.

268. Macosko, C. W.; Kim, H.; Abdala, A. A. *Macromolecules* **2010,** 43, (16), 6515-6530.

269. Gao, J.; Liu, F.; Liu, Y. L.; Ma, N.; Wang, Z. Q.; Zhang, X. *Chem Mater* **2010,** 22, (7), 2213-2218.

270. Cummins, H. Z. *Journal of Non-Crystalline Solids* **2007,** 353, (41-43), 3891-3905.

271. Lutkenhaus, J. L.; Olivetti, E. A.; Verploegen, E. A.; Cord, B. M.; Sadoway, D. R.; Hammond, P. T. *Langmuir* **2007,** 23, (16), 8515-8521.

272. Coia, C.; Fozza, A. C.; Wertheimer, M. R.; Czeremuszkin, G.; Houdayer, A. *Protection of Space Materials from the Space Environment* **2001,** 4, 281-290.

273. Erlat, A. G.; Spontak, R. J.; Clarke, R. P.; Robinson, T. C.; Haaland, P. D.; Tropsha, Y.; Harvey, N. G.; Vogler, E. A. *Journal of Physical Chemistry B* **1999,** 103, (29), 6047-6055.

274. Serizawa, T.; Kamimura, S.; Kawanishi, N.; Akashi, M. *Langmuir* **2002,** 18, (22), 8381-8385.

275. Deng, C. C.; Dong, W. F.; Adalsteinsson, T.; Ferri, J. K.; Sukhorukov, G. B.; Mohwald, H. *Soft Matter* **2007,** 3, (10), 1293-1299.

276. Liao, K. H.; Mittal, A.; Bose, S.; Leighton, C.; Mkhoyan, K. A.; Macosko, C. W. *Acs Nano* **2011,** 5, (2), 1253-1258.

APPENDIX A

OVERVIEW OF KEY CHARACTERIZATION TECHNIQUES FOR THIN FILM ASSEMBLIES

A.1 Ellipsometry[1]

Ellipsometry is a non-destructive technique for measuring film thickness and optical properties. When a polarized light hits the sample surface, its polarization state of reflection and transmission also changes, which results in changes in the psi (Ψ) and delta (Δ) parameters:

$$\tan(\Psi) \cdot e^{i\Delta} = \rho = \frac{r_p}{r_s} \tag{A.1}$$

where Ψ is the amplitude ratio, Δ is the phase change, ρ is the complex reflectance ratio, and r_p and r_s are the reflectivity of p-polarized and s-polarized light. A schematic setup for an ellipsometry experiment is shown in Figure A.1.

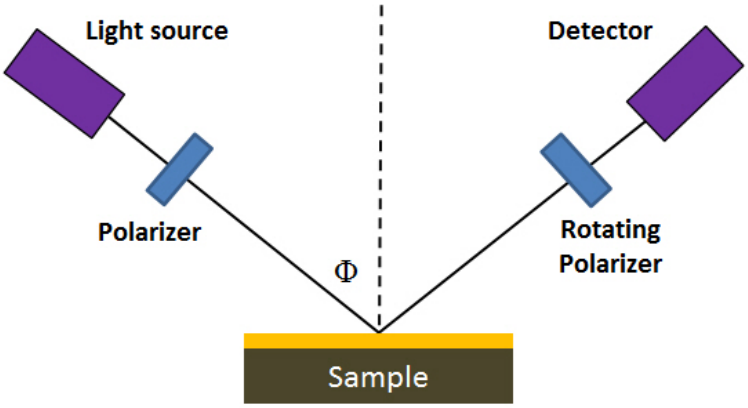

Figure A.1. Schematic of an ellipsometry experiment (adapted from ref. 2).

The light source in Fig. A.1 emits unpolarized light through a polarizer, which only transmits light with a specific electric field orientation. This linearly polarized light then hits the sample surface and reflects elliptically polarized light onto a rotating polarizer and a detector. The detector converts the polarized light into an electronic signal which is then compared with the input polarization to determine the change from sample reflection. The acquired psi/delta (Ψ,Δ) can be transformed into optical constants (n,k), where n represents the refractive index and k represents the extinction coefficient. Figure A.2 shows the reflection and refraction of light from the interface of two media. From the Fresnel equation, r_p and r_s can be described as:

$$r_s = \frac{n_i \cos\Phi_i - n_t \cos\Phi_t}{n_i \cos\Phi_i + n_t \cos\Phi_t} \qquad \text{(A.2)}$$

$$r_p = \frac{n_t \cos\Phi_i - n_i \cos\Phi_t}{n_i \cos\Phi_t + n_t \cos\Phi_i} \qquad \text{(A.3)}$$

where n_i and n_t represent the refractive indices of incidental and transmitted media, respectively.

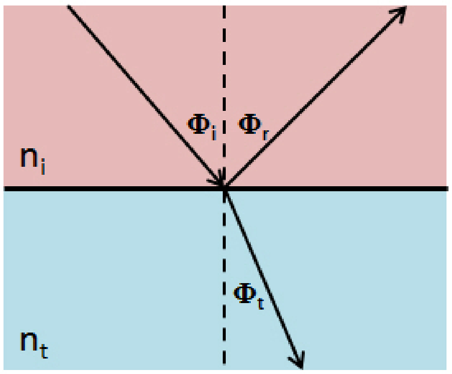

Figure A.2. Reflection and refraction of light at the interface between two media.

Analyzing ellipsometric data involves: (1) constructing an optical model with corresponding samples, (2) selecting or modeling the dielectric functions, and (3) fitting the calculated ellipsometric psi (Ψ) and delta (Δ) parameters data with experimentally acquired (Ψ,Δ) using the mean square error (MSE) method. In the case of thin, transparent layer-by-layer (LbL) coatings on silicon wafers, the refractive index and film thickness can both be calculated with the Cauchy model:

$$n = \sqrt{\varepsilon_1} = A + \frac{B}{\lambda^2} + \frac{C}{\lambda^4} \tag{A.4}$$

where λ is the wavelength of the light and A, B, C are the analytical parameters. Refractive indices from the Cauchy model are calculated by iterations of A, B, C and λ that are inserted into Equations A.2 and A.3 (to be compared with the experimentally measured ρ descried in Equation A.1).

Spectroscopic ellipsometry (SE), in contrast to single wavelength ellipsometry, has a light source with a broad set of wavelengths (380 – 900 nm). SE provides a Ψ and Δ data set at each measurable wavelength, which generates a precisely calculated thickness value. The thicknesses of the LbL films reported within this dissertation were measured with an alpha-SE Ellipsometer (J. A. Woollam Co., Inc., Lincoln, NE). These measurements are calculated based on the assumption that the surface roughness of deposited film is less than 40 nm.[3] Two different models, *Si with transparent film* and *Si with absorbing film,* were used to fit Ψ and Δ. The resulting thickness, with the smallest MSE, was selected as the reported thickness (See Fig. 4.2, 5.2(a), 7.1(a), 7.2 and Tables 4.1 and 5.1).

A.2 Quartz Crystal Microbalance (QCM)[4, 5]

Traditional scales are not sensitive enough to accurately and precisely measure mass changes within the micro- and nanogram range. QCM is a mass loading sensor that can provide a mass measurement precision of 10^{-13} g.[6] The experimental set-up for this device is shown in Figure A.3. Gold, keyhole shaped films are deposited onto a quartz crystal and act as electrodes that capture alterations to the calibrated oscillatory frequency. Using the Sauerbrey equation:[7]

$$\Delta f = -\frac{2 f_0^{\,2}}{A\sqrt{\rho_q \mu_q}} \Delta m \tag{A.7}$$

where Δf is frequency change, f_0 is resonant frequency, A is active crystal area, ρ_q is the density of quartz, μ_q is shear modulus of quartz crystal and Δm is the mass change, changes in this frequency can be converted into a real-time mass deposition (e.g. the frequency is proportional to the mass deposited on the quartz crystal).

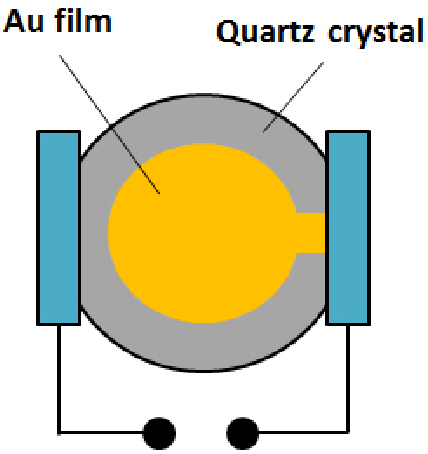

Figure A.3. Schematic of a quartz crystal for mass measurement (adapted from ref. 8).

In this dissertation, the mass increments of LbL deposition were measured with a Research Quartz Crystal Microbalance (Inficon, East Sycrase, NY) with a frequency range of 3.8 - 6 MHz. The 5 MHz quartz crystal was inserted in a polypropylene holder and dipped into the cationic and anionic polyelectrolyte solutions. After each deposition, with deionized water rinsing and filtered air drying, a thin layer was adsorbed onto the quartz crystal. The holder was then left on the microbalance to stabilize for 5 minutes to equilibrate before taking a measurement. Figures 3.2, 4.1(e), 5.2(b), 6.3, 6.6, and Tables 6.1 and 6.2 show these results.

A.3 Fourier Transform Infrared Spectroscopy (FTIR)[9, 10]

FITR provides information about the chemical bonds by comparing the sample absorption bands at each wavelength with absorption bands of known chemical bonds or functional groups. By analyzing the IR spectrum of a radiated sample, one can identify the existed bonding in the structure. The two most common modes used in FTIR measurements are transmission and attenuated total reflection (ATR) mode. An IR transparent substrate (e.g., zinc selenide (ZnSe)) is used in transmission mode, while in ATR mode the thin films can be deposited on opaque substrates (e.g., silicon wafers).[11-13] In transmission mode, a film deposited onto ZnSe absorbs the infrared radiation from the light source. Detectors then receive the transmitted light and transform it into absorption bands at different wavenumbers. Figure A.4 shows a schematic of transmission and ATR modes, respectively.

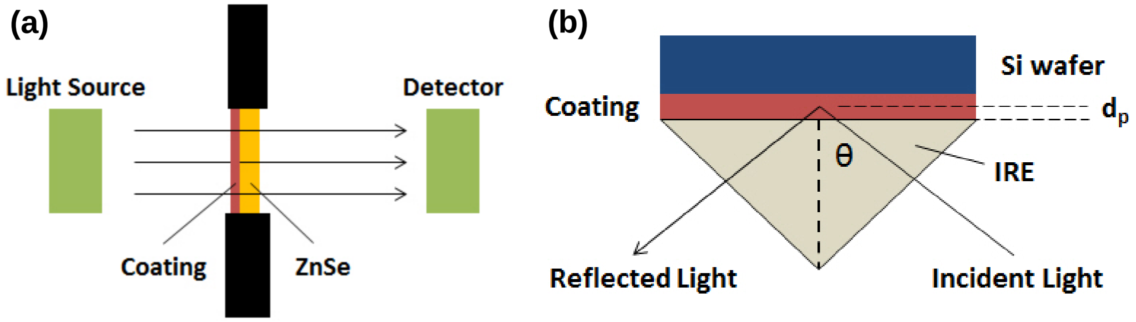

Figure A.4. Schematics of FTIR in transmission (a) and ATR (b) modes (adapted from ref. 9).

ATR mode is more effective for getting IR spectra of thin films. The tested sample is in close contact with an internal reflection element (IRE) (Fig. A.4(b)). When the angle of incidence exceeds the critical angle for internal reflection, an evanescent wave will be generated at the reflecting surface and absorbed by the sample. The penetration depth, d_p, can be described as:[9]

$$d_p = \frac{\lambda}{2\pi n_{IRE}\sqrt{\sin^2\theta - \left(n_c / n_{IRE}\right)^2}} \tag{A.8}$$

where λ is the wavelength of IR radiation, n_{IRE} is the refractive index of IRE, θ is the angle of incidence and n_c is the refractive index of the coating. From Equation A.8, the depth of penetration varies with wavelength, suggesting ATR intensities decrease at high wavenumbers (λ^{-1}). Refractive index of the IRE also influences the depth of penetration. An ALPHA-P10098-4 spectrometer (Bruker Optics Inc., Billerica, MA) was used in this dissertation for FTIR measurement using ATR mode with a diamond IRE ($n_{IRE} = 2.4$), which has a depth of penetration around 2 μm at a 45° incident angle (at wavenumber

1000 cm^{-1}), assuming $n_c = 1.5$ (calculated from Equation A.8). All thin films analyzed using ATR FTIR in this dissertation were less than 1.5 μm thick, which suggests this technique probed the entire film thickness. Figures 4.4 and 4.5 show these results.

A.4 Oxygen Transmission Rate Measurement

Oxygen transmission rate (OTR) of LbL films coated on 7-mil PET were tested by MOCON using an OX-TRAN 2/21 testing module, which is shown schematically in Figure A.5. A testing sample is inserted as the interface of two different testing chambers, which are fed with carrier (N_2) and test (O_2) gas flows, respectively. A patented coulometric sensor (COULOX®) is connected to each chamber to detect oxygen transmission through the test film. For oxygen permeation tests at various relative humidities (RH), moist N_2 and O_2 can be used. The final OTR is collected after the equilibrium is achieved, which takes at least 100 hours for a good barrier material (OTR < 1 $cc/m^2 \cdot day$). An example of OTR as a function of time of 60BL PEI/GO film coated on PET is shown in Figure A.6. After more than 500 hours of testing, this film still had not reached equilibrium. The testing range of OX-TRAN 2/21 is 0.005 to 200 $cc/m^2 \cdot day$.[14]

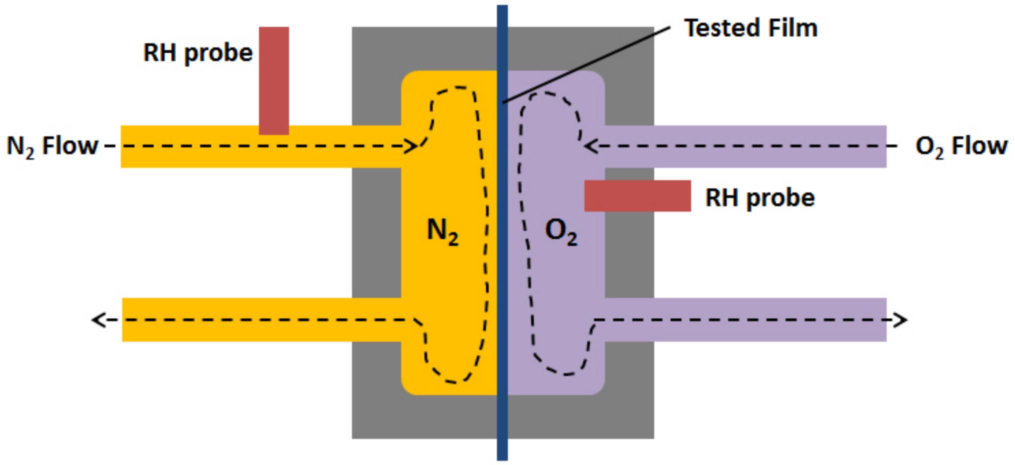

Figure A.5. Schematic of a testing cell of OX-TRAN 2/21oxygen permeation testing.

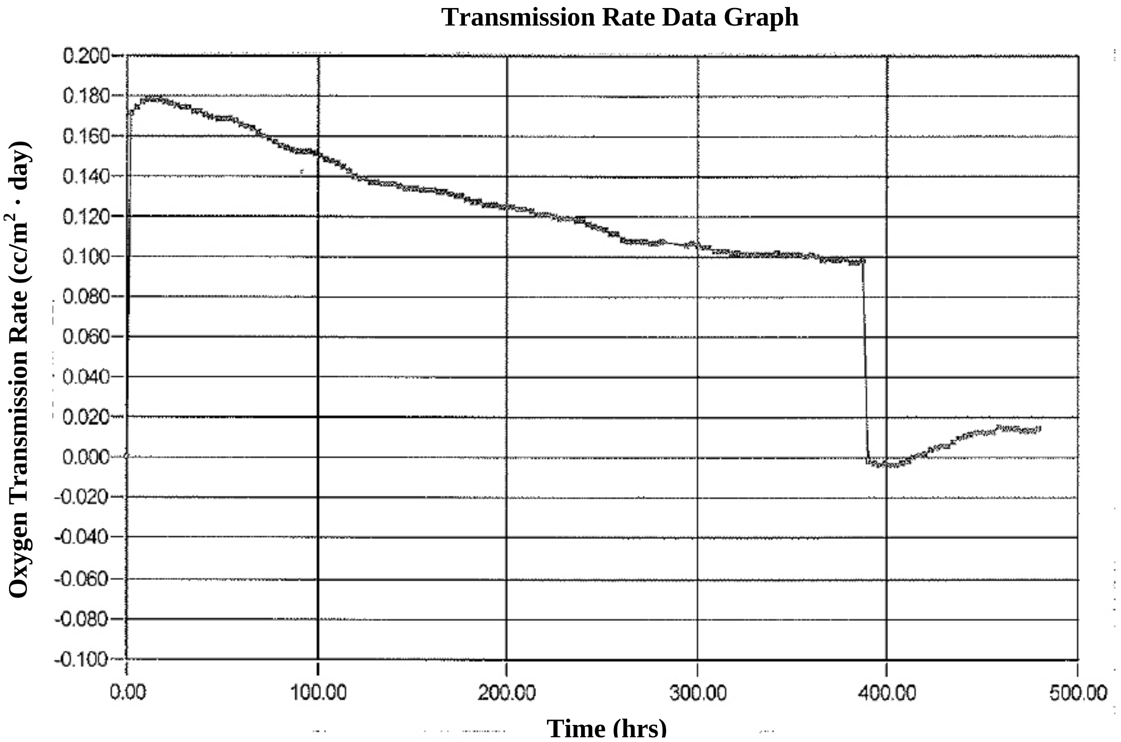

Figure A.6. Oxygen transmission rate as a function of time of a LbL film on PET tested by MOCON.

A.5 References

1. Fujiwara, H. *Spectroscopic Ellipsometry : Principles and Applications*. John Wiley & Sons: Hoboken, NJ, 2007.

2. Wikipedia. http://en.wikipedia.org/wiki/File:Ellipsometry_setup.svg (accessed Jun 8, 2012).

3. J.A. Woollam Co., Inc. www.jawoollam.com (accessed Jun 12, 2012).

4. O'Sullivan, C. K.; Guilbault, G. G. *Biosens Bioelectron* **1999,** 14, (8-9), 663-670.

5. Lu, C.; Czanderna, A. W. *Applications of Piezoelectric Quartz Crystal Microbalances*. Elsevier: New York, 1984.

6. Mecea, V. M. *J Therm Anal Calorim* **2006,** 86, (1), 9-16.

7. Sauerbrey, G. *Z Phys* **1959,** 155, (2), 206-222.

8. Biosensing Instrument. http://www.biosensingusa.com/Application103.html (accessed Jun 8, 2012).

9. Gèunzler, H.; Gremlich, H. U. *IR Spectroscopy : An Introduction*. Wiley-VCH: Weinheim, 2002.

10. Urban, M. W. *Attenuated Total Reflectance Spectroscopy of Polymers: Theory and Practice*. American Chemistry Society: Washington, DC, 1996.

11. Turgeman, R.; Gershevitz, O.; Palchik, O.; Deutsch, M.; Ocko, B. M.; Gedanken, A.; Sukenik, C. N. *Cryst Growth Des* **2004,** 4, (1), 169-175.

12. Choi, K.; Ghosh, S.; Lim, J.; Lee, C. M. *Appl Surf Sci* **2003,** 206, (1-4), 355-364.

13. Muller, M.; Heinen, S.; Oertel, U.; Lunkwitz, K. *Macromol Symp* **2001,** 164, 197-210.

14. MOCON. www.mocon.com (accessed Jun 8, 2012).

VITA

You-Hao Yang was born in Taipei, Taiwan. He received his Bachelor of Science degree in chemical engineering from the National Taiwan University in 2007. After one year of military service, he entered the doctoral program at Texas A&M University, where in August 2012 he received his Ph.D. degree, in chemical engineering. His research interests include gas barrier coatings, polymer characterization and polymer nanocomposites. His permanent address is 3122 TAMU, Department of Chemical Engineering, Texas A&M University, College Station, TX 77843. His e-mail address is yangyouhao@gmail.com.